UNIVERSITÀ DEGLI STUDI DI NAPOLI FEDERICO II

SCUOLA POLITECNICA E DELLE SCIENZE DI BASE
AREA DIDATTICA SCIENZE MATEMATICHE, FISICHE E NATURALI

DIPARTIMENTO DI SCIENZE DELLA TERRA, DELL'AMBIENTE
E DELLE RISORSE

TESI DI DOTTORATO
XXXV CICLO

MORFOLOGIE CEREBRALI E SOCIALITÀ NEI GRANDI MAMMIFERI

Tutor:
Prof. Pasquale Raia
Coordinatore:
Prof.ssa Rosa Di Maio

Candidata:
Maria Modafferi
Matricola:
DR993807

Anno Accademico 2022/2023

Indice dei contenuti

Abstract

La presente tesi si occupa dello studio sui rapporti che intercorrono tra morfologia cerebrale e socialità nei mammiferi di grossa taglia, viventi ed estinti, con una particolare attenzione all'Ordine *Carnivora*. L'obbiettivo è verificare quanto propinato dalla SBH ("*The social brain hypothesis",* Dunbar, 1998). Per l'antropologo inglese, un ruolo sostanziale nell'evoluzione della morfologia cerebrale e nello sviluppo della neocorteccia negli animali (uomo compreso) è fornito dalla socialità e non tanto dalla sola ecologia.

Dunque, l'approccio alla problematica di ricerca presentata si è sostanzialmente articolato in due fasi distinte: raccolta dei dati ed il loro processamento.

Per la raccolta dei dati, ho messo a punto un database con **643 mesh 3D** di crani appartenenti a diversi gruppi tassonomici, sia viventi che estinti, avendo cura di selezionare un maschio ed una femmina qualora possibile. La scelta di campioni di entrambi i sessi è stata fondamentale per motivi legati al dimorfismo sessuale.

Le banche dati a cui ho attinto per il reperimento delle superfici 3D sono state: Digimorph (http://www.digimorph.org), KUPRI (http://dmm.ehub.kyoto-u.ac.jp), Morphosource (https://www.morphosource.org/), Phenome10K (https://www.phenome10k.org/), Sketchfab (https://sketchfab.com/). Tali oggetti, messi a disposizione da enti pubblici e/o privati, sono usufruibili a scopi scientifici in modo gratuito e *open source*.

Per effettuare analisi successive, le mesh 3D dovevano essere tutte necessariamente in formato .ply. Perciò, ho dovuto talvolta estrarre le superfici a partire direttamente dalle CT-scan, utilizzando i seguenti software: **Amira** (version 5.4.5, Visualization Sciences Group, © 20132) e **Mimics research** 21.0.

Amira visualizza, analizza e modella i dati tridimensionali, rappresentati come volumi di immagini o superfici geometriche (di forma triangolare o poliedrica). **Mimics** invece si serve delle **DICOM** (***D****igital* ***I****maging and* ***CO****mmunications in* ***M****edicine*), che permettono la comunicazione,

visualizzazione, archiviazione e stampa di informazioni di tipo biomedico, quali ad esempio immagini radiologiche.

Sono state quindi applicate tecniche di **morfometria geometrica** (GMM) e **metodi filogenetici comparativi** (PCMs) sui dati di input al fine di realizzare studi destinati a riviste impattate.

Si è rivelato necessario il software RStudio, e soprattutto i pacchetti **Arothron** (Profico et al., 2021) ed **RRphylo** (Castiglione et al., 2018).

Del primo, la funzione che più ho utilizzato è stata *endomaker* (Profico et al., 2020) che permette l'estrazione di *endocast,* ovvero calchi delle cavità cerebrali, a partire da superfici 3D (in formato .ply, .obj, .stl) ed il calcolo dei volumi cerebrali (ECV).

La funzione si basa sull'algoritmo **AST-3D** (*automatic segmentation tool for 3D object,* Profico et al., 2018) che, grazie ad una nuova implementazione (Profico et al., 2020) è in grado di riconoscere automaticamente la cavità endocranica, posizionare i **POVs** (*point of views*) in completa autonomia senza intervento dell'utente.

RRphylo (Castiglione et al., 2018) rientra nei metodi filogenetici comparativi (PCMs). Si sviluppa sulla *phylogenetic ridge regression* (Kratsch & Mchardy 2014; Gubry-Rangin et al. 2015) che, lavorando sulle filogenesi, consente di stimare i tassi di variazione fenotipica lungo i rami degli alberi filogenetici sia per specie viventi che per i fossili.

L'evoluzione del tratto è descritta attraverso la seguente equazione:

$$\boldsymbol{\Delta P = \beta_1 l_1 + \beta_2 l_2 + \cdots + \beta_n l_n}$$

β = coefficiente di regressione del *branch* (ramo) dell'albero considerato nel percorso dal *root* (radice) al *tip* (parte finale).

l = lunghezza del *branch.*

La presente tesi è suddivisa in sei capitoli, di cui uno introduttivo.

L'introduzione si occupa di una rapida panoramica su paleontologia virtuale e morfometria geometrica con annessi vantaggi e tecniche di acquisizione.

Dal momento questa tesi è fortemente incentrata sui mammiferi, ed in particolar modo sui carnivori, risultava doveroso fare in seguito un *excursus* sulla loro evoluzione.

La fine della parte introduttiva riprende nuovamente i materiali e metodi utilizzati al fine dell'elaborazione dei dati campionati, per poi discutere sugli scopi di ricerca perseguiti durante il triennio.

I rimanenti capitoli della tesi sono incentrati ciascuno su un articolo pubblicato su riviste impattate, a cui ho lavorato nel corso del mio dottorato.

Il primo articolo, in via di definizione, analizza la variazione fenotipica nel cranio e negli endocast dei mammiferi carnivori.

Il secondo lavoro *("One among many: the enigmatic case of the Miocene mammal, Kolponomos newportensis"*, Modafferi et al., 2022) riguarda lo studio sulla presenza di convergenza evolutiva tra un enigmatico mammifero del Miocene, *Kolponomos newportensis*, e diverse specie di *sabretooth* (in italiano: tigri dai denti a sciabola) quali *Barbourofelis frickii, Homotherium serum, Hoplophoneus primaevus, Smilodon fatalis* e *Smilodon californicus.* Tale studio mira a verificare l'ipotesi secondo cui le tecniche di caccia di queste specie filogeneticamente lontane presentassero in realtà palesi elementi di convergenza.

Il focus del terzo lavoro (*"Human face-off: a new method for mapping evolutionary rates on three-dimensional digital models"*, Castiglione et al., 2022) riguarda lo studio dell'evoluzione dello splancnocranio negli Hominoidea. Per farlo, sono stati condotti studi di morfometria geometrica e filogenetici. In particolare, è stata proposta una nuova implementazione del pacchetto **RRphylo** (Castiglione et al., 2018): *rate.map,* che stima i tassi evolutivi del cambiamento dei fenotipi per ogni ramo dell'albero filogenetico considerato.

Parimenti al terzo lavoro, anche per il quarto (*"A method for mapping morphological convergenze on three-dimensional digital models: the case of the mammalian sabretooth",* Melchionna et al., 2021) la morfometria geometrica e l'utilizzo di un'altra implementazione, *conv.map,* presente nel pacchetto **RRphylo** (Castiglione et al., 2018) ne hanno costituito l'ossatura.

A differenza però di *rate.map,* quest'ultimo rileva la presenza di pattern di convergenza evolutiva tra specie diverse filogeneticamente; pertanto, ci ha permesso capire che la convergenza evolutiva nelle diverse specie di *sabretooth* sia particolarmente evidente nella parte posteriore del cranio.

Tale carattere si è rivelato strategico ai fini dell'uccisione di prede di taglia medio-grande.

Il quinto ed ultimo articolo, (*"A major change in rate of climate niche envelope evolution during hominid history"*, Mondanaro et al., 2020) applicando dati paleoclimatici, filogenetici ed archeologici si è focalizzato su come *Homo sapiens* sia stata l'unica specie ad essere in grado di adattarsi ad ogni ambiente e clima sulla Terra.

Dai risultati ottenuti si è evinto che in realtà questa sua capacità è dovuta non tanto a pura filogenesi, quanto all'innovazione tecnologica.

Introduzione

1. Paleontologia digitale e morfometria geometrica

Allo stato attuale, la paleontologia ha sicuramente subito notevoli sviluppi sull'approccio ai reperti. L'avvento di metodologie sempre più dettagliate e meno invasive, ha permesso lo studio in estremo dettaglio dei fossili.

Ciò riguarda non solo le parti anatomiche, quali ossa, vasi sanguigni ed *endocast* (Profico et al., 2018), ma anche le tracce (Mujal et al., 2020), fondamentali per comprendere le strategie di locomozione o l'evoluzione degli arti.

I primi ad utilizzare questo approccio furono Tate e Cann (1982), che, nel lavoro *"High-resolution computed tomography for the comparative study of fossil and extant bone",* descrivevano quanto l'uso della Tomografia Computerizzata (CT-scan), diventata ormai di routine in medicina dal 1973, fosse rivoluzionaria anche nell'ambito paleontologico.

Nel corso del tempo, alla tomografia computerizzata si sono affiancate altre tecniche quali: *laser scanner* e l'*imaging* a risonanza magnetica (MRI). I vantaggi sono stati innumerevoli.

Innanzitutto, con strumentazioni sempre più alla portata di tutti, è stato possibile digitalizzare una gran quantità di reperti fossili in modo poco invasivo.

Operando "a distanza", il reperto non viene manipolato in modo eccessivo e questo permette la sua preservazione, senza contare che tale materiale viene poi messo a disposizione e reso *open source* alla comunità scientifica.

Diverse, infatti, sono le piattaforme (**Digimorph, KUPRI, Morphosource, Morphomuseum, Phenome10K, Sketchfab)** che, aggiornando continuamente le loro banche dati, mettono a disposizione migliaia di *mesh 3D*, ovvero superfici tridimensionali che danno ai ricercatori la possibilità di condurre studi di varie entità.

Passiamo dunque alle tecniche di acquisizione. Le più utilizzate sono: CT-scan, MRI, e laser scanner.

Come già accennato, la tecnica di **scansione a tomografia computerizzata** (CT-scan) permette l'osservazione dell'interno di un corpo da ogni sua angolazione.

Basata sulla tecnologia a raggi X, si è largamente sviluppata in ambito medico a partire dagli anni ’70. La sua applicazione in ambito paleontologico è iniziata invece a partire dalla decade successiva (Tate e Cann, 1982; Conroy e Vannier, 1984; Zonnevald e Weber, 1985). Questo perché è stato osservato che il materiale fossile di natura ossea risponde molto bene ai segnali emessi dalla strumentazione (Weber, 2001).

Quest’ultima produce come dato di input un set completo sezioni interne, chiamate *slices* che, in seguito ad opportune tecniche di processamento ricostruiscono un’immagine (Tate e Cann,1982).

Dal momento che l’output è una superficie tridimensionale non si parla più di pixel, ma di **voxel** (Weber, 2001), ciascuno dei quali è indicato da coordinate cartesiane x, y e z.

L’*imaging* a risonanza magnetica (MRI) è un altro metodo basato su impulsi a radiofrequenza e risulta essere particolarmente adatto per campioni *in vivo*, dal momento che lo strumento definisce meglio i tessuti molli anziché le ossa, a differenza della CT-scan (Weber, 2001).

Infine, è da citare la tecnica di laser scanner. Questa differisce dalla tomografia computerizzata in quanto permette di ottenere solo la superficie esterna e non l’oggetto nel suo insieme (Kappelman, 1998). L’output fornito da questa tecnica è una nuvola densa di punti - *dense point cloud* (Aiello et al., 1998) - che sarà poi soggetta a *processing* attraverso appositi software.

Dal momento che una serie di processi biologici possono produrre differenze di forma dovute a malattia, sviluppo ontogenetico, adattamenti o altri fattori geografici (Zelditch, 2004), le superfici tridimensionali rappresentano il punto di partenza per studi di morfometria geometrica (GMM, *Geometric MorphoMetrics*).

La **GMM** è l’approccio moderno della morfometria tradizionale e rappresenta la descrizione statistica quantitativa della variazione di forma (Cardini, 2013). Il passaggio dall’approccio più tradizionale alla morfometria geometrica moderna non è stato netto.

La svolta avvenne a fine anni ’80 quando Bookstein teorizzò matematicamente il concetto di super-imposizione (*superimposition;* Bookstein, 1989). La super-imposizione di Bookstein consiste nel

ridimensionare, ruotare e traslare i campioni esaminati finché i punti di *baseline* (un'unità standard di misura) non risultano sovrapposti.

Col tempo, questo metodo è stato ulteriormente sviluppato ed è attualmente noto come **l'analisi generalizzata di Procruste** (GPA) oppure come la **super-imposizione di Procuste** (Rohlf e Slice, 1990).

La GPA è una procedura importante in quanto rimuove la variazione nella digitalizzazione di posizione, orientamento e scala. Inoltre, sovrappone gli oggetti in un sistema di coordinate comune, per quanto arbitrarie (Adam et al., 2009).

Effettuando studi comparativi su elementi scheletrici di taglia differente, per applicare la super-imposizione è necessario l'uso di punti di riferimento: i **landmark** (Cardini, 2013).

Questi sono punti anatomici discreti che possono essere riconosciuti come gli stessi punti in tutti i campioni di uno studio.

Idealmente, devono soddisfare ben 5 condizioni (Zelditch, 2004):

1. Omologia;
2. Non devono alterare le loro posizioni topologiche rispetto agli altri landmark;
3. Devono permettere un'adeguata copertura della morfologia in esame;
4. Devono essere trovati ripetutamente ed in modo affidabile;
5. Devono giacere su uno stesso piano.

Bookstein elaborò una classificazione di landmark che descrisse nei suoi libri "*Proceedings of the Michigan Morphometrics Workshop"* (1990) e "*Morphometric Tools for Landmark Data"* (1991) basata su 3 categorie: **tipo 1, tipo 2, tipo 3.**

Nel primo tipo rientrano i punti posizionati nelle intersezioni; alcuni esempi sono il **lambda** (punto di convergenza tra la sutura sagittale e sutura lambdoidea nel neurocranio) ed il **bregma** (punto di intersezione tra la sutura coronale e sagittale).

Nella seconda tipologia rientrano i landmark posizionati nei punti di massima curvatura, sia estrusioni che invaginazioni, come artigli o denti.

L'ultimo tipo infine è di natura ibrida perché i suoi valori estremi sono influenzati da valori estremi di curvatura. Esempi di questo tipo sono **glabella** (area depressa tra le arcate sopracciliari), ***gonion*** (vertice dell'angolo che si viene a formare tra il corpo ed il rampo mandibolare) e ***gnation*** (centro delle sinfisi mentoniera) (Wärmländer, 2019; Bookstein 1990,1991).

In sintesi, le analisi quantitative effettuate per gli studi di forma si avvalgono di analisi statistiche di coordinate espresse da punti omologhi, definiti landmarks. Tuttavia, questi presentano una limitazione.

Molte strutture ricurve, come ad esempio il neurocranio, sono difficilmente rappresentabili dai soli landmark, dato che la loro posizione non può essere omologata tra individui diversi.

La soluzione al problema è dunque data dai **semilandmark** (Gunz e Mitteroecker, 2013). Essi fungono da supporto ai landmark nelle analisi quantitative lungo superfici curve, geometricamente omologhe, a 2 o 3 dimensioni.

Per poterli utilizzare, una prima fase del lavoro consiste nel posizionare lo stesso numero di semilandmark in punti, più o meno corrispondenti, su ogni superficie oggetto di analisi. Quest'operazione può essere fatta dall'operatore sia manualmente che in modo semi-automatico.

In secondo luogo, c'è bisogno di ottimizzare la spaziatura tra i semilandmark in modo che "scorrano" lungo le superfici curve. Questo processo prende il nome di *sliding* e permette di stabilire una corrispondenza geometrica tra semilandmark, in modo da eliminare qualsiasi effetto dovuto ad un'arbitraria spaziatura iniziale.

Grazie allo *sliding*, landmark e semilandmark possono essere trattati allo stesso modo nelle analisi statistiche (Gunz e Mitteroecker, 2013).

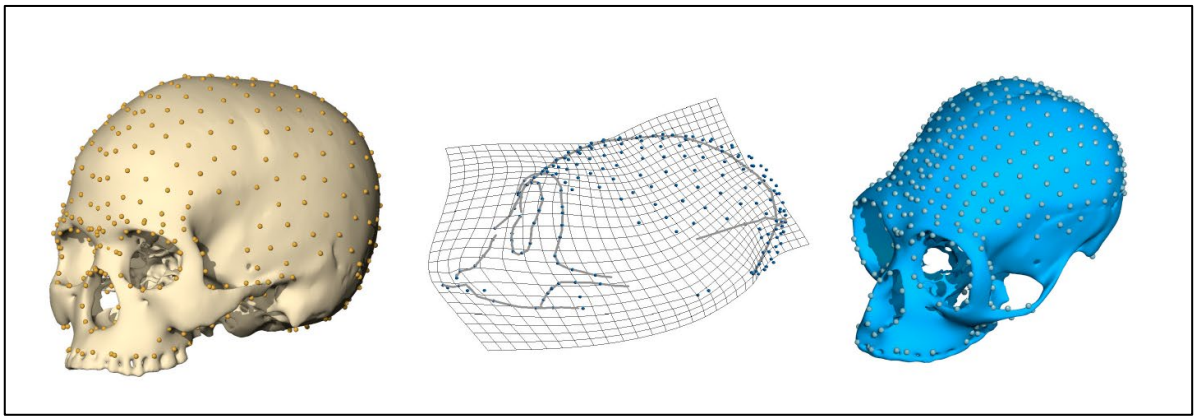

Fig.1. Insieme di landmark e semilandmark sul cranio di *Homo sapiens* (a sinistra) e di un gibbone (a destra). Da Gunz e Mitteroecker, 2013

Quando parliamo delle applicazioni della morfometria geometrica, non ci riferiamo solo alle superfici esterne (ossa), ma anche alle cavità interne; in particolar modo si tratta degli *endocast* o calchi delle cavità cerebrali.

In rari casi la loro formazione è naturale e frutto della litificazione di sedimenti che hanno riempito la cavità cranica, preservando la morfologia cerebrale interna ed esterna (Ivanoff et al., 2014).

Quando ciò non avviene, prima si procedeva con la loro realizzazione manuale e solo adesso con nuove metodologie di acquisizione che ne hanno permesso la realizzazione digitale. Tra gli anni ’60 ed ’80, c’erano cinque diversi modi per ottenere un endocast.

Uno dei primi materiali usati è stato lo Xantopren, un silicone. Poi c’è stato il gesso, versato nella scatola cranica dal *forame magno* dopo aver opportunamente rivestito la superficie ossea interna con gommalacca.

In seguito, l’alginato e successivamente il lattice liquido, diventato poi uno standard in questa procedura. Una variazione delle tecniche sopracitate consisteva nell’uso di paste destinate a protesi dentali (Holloway, 2018).

L’avvento della paleontologia e della paleoantropologia virtuale ha permesso il superamento di queste tecniche decisamente invasive e rischiose, permettendo una mole di dati sempre maggiore ed una disponibilità di informazioni sempre più diffusa nella comunità scientifica.

2. Mammiferi di grossa taglia: i Carnivori

I mammiferi come li conosciamo attualmente sono accomunati da diversi caratteri: peli, ghiandole mammarie, allattamento del piccolo e cervelli relativamente grandi.

Ma non è stato sempre così. Ad esempio, nel tardo Triassico il confine tra mammiferi e no, era davvero sottilissimo.

Filogeneticamente, i mammiferi rientrano in un clade ben più grande: i **sinapsidi**.

Nel Triassico, un gruppo di sinapsidi, i **Cinodonti** (comparsi però già a partire dal Permiano) iniziano ad acquisire, 30-40 Ma fa c.ca, delle modifiche anatomiche che avrebbero portato poi ai mammiferi moderni. Erano individui abbastanza diversificati, presentando sia una dieta carnivora che erbivora.

Perché questi animali sono così importanti? Perché il loro record fossile mostra con estremo dettaglio il passaggio rettili-mammiferi (Benton, 2014) mediante la comparsa delle tre ossa del nostro orecchio medio: **incudine, martello e staffa**.

Questi tre ossicini coinvolti nella conduzione del suono sono in realtà l'a**pomorfia** (ovvero quel carattere morfologico nuovo e frutto dell'evoluzione) dei moderni mammiferi.

Come ogni tratto derivato dall'evoluzione la sua comparsa non è stata netta, ma graduale e consequenziale alla modifica di ossa preesistenti: l'articolazione mascellare dei Cinodonti basali (Allin, 1975; Kemp, 2005; Takechi and Kuratani, 2010; Luo, 2011).

L'articolazione era fatta in questo modo: era posta tra l'**osso quadrato** (molto ridotto) nella mascella e l'**osso articolare** della mandibola.

Da quest'ultimo, presente tuttora nell'articolazione mandibolare di rettili e uccelli, si è evoluto il martello (Ramachandran e Blakeslee, 1999); mentre dal quadrato è derivata l'incudine.

La staffa ha subito un percorso evolutivo differente. A livello embrionale, si sviluppa a partire da uno degli archi branchiali, chiamato epimandibolare o iomandibolare (Chapman, 2011).

Dopo una breve sintesi sull'evoluzione e lo sviluppo dei primi mammiferi, il focus verrà adesso spostato sull'ordine **Carnivora.**

Evolutivamente parlando, il clade di cui fanno parte i carnivori moderni prende il nome di **Carnivoramoprha** e comprende una serie di famiglie sia viventi che estinte.

Si pensava che i moderni carnivori discendessero dai **Creodonti**, ma in realtà la filogenesi di questo clade è piuttosto controversa ed il suo preciso numero di generi e specie è cambiato spesso nel corso del tempo.

Questa presunta incertezza è dovuta al fatto che non si sa ancora bene se le famiglie Oxyaenidae e Hyaenodontidae siano *sister species* e quindi se i Creodonti siano un gruppo monofiletico, oppure no (Morlo, Gunnell & Polly, 2009; Zack, 2011) (in un gruppo monofiletico, tutti gli individui discendono da un antenato comune, a differenza del gruppo polifiletico).

Nel Paleocene (66-56 Ma) i Creodonti dominavano le nicchie ecologiche dei carnivori ed avevano con questi dei tratti comuni, come la presenza dei carnassiali, indice di convergenza evolutiva (Van Valkenburgh, 1999).

Erano animali specialisti, con alcune specie che raggiungevano diete ipercarnivore (Halliday, 2015).

Nell'Eocene (56-33,9 Ma) acquisirono notevoli dimensioni corporee (Gunnel, 1998), ma la loro tendenza alla diversità diminuì drasticamente nell'Oligocene (33,9-23 Ma) (Valkenburgh, 1999; Friscia e Valkenburgh, 2010).

I Carnivoramorpha basali dall'altra parte, includevano vari cladi estinti (Wesley-Hunt e Flynn, 2005; Rose, 2006; Spaulding e Flynn, 2012; Benton, 2014), come Miacidae e Virerravidae, comparsi anch'essi nel Paleocene e presenti fino all'Eocene. Secondo Wang e Tedford (2008) entrambe le famiglie sono comparse in Nord America e si diffusero poi in Asia ed Europa.

All'inizio del Terziario, sia i carnivori basali che i creodonti erano, come accennato, di piccole dimensioni; tanto da poter essere paragonati ad i più moderni viverridi, erpestidi, mustelidi procionidi e/o canidi di piccola taglia (Friscia, 2007).

I carnivori più moderni iniziarono a divergere tra fine Eocene ed inizio Oligocene (Rose, 2006; Agnarsson et al., 2010; Spaulding e Flynn, 2012). I creodonti si estinsero invece a fine Miocene.

Secondo alcuni studiosi la causa principale fu l'esclusione competitiva coi più moderni carnivori, ma dal momento che si tratta di supposizioni, il dibattito resta ancora aperto (Wesley-Hunt, 2005).

Attualmente, l'ordine Carnivora si divide in due sottordini: *Caniformia* e *Feliformia.* Nel primo rientrano le seguenti famiglie: Amphicyonidae (estinta); Ailuridae; Enaliarctidae (estinta); Canidae; Hemicyonidae (estinta); Mephitidae; Mustelidae; Odobenidae; Otariidae; Phocidae; Procyonidae; Ursidae.

Dei *Feliformia* invece fanno parte: Barbourofelidae (estinti); Eupleridae; Felidae; Herpestidae; Hyaenidae; Lophocyonidae (estinti); Nandiinidae; Nimravidae (estinti); Percrocutidae (estinti); Stenoplesictidae (estinti) e Viverridae.

Caratteristica comune a tutti i carnivori è la presenza di un dente carnassiale (o ferino) su ciascun lato delle mascelle. Generalmente è il quarto premolare superiore ed il primo molare inferiore che, insieme, lavorano come le lame di una forbice (Benton, 2014) e sono altamente specializzati per il tagliare e strappare la carne dalle prede al fine della masticazione.

La maggior parte dei carnivori sono terrestri, ma ci sono anche alcune famiglie, facenti parte dei Caniformia, che conducono uno stile di vita acquatico.

Si tratta dei Pinnipedi, una superfamiglia costituita da: Odobenidi (trichechi), Otaridi (otarie) e Focidi (foche).

Tra i gruppi estinti, quelli sicuramente più noti sono gli Amficionidi, i Barburofelidi ed i Nimravidi.

Per il loro aspetto, gli Amficionidi venivano considerati come *bear-dogs.* Era un clade molto diversificato ed il suo record fossile spazia dall'Eocene al Miocene (McKenna e Bell, 1997). Comparvero per la prima volta durante l'Eocene in Nord America, per poi diffondersi in Eurasia ed arrivare in Africa nel Miocene. (Goswami e Friscia, 2010).

Felini robusti e di dimensione molto eterogenea, i Barburofelidi erano animali che si pensava facessero parte della famiglia Felidae, ma in realtà attualmente costituiscono una famiglia filogeneticamente a sé stante e più vicina ai Felidi che ai Nimravidi (Morales et al., 2001; Morlo et al., 2004; Anton, 2013).

Strutturalmente, avevano arti accorciati e possenti muscoli del collo. Il cranio era corto, aveva barre post orbitali e i canini estremamente allungati. I primi resti di questi animali sono stati trovati in Uganda, a Napak e risalgono al Miocene inferiore (Morales et al., 2001). Anche in Europa il record del loro primo insediamento è ascrivibile al Miocene inferiore con specie del genere *Prosansanosmilus* (Morlo et al., 2004).

I Nimravidi, infine, erano una famiglia che comprendeva specie la cui taglia oscillava tra quella di moderno leone e quella di una lince. Si diffusero tra l'Eocene e l'Oligocene in Eurasia e Nord America (Bryant 1996b; Peigné 2003; Morlo et al. 2004).

Se morfologicamente i Nimravidi somigliavano molto ai moderni felini, in realtà rispetto ad essi presentavano una differenza sostanziale nella struttura della *bulla* uditiva, che si trova nella parte esterna del cranio e non all'interno di esso, come nel caso dei primati (Turner, 1997).

I veri felidi (*true cats* in inglese) hanno la *bulla* divisa in due camere da un setto osseo; invece, nei Nimravidi il setto era di natura cartilaginea e per questo assente nel record fossile (Turner, 1997).

3. Materiali e Metodi

Nel corso del triennio ho assemblato un database di 643 campioni, suddivise in 10 ordini e 59 famiglie. Più in dettaglio, di queste, 212 specie sono viventi e 75 fossili. Le superfici sono inoltre distinte in 633 crani e 182 endocast. Per ciascuna specie, qualora possibile, ho campionato un maschio ed una femmina in modo da valutare anche gli effetti del dimorfismo sessuale.

Le banche dati a cui ho attinto per il reperimento del materiale sono state diverse.

Digimorph (http://www.digimorph.org) una libreria digitale che afferisce all'Università di Austin in Texas, il Museo digitale giapponese di Kyoto KUPRI (http://dmm.ehub.kyoto-u.ac.jp), Morphosource (https://www.morphosource.org/) che, con più di 67000 oggetti è supportata dalla Duke University, Phenome10K (https://www.phenome10k.org/), sito ospitato e gestito dal Museo di storia naturale di Londra ed infine Sketchfab (https://sketchfab.com/) piattaforma su cui si possono trovare oggetti 3D destinati a fini scientifici e/o artistici.

Gli oggetti 3D potevano essere scaricati in via completamente libera e gratuita o previa autorizzazione dall'ente che li metteva a disposizione.

Spesso ho dovuto estrarre le superfici, o più semplicemente *mesh* 3D, dalle CT-scan; al fine di ottenere materiale più leggero e manipolabile. Ho quindi usato i software **Amira** (version 5.4.5, Visualization Sciences Group, © 20132), **Mimics research** 21.0 e talvolta, per la rifinitura, rifinite con Geomagic Studio (v.2014.3.0.1781, Geomagic, 2014).

Amira visualizza, analizza e modella i dati tridimensionali, rappresentati come volumi di immagini o superfici geometriche (di forma triangolare o poliedrica). **Mimics** invece si serve delle **DICOM** (***D****igital* ***I****maging and* ***CO****mmunications in* ***M****edicine*), che permettono la comunicazione, visualizzazione, archiviazione e stampa di informazioni di tipo biomedico, quali ad esempio immagini radiologiche. Le analisi statistiche sono state condotte con RStudio.

Pure per l'estrazione degli endocast ed il calcolo dei volumi cerebrali ho usato RStudio e soprattutto il pacchetto **Arothron** (Profico et al. 2021) con la funzione *endomaker* (Profico et al. 2018). La funzione si basa sull'algoritmo **AST-3D** (*automatic segmentation tool for 3D object,* Profico et al.,

2018) che, grazie ad una nuova implementazione (Profico et al., 2020) è in grado di riconoscere automaticamente la cavità endocranica, posizionare i **POVs** (*point of views*) in completa autonomia senza intervento dell'utente.

Quando per altri fattori il software non è stato in grado di riconoscere la cavità endocranica, ho provveduto a posizionare il POVs manualmente, sotto forma di landmark, all'interno di essa. Una volta ottenuto l'endocast allo stato "grezzo" ho poi adoperato nuovamente Geomagic Studio per la pulitura e la rifinitura. Le analisi di morfometria geometrica e filogenetiche sono state condotte in modo analogo sia per i crani che per gli endocast.

Oltre alla procedura prevista dall'uso di *endomaker,* studi sui cambiamenti di forma, sviluppo o comparazione hanno visto l'impiego di landmark e semilandmark, soprattutto trattandosi di specie diverse.

Avendo molti fossili spesso danneggiati per motivi tafonomici, i landmark si sono rivelati utilissimi anche per ripristinare la forma degli oggetti 3D. Per citare alcuni esempi, le funzioni *fiLMmirror* e *retroDeformMesh*, entrambe del pacchetto **Morpho** (Schlager, 2019), si usano rispettivamente per individuare i landmark mancanti a partire dalla loro controparte e retrodeformare e simmetrizzare una mesh.

Per ottenere un campionamento omogeneo e privo di effetti legati non a variazioni di forma (Kendall,1977) allora è stata effettuata la GPA che elimina la variazione di posizione, orientamento e scala. Inoltre, sovrappone gli oggetti in un sistema di coordinate comune, per quanto arbitrarie (Adam et al., 2009). Tra i vantaggi dell'uso di questa metodologia, c'è anche quello di ottenere il *consensus,* cioè la forma media dei campioni.

Per studi filogenetici ho usato invece il pacchetto **RRphylo** (Castiglione et al., 2018) che rientra nei metodi filogenetici comparativi (PCMs). Si sviluppa sulla *phylogenetic ridge regression* (Kratsch & Mchardy 2014; Gubry-Rangin et al. 2015) che consente di stimare i tassi di variazione fenotipica lungo i rami degli alberi filogenetici sia per specie viventi che per i fossili. L'evoluzione del tratto è descritta attraverso la seguente equazione:

$$\boldsymbol{\Delta P = \beta_1 l_1 + \beta_2 l_2 + \cdots + \beta_n l_n}$$

β = coefficiente di regressione del *branch* (ramo) dell'albero considerato nel percorso dal *root* (radice) al *tip* (parte finale).

l = lunghezza del *branch.*

Altra funzione usata che rientra nel pacchetto **RRphylo** è *conv.map*, metodo che permette di studiare pattern di convergenza su superfici 3D. Mappando le regioni responsabili di questi pattern, la funzione permette all'utente di visualizzare il significato funzionale della convergenza nelle strutture biologiche (Melchionna et al., 2021).

Rate.map invece, è un muovo metodo che consente di mappare la variazione del tasso evolutivo agendo sui fenotipi delle superfici 3D e riportando direzione ed entità del cambiamento del tratto (Castiglione et al., 2021).

4. Scopi della ricerca

L'obbiettivo della seguente tesi è dunque verificare quanto propinato dalla SBH ("*The social brain hypothesis",* Dunbar, 1998). Per l'antropologo inglese, esiste una stretta correlazione tra la socialità e l'aumento del grado di encefalizzazione, specialmente della neocorteccia.

Anatomicamente parlando, la neocorteccia (o isocorteccia o *neocortex*) nei mammiferi corrisponde alla sezione di corteccia cerebrale (sezione più esterna del cervello) più recente filogeneticamente.

È la sede adibita a varie funzioni: cognitiva, percettivo-sensoriale, linguaggio, genera i comandi motori ed è sede del ragionamento spaziale. Nell'uomo, rappresenta il 90% circa della superficie cerebrale.

Per ampliare questo campo di ricerca, il mio percorso di dottorato si è articolato seguendo i seguenti obbiettivi:

- Studio in letteratura sui gruppi tassonomici presi in esame;
- Messa a punto di un *database* caratterizzato da specie appartenenti prevalentemente all'ordine Carnivora, ma non solo (sia viventi che fossili);
- Messa a punto di un *database* di *mesh 3D* di crani;
- Realizzazione, laddove possibile, di endocast a partire dalle superfici ottenute;
- Studi di Morfometria Geometrica utilizzando il software RStudio, a partire da *landmark* e *semilandmark*;
- Applicazione di metodi filogenetici comparativi, mediante il software RStudio ed il pacchetto RRPhylo (Raia et al., 2018).

Studi pionieristici sull'argomento sono stati condotti principalmente sui primati (Dunbar, 1998), ma di recente questo settore di studio si è aperto anche a diversi altri taxa.

Finarelli e Flynn (2009), nel loro studio citano l' *Akaike Informazione Criterion;* modello che sfrutta i dati di natura allometrica, come dimensioni corporee e volume endocranico, e le filogenesi delle specie oggetto di studio, ricostruendo l'aumento dell'encefalizzazione tra allometrie parallele.

Perez-Barberia et al., (2007) hanno trovato invece, associazioni statisticamente significative tra socialità e volumi cerebrali maggiori del previsto in ben altri due ordini di mammiferi oltre ai primati, ovvero i Carnivori e gli Artiodattili.

Ciò però non vale per tutte le famiglie. Gli ursidi, ad esempio, sono animali tendenzialmente solitari, così come alcuni gruppi di iene, mentre altri sono estremamente sociali e governate da rigide gerarchie. Lupi e leoni sono altamente sociali, tant'è che vivono in branchi, mentre tigri ed altri felini di più piccole dimensioni conducono stili di vita solitari.

Le analisi condotte nello studio di Perez-Barberia et al. (2007) sono basate sullo studio della dimensione relativa del cervello, in quanto quella assoluta è fortemente correlata alla dimensione corporea, nella maggior parte dei taxa. Tali dimensioni relative vengono calcolate a partire da valori residui del rapporto cervello-corpo attraverso la PGLS (*phylogenetic generalized Least Square*). La PGLS consente di identificare e controllare il grado di autocorrelazione filogenetica (Harvey e Pagel, 1991). Pagel stima il grado di autocorrelazione filogenetica, indicando con 0 l'assenza di autocorrelazione e 1 quando i dati seguono le ipotesi del moto browniano (Paradis et al., 2004).

Data l'estrema eterogeneità tassonomica e comportamentale, questo campo d'indagine risulta ancora del tutto aperto; perciò, in continua evoluzione e pieno di prospettive future.

Variazione fenotipica nei carnivori

In questo primo capitolo illustrerò materiali e metodi per uno studio, in via di definizione, sulla variazione fenotipica nel cranio e negli *endocast* dei mammiferi carnivori.

L'obbiettivo è quello di verificare la presenza di convergenza in gruppi che hanno stili di vita simili, considerando in particolar modo tre fattori: dieta, socialità ed ambiente.

Per mettere appunto il database, sono state scaricate *mesh* 3D e CT-scan dalle seguenti librerie *open source:* Digimorph (http://www.digimorph.org), KUPRI (http://dmm.ehub.kyoto-u.ac.jp), Morphosource (https://www.morphosource.org/), Phenome10K (https://www.phenome10k.org/) ed infine Sketchfab (https://sketchfab.com/).

In totale, sono stati campionati 197 crani, di cui: N = 1 Ailuridae, N= 1 Barbourofelidae, N = 47 Canidae, N = 1 Eupleridae, N = 63 Felidae, N = 7 Herpestidae, N = 9 Hyaenidae, N = 2 Mephitidae, N = 36 Mustelidae, N = 1 Nimravidae, N = 6 Procyonidae, N = 14 Ursidae, N = 9 Viverridae (Tab. 1A). Le superfici sono inclusive di N = 16 specie fossili, ovvero: *Barbourofelis frickii, Aelurodon sp., Borophagus secundus, Canis dirus, Hesperocyon sp., Homotherium serum, Megantereon sp., Panthera atrox, Panthera spelaea, Smilodon fatalis, Smilodon californicus, Yoshi garevskii, Dinictis felina, Arctodus simus, Ursus deningeri* e *Ursus spelaesus*.

Gli *endocast* campionati sono stati invece 87, di cui: N = 1 Ailuridae, N = 14 Canidae, N = 19 Felidae, N = 6 Herpestidae, N = 7 Hyaenidae, N = 3 Mephitidae, N = 21 Mustelidae, N = 6 Procyonidae, N = 6 Ursidae, N = 4 Viverridae (Tab.1B). Anche gli *endocast* sono inclusivi anche di N = 2 specie fossili, ovvero: *Borophagus secundus* e *Yoshi garevskii*.

Id	Family	Specimen	Species	Sex	Diet	Environment	Sociality
PRICT-103-1382	Ailuridae	Ailurus_fulgens_U_PRICT-103-1382	*Ailurus_fulgens*	U	herbivore	closed	solitary
no-id	Barbourofelidae	Barbourofelis_fricki_retro	*Barbourofelis_fricki*	U	sabertooth	open	solitary
UW-2427	Canidae	Aelurodon_sp_U_UW-2427_retro	*Aelurodon_sp*	U	carn-omn	closed	NA
F-AM61640	Canidae	Borophagus_secundus_U_F-AM61640	*Borophagus_secundus*	U	bonecracker	open	NA

SMNS-Z-019005	Canidae	Canis_adustus_F_SMNS-Z-019005	*Canis_adustus*	F	carn-omn	open	family
TM-10907	Canidae	Canis_adustus_M_TM-10907	*Canis_adustus*	M	carn-omn	open	family
SMNS-Z-005014	Canidae	Canis_aureus_F_SMNS-Z-005014	*Canis_aureus*	F	carn-omn	open	solitary
SMNS-Z-005016	Canidae	Canis_aureus_M_SMNS-Z-005016	*Canis_aureus*	M	carn-omn	open	solitary
no-id	Canidae	Canis_dirus_U_no-id	*Canis_dirus*	U	hyper	open	family
NHMUK-1987-1	Canidae	Canis_latrans_F_NHMUK-1987-1	*Canis_latrans*	F	carn-omn	open	family
UV-959	Canidae	Canis_latrans_M_UV-959	*Canis_latrans*	M	carn-omn	open	family
SMNS-Z-051593	Canidae	Canis_lupaster_F_SMNS-Z-051593	*Canis_lupaster*	F	hyper	open	family
MZUF-1851	Canidae	Canis_lupaster_M_MZUF-1851	*Canis_lupaster*	M	hyper	open	family
WAM-M-3831	Canidae	Canis_lupus_dingo_F_WAM-M-3831	*Canis_lupus_dingo*	F	hyper	open	family
WAM-M-5261	Canidae	Canis_lupus_dingo_M_WAM-M-5261	*Canis_lupus_dingo*	M	hyper	open	family
TMN-M-1709	Canidae	Canis_lupus_F_TMN-M-1709	*Canis_lupus*	F	hyper	open	family
PRIZ773	Canidae	Canis_lupus_M_PRIZ773	*Canis_lupus*	M	hyper	open	family
MZUF-1707	Canidae	Canis_mesomelas_F_MZUF-1707	*Canis_mesomelas*	F	carn-omn	open	family
TM-4424	Canidae	Canis_mesomelas_M_TM-4424	*Canis_mesomelas*	M	carn-omn	open	family
NHMUK-1924-8-7-10	Canidae	Canis_simensis_F_NHMUK-1924-8-7-10	*Canis_simensis*	F	carn-omn	open	family
ZMB-MAM-52489	Canidae	Canis_simensis_M_ZMB-MAM-52489	*Canis_simensis*	M	carn-omn	open	family
ZMB-62102	Canidae	Chrysocyon_brachyurus_F_ZMB-62102	*Chrysocyon_brachyurus*	F	carn-omn	open	solitary
ZMB-44198	Canidae	Chrysocyon_brachyurus_M_ZMB-44198	*Chrysocyon_brachyurus*	M	carn-omn	open	solitary
ZMB-56622	Canidae	Cuon_alpinus_F_ZMB-56622	*Cuon_alpinus*	F	hyper	open	family
ZMB-56621	Canidae	Cuon_alpinus_M_ZMB-56621	*Cuon_alpinus*	M	hyper	open	family
UW-15547	Canidae	Hesperocyon_sp_U_UW-15547_adj	*Hesperocyon_sp*	U	carn-omn	open	NA
ZMB-77108	Canidae	Lycalopex_culpaeus_F_ZMB-77108	*Lycalopex_culpaeus*	F	carn-omn	open	solitary
ZMB-77106	Canidae	Lycalopex_culpaeus_M_ZMB-77106	*Lycalopex_culpaeus*	M	carn-omn	open	solitary

ZMB-77035	Canidae	Lycalopex_gymnocercus_F_ZMB-77035	*Lycalopex_gymnocercus*	F	carn-omn	open	solitary
ZMB-77033	Canidae	Lycalopex_gymnocercus_M_ZMB-77033	*Lycalopex_gymnocercus*	M	carn-omn	open	solitary
SMNS-Z-004460	Canidae	Lycaon_pictus_F_SMNS-Z-004460	*Lycaon_pictus*	F	hyper	open	family
TM-47678	Canidae	Lycaon_pictus_M_TM-47678	*Lycaon_pictus*	M	hyper	open	family
PRICT-228-76	Canidae	Nyctereutes_procyonoides_F_PRICT-228-76	*Nyctereutes_procyonoides*	F	omn-carn	closed	solitary
PRIZ-94	Canidae	Nyctereutes_procyonoides_M_PRIZ-94	*Nyctereutes_procyonoides*	M	omn-carn	closed	solitary
TM-27297	Canidae	Otocyon_megalotis_F_TM-27297	*Otocyon_megalotis*	F	insectivore	open	family
USNM-429129	Canidae	Otocyon_megalotis_M_USNM-429129	*Otocyon_megalotis*	M	insectivore	open	family
ZMB-4680	Canidae	Speothos_venaticus_F_ZMB-4680	*Speothos_venaticus*	F	hyper	open	family
SMNS-Z-019136	Canidae	Speothos_venaticus_U_SMNS-Z-019136	*Speothos_venaticus*	U	hyper	open	family
AMNH-255648	Canidae	Urocyon_cinereoargenteus_F_AMNH-255648	*Urocyon_cinereoargenteus*	F	carn-omn	open	solitary
AMNH-1298	Canidae	Urocyon_cinereoargenteus_M_AMNH-1298	*Urocyon_cinereoargenteus*	M	carn-omn	open	solitary
DNMNH-1193	Canidae	Vulpes_chama_M_DNMNH-1193	*Vulpes_chama*	M	carn-omn	open	solitary
SAP-ZOO-136	Canidae	Vulpes_chama_U_SAP-ZOO-136	*Vulpes_chama*	U	carn-omn	open	solitary
ZMB-65305	Canidae	Vulpes_lagopus_F_ZMB-65305	*Vulpes_lagopus*	F	carn-omn	fossorial	family
ZMB-65324	Canidae	Vulpes_lagopus_M_ZMB-65324	*Vulpes_lagopus*	M	carn-omn	fossorial	family
ab0056	Canidae	Vulpes_pallida_U_ab0056	*Vulpes_pallida*	U	carn-omn	fossorial	family
ZMB-49961	Canidae	Vulpes_rueppellii_M_ZMB-49961	*Vulpes_rueppellii*	M	carn-omn	fossorial	family
ZMB-91331	Canidae	Vulpes_rueppellii_U_ZMB-91331	*Vulpes_rueppellii*	U	carn-omn	fossorial	family
PRICT-238-424	Canidae	Vulpes_vulpes_F_PRICT-238-424	*Vulpes_vulpes*	F	carn-omn	open	solitary
PRICT-239-426	Canidae	Vulpes_vulpes_M_PRICT-239-426	*Vulpes_vulpes*	M	carn-omn	open	solitary
SMNS-Z-021615	Eupleridae	Cryptoprocta_ferox_U_SMNS-Z-021615	*Cryptoprocta_ferox*	U	carn-omn	scansorial	solitary
MZUF-1831	Felidae	Acinonyx_jubatus_F_MZUF-1831	*Acinonyx_jubatus*	F	hyper	open	family
MZUF-2135	Felidae	Acinonyx_jubatus_M_MZUF-2135	*Acinonyx_jubatus*	M	hyper	open	family
MNHN_CG1939-687	Felidae	Caracal_aurata_F_MNHN_CG1939-687	*Caracal_aurata*	F	hyper	closed	solitary

MNHN_CG 1940-1213	Felidae	Caracal_aurata_M_MNHN_ CG1940-1213	*Caracal_aurata*	M	hyper	closed	solitary
DNMNH-877	Felidae	Caracal_caracal_F_DNMN H-877	*Caracal_caracal*	F	hyper	open	solitary
MZUF-1752	Felidae	Caracal_caracal_M_MZUF-1752	*Caracal_caracal*	M	hyper	open	solitary
MNHN-CG1939-2152	Felidae	Catopuma_temminckii_F_ MNHN-CG1939-2152	*Catopuma_temminc kii*	F	hyper	closed	solitary
MNHN-CG1962-2927	Felidae	Catopuma_temminckii_M_ MNHN-CG1962-2927	*Catopuma_temminc kii*	M	hyper	closed	solitary
MNHN_CG 2015-1302	Felidae	Felis_chaus_F_MNHN_CG 2015-1302	*Felis_chaus*	F	hyper	closed	solitary
MNHN-CG1995-448	Felidae	Felis_silvestris_F_MNHN-CG1995-448	*Felis_silvestris*	F	hyper	closed	solitary
TM-6154	Felidae	Felis_silvestris_lybica_F_T M-6154	*Felis_silvestris_lybi ca*	F	hyper	closed	solitary
TM-17016	Felidae	Felis_silvestris_lybica_M_T M-17016	*Felis_silvestris_lybi ca*	M	hyper	closed	solitary
SAP-ZOO-84	Felidae	Felis_silvestris_M_SAP-ZOO-84	*Felis_silvestris*	M	hyper	closed	solitary
no-id	Felidae	Homotherium_serum_retro	*Homotherium_seru m*	U	saberto oth	open	solitary
MNHN-CG1897-1261	Felidae	Leopardus_colocolo_F_MN HN-CG1897-1261	*Leopardus_colocolo*	F	hyper	open	solitary
MNHN-CG1912-748	Felidae	Leopardus_geoffroyi_F_M NHN-CG1912-748	*Leopardus_geoffroy i*	F	hyper	open	solitary
MNHN-CG2006-546	Felidae	Leopardus_jacobita_U_MN HN-CG2006-546	*Leopardus_jacobita*	U	hyper	open	solitary
MLP-1913	Felidae	Leopardus_pajeros_U_MLP -1913	*Leopardus_pajeros*	U	hyper	open	solitary
SMNS-Z-006970	Felidae	Leopardus_pardalis_F_SM NS-Z-006970	*Leopardus_pardalis*	F	hyper	closed	solitary
MNHN-CH1902-50	Felidae	Leopardus_pardalis_M_MN HN-CH1902-50	*Leopardus_pardalis*	M	hyper	closed	solitary
MNHN-CG2006-542	Felidae	Leopardus_tigrinus_F_MN HN-CG2006-542	*Leopardus_tigrinus*	F	hyper	closed	solitary
MZUF-4054	Felidae	Leopardus_tigrinus_M_MZ UF-4054_adj	*Leopardus_tigrinus*	M	hyper	closed	solitary
MNHN-CG1995-452	Felidae	Leptailurus_serval_F_MNH N-CG1995-452	*Leptailurus_serval*	F	hyper	open	solitary
MNHN-CG1958-164	Felidae	Leptailurus_serval_M_MN HN-CG1958-164	*Leptailurus_serval*	M	hyper	open	solitary
IMNH-R-213	Felidae	Lynx_canadensis_F_IMNH-R-213	*Lynx_canadensis*	F	hyper	closed	solitary
UWBM-80612	Felidae	Lynx_canadensis_M_UWB M-80612	*Lynx_canadensis*	M	hyper	closed	solitary

MNCN-63887	Felidae	Lynx_issiodorensis_U_MNCN-63887	*Lynx_issiodorensis*	U	hyper	open	NA
MG-2-2013-852	Felidae	Lynx_lynx_F_MG-2-2013-852	*Lynx_lynx*	F	hyper	open	solitary
MG-2-2013-839	Felidae	Lynx_lynx_M_MG-2-2013-839	*Lynx_lynx*	M	hyper	open	solitary
MNCN-16784	Felidae	Lynx_pardinus_U_MNCN-16784	*Lynx_pardinus*	U	hyper	open	solitary
UCLA-10118	Felidae	Lynx_rufus_F_UCLA-10118	*Lynx_rufus*	F	hyper	open	solitary
UWBM-32046	Felidae	Lynx_rufus_M_UWBM-32046	*Lynx_rufus*	M	hyper	open	solitary
Seneze	Felidae	Megantereon_sp_U_Seneze	*Megantereon_sp*	U	saberto oth	open	NA
MNHN_CG1879-2133	Felidae	Neofelis_diardi_M_MNHN_CG1879-2133	*Neofelis_diardi*	M	hyper	scansorial	solitary
MNHN-CG1971-86	Felidae	Neofelis_nebulosa_F_MNHN-CG1971-86	*Neofelis_nebulosa*	F	hyper	scansorial	solitary
MZUF-1024	Felidae	Neofelis_nebulosa_M_MZUF-1024	*Neofelis_nebulosa*	M	hyper	scansorial	solitary
MNHN-CG2009-251	Felidae	Otocolobus_manul_F_MNHN-CG2009-251	*Otocolobus_manul*	F	hyper	open	solitary
MNHN-CG2010-646	Felidae	Otocolobus_manul_M_MNHN-CG2010-646	*Otocolobus_manul*	M	hyper	open	solitary
CB2900-3	Felidae	Panthera_atrox_U_CB2900-3	*Panthera_atrox*	U	hyper	open	family
MNHN-A12259	Felidae	Panthera_leo_F_MNHN-A12259	*Panthera_leo*	F	hyper	open	family
MNHN-CG1938-632	Felidae	Panthera_leo_M_MNHN-CG1938-632	*Panthera_leo*	M	hyper	open	family
MNHN-CG1962-2880	Felidae	Panthera_onca_F_MNHN-CG1962-2880	*Panthera_onca*	F	hyper	closed	solitary
MZUF-501	Felidae	Panthera_onca_M_MZUF-501	*Panthera_onca*	M	hyper	closed	solitary
TM-13276	Felidae	Panthera_pardus_F_TM-13276	*Panthera_pardus*	F	hyper	scansorial	solitary
MNHN-CG1998-1249	Felidae	Panthera_pardus_M_MNHN-CG1998-1249	*Panthera_pardus*	M	hyper	scansorial	solitary
no-id	Felidae	Panthera_spelaea_U_no-id	*Panthera_spelaea*	U	hyper	open	family
MNHN-CG1895-355	Felidae	Panthera_tigris_F_MNHN-CG1895-355	*Panthera_tigris*	F	hyper	closed	solitary
MNHN-CG1985-1860	Felidae	Panthera_tigris_M_MNHN-CG1985-1860	*Panthera_tigris*	M	hyper	closed	solitary
MNHN-CG2016-1664	Felidae	Panthera_uncia_F_MNHN-CG2016-1664	*Panthera_uncia*	F	hyper	open	solitary

MNHN-CG1998-1248	Felidae	Panthera_uncia_M_MNHN-CG1998-1248	*Panthera_uncia*	M	hyper	open	solitary
MNHN-CG1886-25	Felidae	Pardofelis_marmorata_U_MNHN-CG1886-25	*Pardofelis_marmorata*	U	hyper	scansorial	solitary
MNHN-CG1954-293	Felidae	Prionailurus_bengalensis_F_MNHN-CG1954-293	*Prionailurus_bengalensis*	F	hyper	closed	solitary
PRICT-146-774	Felidae	Prionailurus_iriomotensis_M_PRICT-146-774	*Prionailurus_iriomotensis*	M	hyper	scansorial	solitary
MNHN-CG1873-228	Felidae	Prionailurus_planiceps_U_MNHN-CG1873-228	*Prionailurus_planiceps*	U	hyper	closed	solitary
MNHN-CG2015-1300	Felidae	Prionailurus_viverrinus_F_MNHN-CG2015-1300	*Prionailurus_viverrinus*	F	hyper	closed	solitary
UV-4117	Felidae	Puma_concolor_F_UV-4117	*Puma_concolor*	F	hyper	open	solitary
LACM-87430	Felidae	Puma_concolor_M_LACM-87430	*Puma_concolor*	M	hyper	open	solitary
MNHN-CG2001-1292	Felidae	Puma_yagouaroundi_F_MNHN-CG2001-1292	*Puma_yagouaroundi*	F	hyper	closed	solitary
MNHN-CG1966-7	Felidae	Puma_yagouaroundi_M_MNHN-CG1966-7	*Puma_yagouaroundi*	M	hyper	closed	solitary
BCGD-27000	Felidae	Smilodon_californicus_U_BCGD-27000_sym	*Smilodon_californicus*	U	sabertooth	open	solitary
AMNH-14349	Felidae	Smilodon_fatalis_U_AMNH-14349	*Smilodon_fatalis*	U	sabertooth	open	solitary
UW46981	Felidae	Smilodon_fatalis_U_UW46981	*Smilodon_fatalis*	U	sabertooth	open	solitary
MMNH-Sk-69	Felidae	Yoshi_garevskii_U_MMNH-Sk-69_sym	*Yoshi_garevskii*	U	hyper	open	NA
TM-9019	Herpestidae	Atilax_paludinosus_F_TM-9019	*Atilax_paludinosus*	F	omn-carn	acquatic	solitary
TM-20426	Herpestidae	Atilax_paludinosus_M_TM-20426	*Atilax_paludinosus*	M	omn-carn	acquatic	solitary
AMNH-101655	Herpestidae	Herpestes_javanicus_U_AMNH-101655	*Herpestes_javanicus*	U	omn-carn	fossorial	solitary
SMNS-Z-024104	Herpestidae	Herpestes_sanguineus_F_SMNS-Z-024104	*Herpestes_sanguineus*	F	omn-carn	open	solitary
SMNS-Z-004398	Herpestidae	Herpestes_sanguineus_M_SMNS-Z-004398	*Herpestes_sanguineus*	M	omn-carn	open	solitary
MVZ-118450	Herpestidae	Suricata_suricatta_F_MVZ-118450	*Suricata_suricatta*	F	insectivore	fossorial	herd
USNM-384037	Herpestidae	Suricata_suricatta_M_USNM-384037	*Suricata_suricatta*	M	insectivore	fossorial	herd
IMNH-MVZ-165169	Hyaenidae	Crocuta_crocuta_F_IMNH-MVZ-165169	*Crocuta_crocuta*	F	bonecracker	open	herd
IMNH-MVZ-165160	Hyaenidae	Crocuta_crocuta_M_IMNH-MVZ-165160	*Crocuta_crocuta*	M	bonecracker	open	herd

USNM-182034	Hyaenidae	Hyaena_hyaena_M_USNM-182034	*Hyaena_hyaena*	M	bonecracker	open	family
no-id	Hyaenidae	Hyaena_hyaena_U_no-id	*Hyaena_hyaena*	U	bonecracker	open	family
DNMNH-56B	Hyaenidae	Parahyaena_brunnea_F_DNMNH-56B	*Parahyaena_brunnea*	F	bonecracker	open	group
FMNH-34584	Hyaenidae	Parahyaena_brunnea_M_FMNH-34584	*Parahyaena_brunnea*	M	bonecracker	open	group
MM91	Hyaenidae	Parahyaena_brunnea_U_MM91	*Parahyaena_brunnea*	U	bonecracker	open	group
TM-37169	Hyaenidae	Proteles_cristata_F_TM-37169	*Proteles_cristata*	F	insectivore	open	solitary
J050607T02	Hyaenidae	Proteles_cristata_U_J050607T02	*Proteles_cristata*	U	insectivore	open	solitary
J4240_52um	Mephitidae	Mephitis_macroura_U_J4240_53um	*Mephitis_macroura*	U	carn-omn	fossorial	solitary
AMNH-17213	Mephitidae	Mephitis_mephitis_U_AMNH-17213	*Mephitis_mephitis*	U	carn-omn	fossorial	solitary
AMNH-M-101638	Mustelidae	Aonyx_cinereus_M_AMNH-M-101638	*Aonyx_cinereus*	M	sea food	acquatic	group
CG_2000_646	Mustelidae	Eira_barbara_U_CG_2000_646_sym	*Eira_barbara*	U	carn-omn	scansorial	solitary
AMNH-M-24186	Mustelidae	Enhydra_lutris_M_AMNH-M-24186	*Enhydra_lutris*	M	sea food	acquatic	solitary
FW-1506	Mustelidae	Enhydra_lutris_U_FW-1506	*Enhydra_lutris*	U	sea food	acquatic	solitary
AMNH-M-37433	Mustelidae	Gulo_gulo_luscus_F_AMNH-M-37433	*Gulo_gulo_luscus*	F	carn-omn	fossorial	solitary
AMNH-M-182936	Mustelidae	Gulo_gulo_luscus_M_AMNH-M-182936	*Gulo_gulo_luscus*	M	carn-omn	fossorial	solitary
FW-3174	Mustelidae	Gulo_gulo_U_FW-3174	*Gulo_gulo*	U	carn-omn	fossorial	solitary
no-id	Mustelidae	Gulo_gulo_U_no-id	*Gulo_gulo*	U	carn-omn	fossorial	solitary
AMNH-M-89807	Mustelidae	Hydrictis_maculicollis_M_AMNH-M-89807	*Hydrictis_maculicollis*	M	sea food	acquatic	solitary
AMNH-M-254476	Mustelidae	Lontra_canadensis_M_AMNH-M-254476	*Lontra_canadensis*	M	sea food	acquatic	solitary
FW-6091	Mustelidae	Lontra_canadensis_U_FW-6091	*Lontra_canadensis*	U	sea food	acquatic	solitary
AMNH-M-48193	Mustelidae	Lontra_felina_U_AMNH-M-48193	*Lontra_felina*	U	sea food	acquatic	solitary
AMNH-M-98589	Mustelidae	Lontra_longicaudis_M_AMNH-M-98589	*Lontra_longicaudis*	M	sea food	acquatic	solitary
AMNH-M-206592	Mustelidae	Lutra_lutra_M_AMNH-M-206592	*Lutra_lutra*	M	sea food	acquatic	solitary
PRICT-1341-2070	Mustelidae	Lutra_lutra_U_PRICT-1341-2070	*Lutra_lutra*	U	sea food	acquatic	solitary
AMNH-M-204747	Mustelidae	Lutrogale_perspicillata_M_AMNH-M-204747	*Lutrogale_perspicillata*	M	sea food	acquatic	family

1897_422	Mustelidae	Lyncodon_patagonicus_U_1897_422	*Lyncodon_patagonicus*	U	carn-omn	open	solitary
FW-3253	Mustelidae	Martes_americana_U_FW-3253	*Martes_americana*	U	carn-omn	scansorial	solitary
MSB-Mamm-216253	Mustelidae	Martes_caurina_M_MSB-Mamm-216253	*Martes_caurina*	M	carn-omn	scansorial	solitary
no-id	Mustelidae	Martes_foina_U_no-id	*Martes_foina*	U	carn-omn	scansorial	solitary
SMNS-Z-046570	Mustelidae	Martes_martes_F_SMNS-Z-046570	*Martes_martes*	F	carn-omn	scansorial	solitary
SMNS-Z-021808	Mustelidae	Martes_martes_M_SMNS-Z-021808	*Martes_martes*	M	carn-omn	scansorial	solitary
PRICT-253-604	Mustelidae	Martes_melampus_M_PRICT-253-604	*Martes_melampus*	M	omn-carn	scansorial	solitary
AMNH-M-57117	Mustelidae	Meles_meles_F_AMNH-M-57117	*Meles_meles*	F	omn-carn	fossorial	group
AMNH-M-70603	Mustelidae	Meles_meles_M_AMNH-M-70603	*Meles_meles*	M	omn-carn	fossorial	group
JM8543_53um	Mustelidae	Mustela_frenata_U_JM8543_53um	*Mustela_frenata*	U	carn-omn	open	solitary
PAS_35262	Mustelidae	Mustela_nivalis_F_PAS_35262	*Mustela_nivalis*	F	carn-omn	closed	solitary
J13253_53um	Mustelidae	Mustela_putorius_U_J13253_53um	*Mustela_putorius*	U	carn-omn	open	solitary
IMNH-R-103	Mustelidae	Mustela_vison_U_IMNH-R-103	*Mustela_vison*	U	carn-omn	acquatic	solitary
FW-3188	Mustelidae	Pekania_pennanti_U_FW-3188	*Pekania_pennanti*	U	carn-omn	closed	solitary
CG-1934-107	Mustelidae	Poecilogale_albinucha_U_CG-1934-107	*Poecilogale_albinucha*	U	carn-omn	fossorial	solitary
AMNH-M-30191	Mustelidae	Pteronura_brasiliensis_F_AMNH-M-30191	*Pteronura_brasiliensis*	F	sea food	acquatic	family
Z-1716	Mustelidae	Pteronura_brasiliensis_U_Z-1716	*Pteronura_brasiliensis*	U	sea food	acquatic	family
LACM-45012	Mustelidae	Taxidea_taxus_F_LACM-45012	*Taxidea_taxus*	F	carn-omn	fossorial	solitary
UCLA-14841	Mustelidae	Taxidea_taxus_M_UCLA-14841	*Taxidea_taxus*	M	carn-omn	fossorial	solitary
JM1044_53um	Mustelidae	Vormela_peregusna_U_JM1044_53um	*Vormela_peregusna*	U	carn-omn	fossorial	solitary
RAM-6911	Nimravidae	Dinictis_felina_U_RAM-6911	*Dinictis_felina*	U	sabertooth	open	solitary
MSB-Mamm-46326	Procyonidae	Bassariscus_astutus_F_MSB-Mamm-46326	*Bassariscus_astutus*	F	omn-carn	open	solitary
IMNHR-2580	Procyonidae	Bassariscus_astutus_U_IMNHR-2580	*Bassariscus_astutus*	U	omn-carn	open	solitary
USNM-337630	Procyonidae	Potos_flavus_F_USNM-337630	*Potos_flavus*	F	omn-carn	scansorial	solitary

USNM-291066	Procyonidae	Potos_flavus_M_USNM-291066	*Potos_flavus*	M	omn-carn	scansorial	solitary
INHS-7241	Procyonidae	Procyon_lotor_F_INHS-7241	*Procyon_lotor*	F	omn-carn	scansorial	solitary
LACM-052261	Procyonidae	Procyon_lotor_M_LACM-052261	*Procyon_lotor*	M	omn-carn	scansorial	solitary
AMNH-M-89030	Ursidae	Ailuropoda_melanoleuca_F_AMNH-M-89030	*Ailuropoda_melanoleuca*	F	herbivore	closed	solitary
MAV-3156	Ursidae	Ailuropoda_melanoleuca_M_MAV-3156	*Ailuropoda_melanoleuca*	M	herbivore	closed	solitary
no-id	Ursidae	Arctodus_simus_U_no-id	*Arctodus_simus*	U	carn-omn	open	solitary
MNHN-CG1992-1469	Ursidae	Tremarctos_ornatus_F_MNHN-CG1992-1469	*Tremarctos_ornatus*	F	omn-carn	closed	solitary
UV-4884	Ursidae	Ursus_americanus_F_UV-4884	*Ursus_americanus*	F	omn-carn	closed	solitary
UWBM-33259	Ursidae	Ursus_americanus_M_UWBM-33259	*Ursus_americanus*	M	omn-carn	closed	solitary
UV-7028	Ursidae	Ursus_arctos_horribilis_F_UV-7028	*Ursus_arctos_horribilis*	F	omn-carn	closed	solitary
9	Ursidae	Ursus_arctos_horribilis_M_9	*Ursus_arctos_horribilis*	M	omn-carn	closed	solitary
ISPRA-1420	Ursidae	Ursus_arctos_M_ISPRA-1420	*Ursus_arctos*	M	omn-carn	closed	solitary
ISPRA-354	Ursidae	Ursus_marsicanus_F_ISPRA-354	*Ursus_marsicanus*	F	herbivore	closed	solitary
no-id	Ursidae	Ursus_deningeri_U_no-id_adj	*Ursus_deningeri*	U	omn-carn	closed	solitary
UWBM-31586	Ursidae	Ursus_maritimus_F_UWBM-31586	*Ursus_maritimus*	F	carn-omn	open	solitary
ISM-001-05	Ursidae	Ursus_maritimus_M_ISM-001-05	*Ursus_maritimus*	M	carn-omn	open	solitary
MSMN-V368	Ursidae	Ursus_spelaeus_U_MSMN-V368	*Ursus_spelaeus*	U	herbivore	closed	solitary
TM-26705	Viverridae	Civettictis_civetta_F_TM-26705	*Civettictis_civetta*	F	carn-omn	closed	solitary
TM-3174	Viverridae	Civettictis_civetta_M_TM-3174	*Civettictis_civetta*	M	carn-omn	closed	solitary
MNHN-ZM-MO-1997-450	Viverridae	Genetta_genetta_U_MNHN-ZM-MO-1997-450	*Genetta_genetta*	U	carn-omn	fossorial	solitary
SMNS-Z-004412	Viverridae	Genetta_maculata_F_SMNS-Z-004412	*Genetta_maculata*	F	carn-omn	fossorial	solitary
SMNS-Z-004427	Viverridae	Genetta_maculata_M_SMNS-Z-004427	*Genetta_maculata*	M	carn-omn	fossorial	solitary
PRICT-756-1901	Viverridae	Paguma_larvata_U_PRICT-756-1901	*Paguma_larvata*	U	omn-carn	scansorial	solitary
MNHN-ZM-AC-A3448	Viverridae	Paradoxurus_hermaphroditus_U_MNHN-ZM-AC-A3448	*Paradoxurus_hermaphroditus*	U	omn-carn	scansorial	solitary

USNM303036	Viverridae	Prionodon_linsang_M_USNM303036	*Prionodon_linsang*	M	carn-omn	scansorial	solitary
WAM-M-30616	Viverridae	Viverricula_indica_U_WAM-M-30616	*Viverricula_indica*	U	carn-omn	open	solitary

Tab.1A Elenco delle superfici 3D con dati relativi a dieta, ambiente e socialità.

ID	Family	Specimen	Species	Sex	Diet	Environment	Sociality
PRICT-103-1382	Ailuridae	Ailurus_fulgens_U_PRICT-103-1382	*Ailurus_fulgens*	U	herbivore	closed	solitary
F-AM61640	Canidae	Borophagus_secundus_U_F-AM61640	*Borophagus_secundus*	U	bonecracker	open	NA
TM-10907	Canidae	Canis_adustus_M_TM-10907	*Canis_adustus*	M	carn-omn	open	family
TMN-M-1709	Canidae	Canis_lupus_F_TMN-M-1709	*Canis_lupus*	F	hyper	open	family
UAM-28826	Canidae	Canis_lupus_M_UAM-28826	*Canis_lupus*	M	hyper	open	family
DNMNH-24017	Canidae	Canis_mesomelas_F_DNMNH-24017	*Canis_mesomelas*	F	carn-omn	open	family
TM-4424	Canidae	Canis_mesomelas_M_TM-4424	*Canis_mesomelas*	M	carn-omn	open	family
TM-47678	Canidae	Lycaon_pictus_M_TM-47678	*Lycaon_pictus*	M	hyper	open	family
PRICT-228-76	Canidae	Nyctereutes_procyonoides_F_PRICT-228-76	*Nyctereutes_procyonoides*	F	omn-carn	closed	solitary
PRIZ-94	Canidae	Nyctereutes_procyonoides_M_PRIZ-94	*Nyctereutes_procyonoides*	M	omn-carn	closed	solitary
TM-27297	Canidae	Otocyon_megalotis_F_TM-27297	*Otocyon_megalotis*	F	insectivore	open	family
USNM-429129	Canidae	Otocyon_megalotis_M_USNM-429129	*Otocyon_megalotis*	M	insectivore	open	family
DNMNH-1493	Canidae	Vulpes_chama_M_DNMNH-1493	*Vulpes_chama*	M	carn-omn	open	solitary
PRICT-238-424	Canidae	Vulpes_vulpes_F_PRICT-238-424	*Vulpes_vulpes*	F	carn-omn	open	solitary
PRIZ-409	Canidae	Vulpes_vulpes_M_PRIZ-409	*Vulpes_vulpes*	M	carn-omn	open	solitary
DNMNH-1217	Felidae	Acinonyx_jubatus_F_DNMNH-1217	*Acinonyx_jubatus*	F	hyper	open	family
FMNH-29635	Felidae	Acinonyx_jubatus_M_FMNH-29635	*Acinonyx_jubatus*	M	hyper	open	family
DNMNH-877	Felidae	Caracal_caracal_F_DNMNH-877	*Caracal_caracal*	F	hyper	open	solitary
TM-15719	Felidae	Caracal_caracal_M_TM-15719	*Caracal_caracal*	M	hyper	open	solitary
TM-6154	Felidae	Felis_silvestris_lybica_F_TM-6154	*Felis_silvestris_lybica*	F	hyper	closed	solitary

TM-17016	Felidae	Felis_silvestris_lybica_M_TM-17016	*Felis_silvestris_lybica*	M	hyper	closed	solitary
010608-SW	Felidae	Felis_silvestris_U_010608-SW	*Felis_silvestris*	U	hyper	closed	solitary
LACM-25127	Felidae	Leopardus_pardalis_M_LACM-25127	*Leopardus_pardalis*	M	hyper	closed	solitary
DNMNH-93	Felidae	Leptailurus_serval_U_DNMNH-93	*Leptailurus_serval*	U	hyper	open	solitary
UCLA-10118	Felidae	Lynx_rufus_F_UCLA-10118	*Lynx_rufus*	F	hyper	open	solitary
OUVC-9576	Felidae	Lynx_rufus_U_OUVC-9576	*Lynx_rufus*	U	hyper	open	solitary
030608-SW	Felidae	Neofelis_nebulosa_U_030608-SW	*Neofelis_nebulosa*	U	hyper	scansorial	solitary
MMNH-17533	Felidae	Panthera_leo_F_MMNH-17533	*Panthera_leo*	F	hyper	open	family
MMNH-17537	Felidae	Panthera_leo_M_MMNH-17537	*Panthera_leo*	M	hyper	open	family
PRICT-148-890	Felidae	Panthera_onca_U_PRICT-148-890	*Panthera_onca*	U	hyper	closed	solitary
TM-13276	Felidae	Panthera_pardus_F_TM-13276	*Panthera_pardus*	F	hyper	scansorial	solitary
LACM-87430	Felidae	Puma_concolor_M_LACM-87430	*Puma_concolor*	M	hyper	open	solitary
PRICT-645-891	Felidae	Puma_concolor_U_PRICT-645-891	*Puma_concolor*	U	hyper	open	solitary
MMNH-Sk-69	Felidae	Yoshi_garevskii_U_MMNH-Sk-69	*Yoshi_garevskii*	U	hyper	open	NA
TM-9019	Herpestidae	Atilax_paludinosus_F_TM-9019	*Atilax_paludinosus*	F	omn-carn	acquatic	solitary
TM-20426	Herpestidae	Atilax_paludinosus_M_TM-20426	*Atilax_paludinosus*	M	omn-carn	acquatic	solitary
AMNH-101655	Herpestidae	Herpestes_javanicus_U_AMNH-101655	*Herpestes_javanicus*	U	omn-carn	fossorial	solitary
USNM-539732	Herpestidae	Herpestes_sanguineus_M_USNM-539732	*Herpestes_sanguineus*	M	omn-carn	open	solitary
MVZ-118450	Herpestidae	Suricata_suricatta_F_MVZ-118450	*Suricata_suricatta*	F	insectivore	fossorial	herd
USNM-384037	Herpestidae	Suricata_suricatta_M_USNM-384037	*Suricata_suricatta*	M	insectivore	fossorial	herd
TM-3269	Hyaenidae	Crocuta_crocuta_F_TM-3269	*Crocuta_crocuta*	F	bonecracker	open	herd
TM-19370	Hyaenidae	Crocuta_crocuta_M_TM-19370	*Crocuta_crocuta*	M	bonecracker	open	herd
USNM-182034	Hyaenidae	Hyaena_hyaena_M_USNM-182034	*Hyaena_hyaena*	M	bonecracker	open	family
DNMNH-56B	Hyaenidae	Parahyaena_brunnea_F_DNMNH-56B	*Parahyaena_brunnea*	F	bonecracker	open	group
FMNH-34584	Hyaenidae	Parahyaena_brunnea_M_FMNH-34584	*Parahyaena_brunnea*	M	bonecracker	open	group

TM-37169	Hyaenidae	Proteles_cristata_F_TM-37169	*Proteles_cristata*	F	insectivore	open	solitary
DNMNH-2152	Hyaenidae	Proteles_cristata_M_DNMNH-2152	*Proteles_cristata*	M	insectivore	open	solitary
MSB-68560	Mephitidae	Conepatus_leuconotus_U_MSB-68560	*Conepatus_leuconotus*	U	omn-carn	open	solitary
J4240_53um	Mephitidae	Mephitis_macroura_U_J4240_53um	*Mephitis_macroura*	U	carn-omn	fossorial	solitary
I-ahr	Mephitidae	Mephitis_mephitis_U_I-ahr	*Mephitis_mephitis*	U	carn-omn	fossorial	solitary
CMNH-VZ-17620	Mustelidae	Aonyx_capensis_U_CMNH-VZ-17620	*Aonyx_capensis*	U	sea food	acquatic	group
AMNH-M-37433	Mustelidae	Gulo_gulo_luscus_F_AMNH-M-37433	*Gulo_gulo_luscus*	F	carn-omn	fossorial	solitary
AMNH-M-182936	Mustelidae	Gulo_gulo_luscus_M_AMNH-M-182936	*Gulo_gulo_luscus*	M	carn-omn	fossorial	solitary
AMNH-M-254476	Mustelidae	Lontra_canadensis_M_AMNH-M-254476	*Lontra_canadensis*	M	sea food	acquatic	solitary
AMNH-M-48193	Mustelidae	Lontra_felina_U_AMNH-M-48193	*Lontra_felina*	U	sea food	acquatic	solitary
PRICT-1341-2070	Mustelidae	Lutra_lutra_U_PRICT-1341-2070	*Lutra_lutra*	U	sea food	acquatic	solitary
AMNH-M-204747	Mustelidae	Lutrogale_perspicillata_M_AMNH-M-204747	*Lutrogale_perspicillata*	M	sea food	acquatic	family
MSB-Mamm-216253	Mustelidae	Martes_caurina_M_MSB-Mamm-216253	*Martes_caurina*	M	carn-omn	scansorial	solitary
no-id	Mustelidae	Martes_foina_U_no-id	*Martes_foina*	U	carn-omn	scansorial	solitary
PRICT-253-604	Mustelidae	Martes_melampus_M_PRICT-253-604	*Martes_melampus*	M	omn-carn	scansorial	solitary
AMNH-M-57117	Mustelidae	Meles_meles_F_AMNH-M-57117	*Meles_meles*	F	omn-carn	fossorial	group
AMNH-M-70603	Mustelidae	Meles_meles_M_AMNH-M-70603	*Meles_meles*	M	omn-carn	fossorial	group
JM8543_53um	Mustelidae	Mustela_frenata_U_JM8543_53um	*Mustela_frenata*	U	carn-omn	open	solitary
PAS_35262	Mustelidae	Mustela_nivalis_F_PAS_35262	*Mustela_nivalis*	F	carn-omn	closed	solitary
AMNH-M-243106	Mustelidae	Mustela_putorius_F_AMNH-M-243106	*Mustela_putorius*	F	carn-omn	open	solitary
J13253_53um	Mustelidae	Mustela_putorius_U_J13253_53um	*Mustela_putorius*	U	carn-omn	open	solitary
AMNH-M-30191	Mustelidae	Pteronura_brasiliensis_F_AMNH-M-30191	*Pteronura_brasiliensis*	F	sea food	acquatic	family
AMNH-M-98594	Mustelidae	Pteronura_brasiliensis_M_AMNH-M-98594	*Pteronura_brasiliensis*	M	sea food	acquatic	family
LACM-45012	Mustelidae	Taxidea_taxus_F_LACM-45012	*Taxidea_taxus*	F	carn-omn	fossorial	solitary

UCLA-14841	Mustelidae	Taxidea_taxus_M_UCLA-14841	*Taxidea_taxus*	M	carn-omn	fossorial	solitary
JM1044_53um	Mustelidae	Vormela_peregusna_U_JM1044_53um	*Vormela_peregusna*	U	carn-omn	fossorial	solitary
MSB-Mamm-46326	Procyonidae	Bassariscus_astutus_F_MSB-Mamm-46326	*Bassariscus_astutus*	F	omn-carn	open	solitary
DU-BAA-RFK-49	Procyonidae	Nasua_narica_U_DU-BAA-RFK-49	*Nasua_narica*	U	omn-carn	closed	group
USNM-337630	Procyonidae	Potos_flavus_F_USNM-337630	*Potos_flavus*	F	omn-carn	scansorial	solitary
USNM-291066	Procyonidae	Potos_flavus_M_USNM-291066	*Potos_flavus*	M	omn-carn	scansorial	solitary
INHS-7241	Procyonidae	Procyon_lotor_F_INHS-7241	*Procyon_lotor*	F	omn-carn	scansorial	solitary
LACM-052261	Procyonidae	Procyon_lotor_M_LACM-052261	*Procyon_lotor*	M	omn-carn	scansorial	solitary
MAV-3156	Ursidae	Ailuropoda_melanoleuca_M_MAV-3156	*Ailuropoda_melanoleuca*	M	herbivore	closed	solitary
no-id	Ursidae	Helarctos_malayanus_U_no-id	*Helarctos_malayanus*	U	omn-carn	closed	solitary
USNM-227070	Ursidae	Ursus_americanus_M_USNM-227070	*Ursus_americanus*	M	omn-carn	closed	solitary
AMNH-M-34408	Ursidae	Ursus_arctos_U_AMNH-M-34408	*Ursus_arctos*	U	omn-carn	closed	solitary
ISM-001-05	Ursidae	Ursus_maritimus_M_ISM-001-05	*Ursus_maritimus*	M	carn-omn	open	solitary
TM-26705	Viverridae	Civettictis_civetta_F_TM-26705	*Civettictis_civetta*	F	carn-omn	closed	solitary
TM-3174	Viverridae	Civettictis_civetta_M_TM-3174	*Civettictis_civetta*	M	carn-omn	closed	solitary
PRICT-756-1901	Viverridae	Paguma_larvata_U_PRICT-756-1901	*Paguma_larvata*	U	omn-carn	scansorial	solitary
USNM303036	Viverridae	Prionodon_linsang_M_USNM303036	*Prionodon_linsang*	M	carn-omn	scansorial	solitary

Tab.1B Elenco degli *endocast* 3D con dati relativi a dieta, ambiente e socialità.

Sono stati inoltre reperiti in letteratura i dati relativi alla dieta, tipo di ambiente e socialità (Tab. 1; Tab.2). La presenza di NA della colonna "**Sociality**" è indicativa dell'assenza momentanea di dati. Spesso il materiale 3D si trovava sotto forma di scansione. Allora, ho provveduto ad estrarre manualmente le superfici 3D, in formato .ply, usando i seguenti software: **Amira** (version 5.4.5, Visualization Sciences Group, © 20132) e **Mimics research** 21.0. Quando il risultato ottenuto

presentava delle imperfezioni dovute al processo di estrazione, per la rifinitura ho utilizzato il software Geomagic Studio (v.2014.3.0.1781, Geomagic, 2014).

Alcune superfici tridimensionali di crani (soprattutto di specie fossili, ma non solo) presentavano distorsioni, difetti o vacanze.

Per risolvere questo problema, abbiamo utilizzato il software RStudio ed in particolar modo alcune funzioni presenti nel pacchetto **Morpho** (Schlager, 2017).

Nel caso dei fossili, ad esempio, le parti mancanti erano dovute all'azione di processi tafonomici. Per cui abbiamo utilizzato la funzione *retroDeformMesh* del pacchetto **Morpho** che permette di simmetrizzare una mesh 3D triangolare (Schlager, 2017).

Anche gli *endocast* sono stati estratti su RStudio, utilizzando il pacchetto **Arothron** (Profico et al., 2021) e la funzione *endomaker* (Profico et al., 2020). Ottenuti gli *endocast,* questi sono stati sottoposti a processi di post-produzione al fine di eliminare tutte le imperfezioni dovute all'uso di questa tecnica. Per farlo, ho utilizzato il software Geomagic Studio (v.2014.3.0.1781, Geomagic, 2014) (Fig.2).

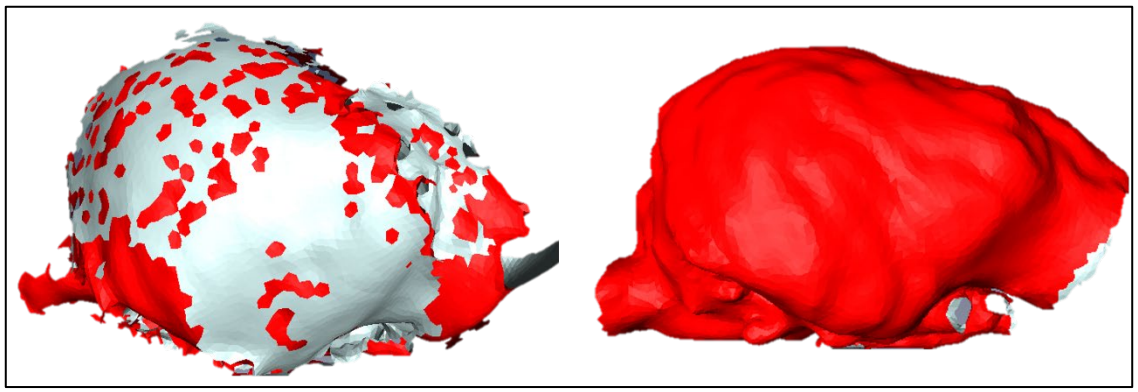

Fig. 2. Prima e dopo il processo di rifinitura e pulitura *endocast,* mediante l'uso del software Geomagic Studio (v.2014.3.0.1781, Geomagic, 2014). La specie in questione è *Canis lupus.*

Al fine di poter effettuare opportune analisi morfometriche sui dati raccolti, è stato fondamentale il ricorso a landmark e semilandmark.

I primi sono punti di riferimento che servono per descrivere strutture biologiche che differiscono in modo sostanziale nella forma; indicano cioè l'omologia tra due immagini in un dataset (Bookstein, 1991). I semilandmark fungono invece, da supporto ai landmark nelle analisi quantitative lungo superfici curve, geometricamente omologhe, a 2 o 3 dimensioni (Gunz e Mitteroecker, 2013).

Come accennato nella sezione introduttiva di questa tesi, per usare i semilandmark bisogna posizionarli in punti più o meno corrispondenti di ogni superficie oggetto di analisi; attività che può essere fatta sia manualmente che in modo semi-automatico dall'operatore.

Si procede poi ad effettuare la procedura di *sliding,* che serve per ottimizzare la spaziatura tra i semilandmark in modo che "scorrano" lungo le superfici curve. Questo processo permette di stabilire una corrispondenza geometrica tra semilandmark, in modo da eliminare qualsiasi effetto dovuto ad un'arbitraria spaziatura iniziale. Grazie allo *sliding*, landmark e semilandmark possono essere trattati allo stesso modo nelle analisi statistiche (Gunz e Mitteroecker, 2013).

Nel nostro set di campioni abbiamo posizionato 48 landmark sui crani (Tab.2A; Fig. 3A) e 18 sugli endocast (Tab.2B; Fig.3B). Inoltre, sono stati posizionati 200 semilandmark (100 a lato) sulle superfici craniche, mentre 120 sugli endocast; di cui 50 per lato sul neurocranio e 10 per lato sul cervelletto.

N	Description
1	Most anterior midline point of the nasals
2	Most anterior, dorsal midline point of the premaxillae (dx)
3	Most anterior, dorsal midline point of the premaxillae (sx)
4	Nasal-premaxilla notch (dx)
5	Nasal-premaxilla notch(sx)
6	Most anterior point of the cheek-tooth row (dx)
7	Most anterior point of the cheek-tooth row (sx)
8	Most posterior point of the infraorbital foramen (dx)
9	Most posterior point of the infraorbital foramen (sx)
10	Contact fourth premolar-fist molar (dx)
11	Contact fourth premolar-fist molar (sx)
12	Zygomatico-maxillo-lachrymal junction (dx)
13	Zygomatico-maxillo-lachrymal junction (sx)
14	Most ventral point of the zygomatic-maxilla suture (dx)
15	Most ventral point of the zygomatic-maxilla suture (sx)
16	Most anterior lateral point of the orbit (dx)
17	Most anterior lateral point of the orbit (sx)
18	Frontolacrimal junction (dx)
19	Frontolacrimal junction (sx)
20	Frontonasal suture (dx)
21	Frontonasal suture (sx)
22	Frontonasal suture
23	Most dorsal point of the orbit (dx)
24	Most dorsal point of the orbit (sx)

25	End of the zygomatic arch (dx)
26	End of the zygomatic arch (sx)
27	Most ventral point of supraorbital process of the frontal bone (dx)
28	Most ventral point of supraorbital process of the frontal bone (sx)
29	Start zygomatic suture (dx)
30	Start zygomatic suture (sx)
31	End zygomatic suture (dx)
32	End zygomatic suture (sx)
33	Most anterior, lateral point of the nuchal crest (dx)
34	Most anterior, lateral point of the nuchal crest (sx)
35	Nuchal crest
36	Lambda
37	Bregma
38	Mastoid process (dx)
39	Mastoid process (sx)
40	Most posterior point of the cheek-tooth row (dx)
41	Most posterior point of the cheek-tooth row (sx)
42	Most posterior point of the foramen magnum
43	Most anterior point of the foramen magnum
44	Most lateral point of the occipital condyle (dx)
45	Most lateral point of the occipital condyle (sx)
46	Vomer
47	Most anterior point of the coanae fossa (dx)
48	Most anterior point of the coanae fossa (sx)

Tab. 2A. Numero e configurazione dei landmarks sul superfici 3D di crani

N	Descrizione
1	Anterior end of the cribriform plate in the sagittal plane
2	Ventral end of the cribriform plate in the sagittal plane
3	Uppermost point of the olfactory bulb (dx)
4	Uppermost point of the olfactory bulb (sx)
5	Frontal pole (dx)
6	Frontal pole (sx)
7	Temporal pole (dx)
8	Temporal pole (sx)
9	The most inferior point between the two occipital lobes on the midsagittal plane
10	Occipital pole (dx)
11	Occipital pole (sx)
12	Endobregma
13	Cerebellar pole (dx)
14	Cerebellar pole (sx)
15	Flocculus (sx)
16	Flocculus (dx)
17	Endolambda
17	Maximum curvature of the sigmoid sinus (dx)
18	Maximum curvature of the sigmoid sinus (sx)

Tab. 2B. Numero e configurazione dei landmarks sul superfici 3D di *endocast.*

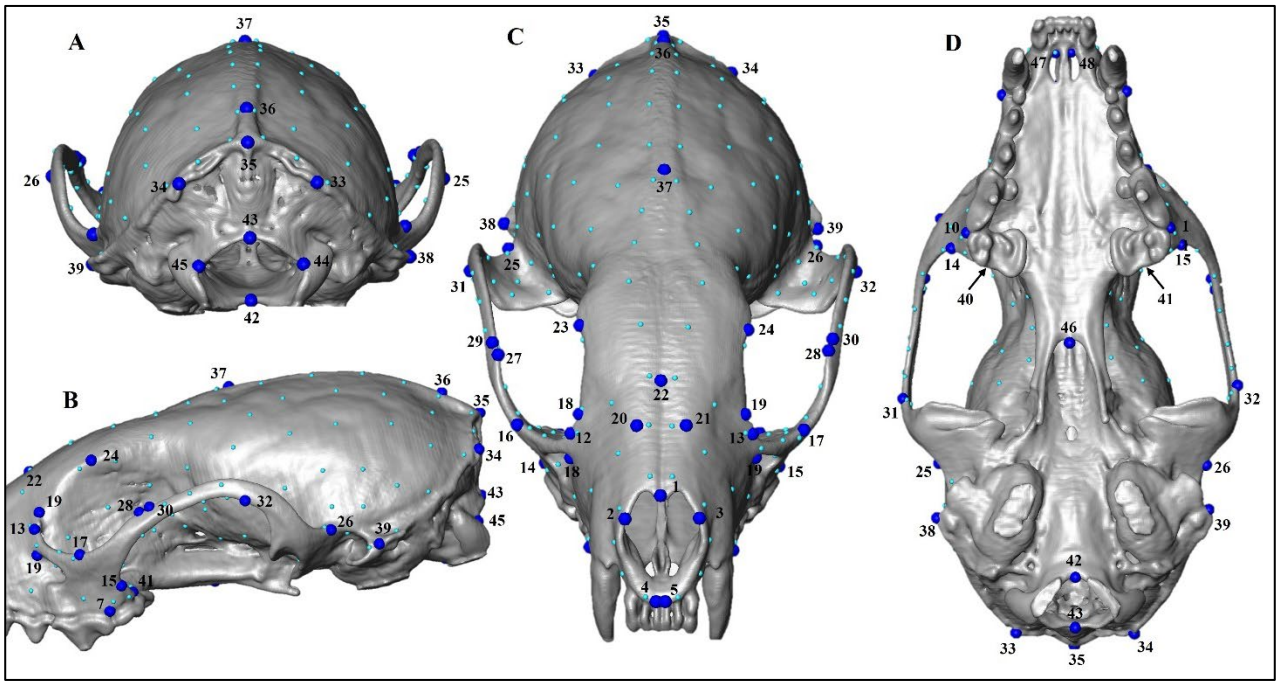

Fig. 2A. Configurazione landmark su cranio di *Martes melampus* (PRICT-253-604).
A: visione posteriore; **B**: visione laterale; **C**: visione frontale; **D**: visione ventrale.

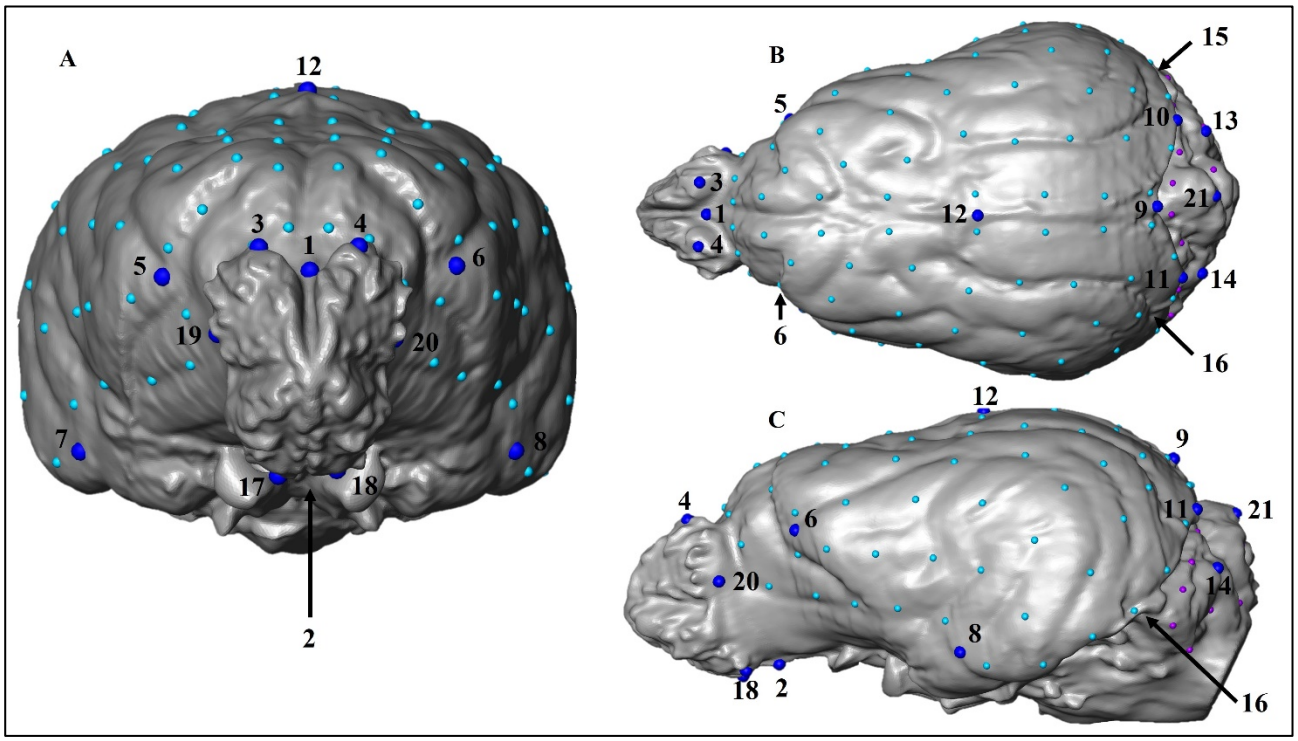

Fig. 2B. Configurazione landmark sull'*endocast* di *Vulpes vulpes* (PRICT-238-424).
A: visione frontale; **B**: visione dorsale; **C**: visione laterale.

Dal momento che le distorsioni hanno inficiato anche sul posizionamento dei landmark, per risolvere questo tipo di problema abbiamo utilizzato nuovamente il pacchetto **Morpho** (Schlager 2017) e soprattutto le funzioni: *symmetrize, fixLMmirror* e *fixLMtps.*

Nell'ordine: *symmetrize* permette di creare una versione perfettamente simmetrica dei landmark; *fixLMmirror* stima invece i landmarks dalle sue controparti bilaterali; *fixLMtps,* infine, stima i landmarks mancanti utilizzando come metodologia di interpolazione la *thin-plate-spline* (Schlager et al., 2019).

Quest'insieme di procedure è servito per preparare i dati per effettuare successivamente le analisi statistiche. La prima parte di analisi riguarda la GMM (*geometric MorphoMetrics*).

Abbiamo effettuato la *Relative warp analysis* (RWA). Quest'analisi costituisce l'equivalente della PCA (analisi delle componenti principali) in studi di morfometria geometrica.

Questo metodo permette di ricavare informazioni sulla forma, o *shape,* di strutture anatomiche dopo aver rimosso tutti gli effetti non legati alla variazione di forma. Tali effetti possono essere relativi a taglia, posizione o orientamento nello spazio di queste strutture e vengono eliminati applicando dapprima la GPA, ovvero la *Generalized Proctrustes Superimposition* (Rohl & Slice 1990).

Ottenuti dati "puliti", si è proceduto col fare la *relative warp analysis.* Questa tecnica applica il tipo di interpolazione *thin-plate-spline (TPS).* Questo scompone la variazione di forma in assi ortogonali di varianza massima e dà come risultato *partial warp scores.* Prendono questo nome perché descrivono solo una parte della deformazione (Zelditch et al. 2004).

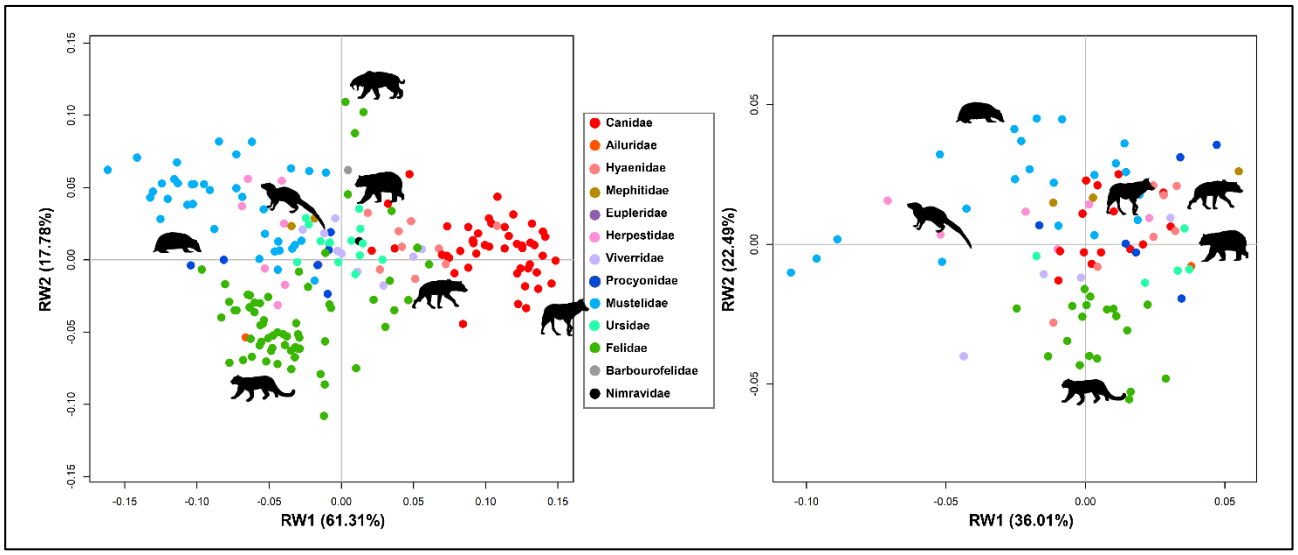

Fig. 3. Risultati ottenuti dalla RWA (*Relative Warp Analysis*) per crani (a sinistra) ed *endocast* (a destra).

Osservando i due grafici in Figura 3 contenenti i risultati della RWA, si possono notare pattern abbastanza distinti, soprattutto nel plot di sinistra. Infatti, dalle analisi condotte sui crani, ciascuna famiglia tende a separarsi dalle altre ed a costituire un gruppo omogeneo. Quindi il segnale filogenetico è abbastanza evidente. Nel grafico di destra invece, si osserva come gli endocast non mostrino lo stesso forte segnale filogenetico.

Successivamente, sono state fatte analisi filogenetiche.

Gli alberi filogenetici sono *informal supertree*, basati sulle topologie e tempi di separazione presentati in Melchionna et al. (2021), Castiglione et al. (2021) e Modafferi et al. (2022) (Fig.4 A,B,C e Fig. 10, 11, 12).

Per testare la presenza di convergenza evolutiva si è utilizzata la funzione *search.conv* (Castiglione et al., 2019) del pacchetto RRphylo (Raia et al., 2018). Questa funzione valuta la convergenza testando se i fenotipi di cladi, distanti filogeneticamente, sono più simili di quanto previsto. Il metodo funziona calcolando l'angolo tra i vettori del fenotipo delle specie, come misura della loro somiglianza e consente l'identificazione della convergenza tra cladi. È un metodo molto veloce e performante ed inoltre, non richiede che i cladi convergenti siano fenotipicamente "insoliti" rispetto al resto dell'albero (Castiglione et al., 2019).

La funzione *search.shift* (Castiglione et al., 2018) permette invece di individuare come cambiano i tassi evolutivi nei diversi cladi e soprattutto a che velocità. Inoltre, la funzione traccia in modo automatico la differenza reale dei tassi, sovrapposti sulla distribuzione della differenza casuale e fornisce i *p-values* per il test di variazione dei tassi (Castiglione et al., 2018).

In seguito, abbiamo applicato la PGLS (*phylogenetic generalized Least Square*). Questa tecnica è una modifica dei minimi quadrati generalizzati, ed utilizza la conoscenza delle relazioni filogenetiche per produrre una stima della covarianza prevista nei dati tra specie diverse. Specie strettamente imparentate hanno tratti più simili a causa dei loro rapporti di parentela e quindi si presume che producano residui più simili dalla linea di regressione dei minimi quadrati (Symonds, M.R.E., Blomberg, S.P., 2014)

1. *Risultati delle analisi sui crani*

Dalla funzione *search.shift* abbiamo ottenuto i dati relativi agli shift evolutivi ed i valori di *p-value* (Tab.3).

Per i nodi 191 e 167 (Fig. 4A- 4B) ci sono valori di *shift* negativi, il che vuol dire che nel caso del clade Feliformia e della famiglia dei Canidi, il tasso di evoluzione è più lento rispetto a quello visibile nel nodo 127 (Fig. 4C), che si riferisce al clade Arctoidea. Questo clade comprende: Ursidi, Mustelidi, Mefitidi e Procionidi.

Nodes	Rate.differences	p.value
191	-0.003740029	0.0028
167	-0.002845669	0.016
127	0.006502671	1

Tab. 3. Dati relativi al nodo dell'albero filogenetico, tasso di evoluzione e *p-value*.

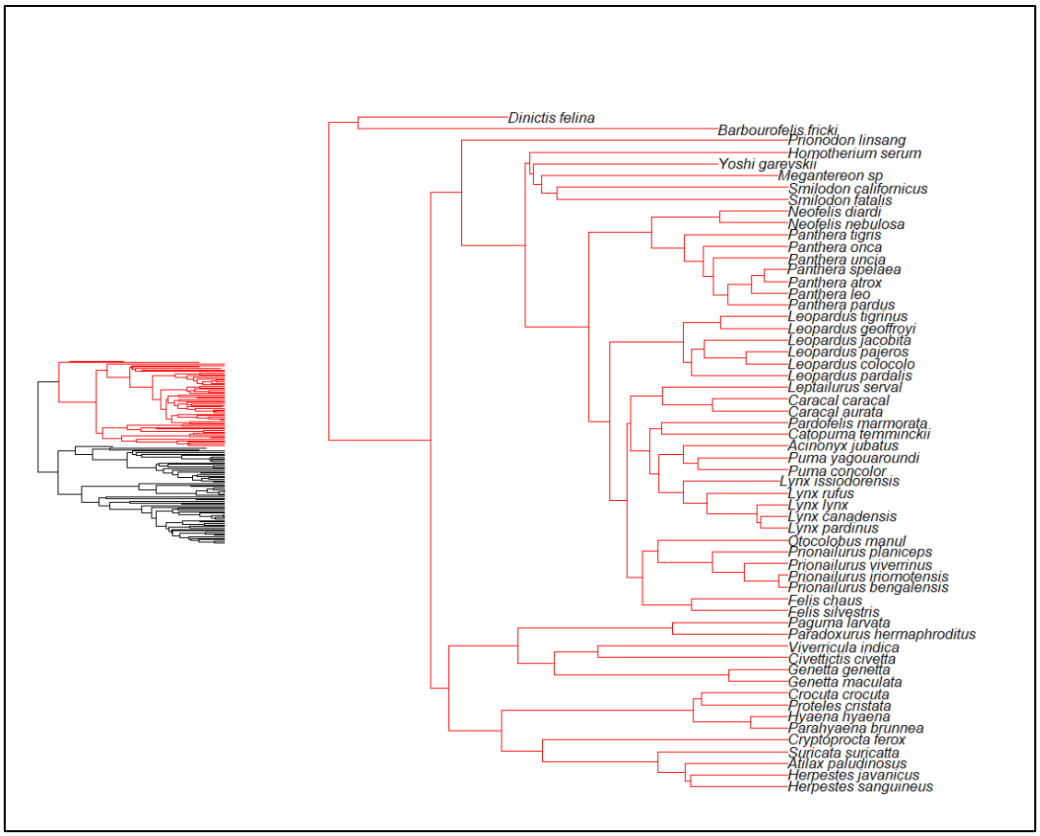

Fig. 4A. Albero filogenetico del clade Feliformia. Nodo 191.

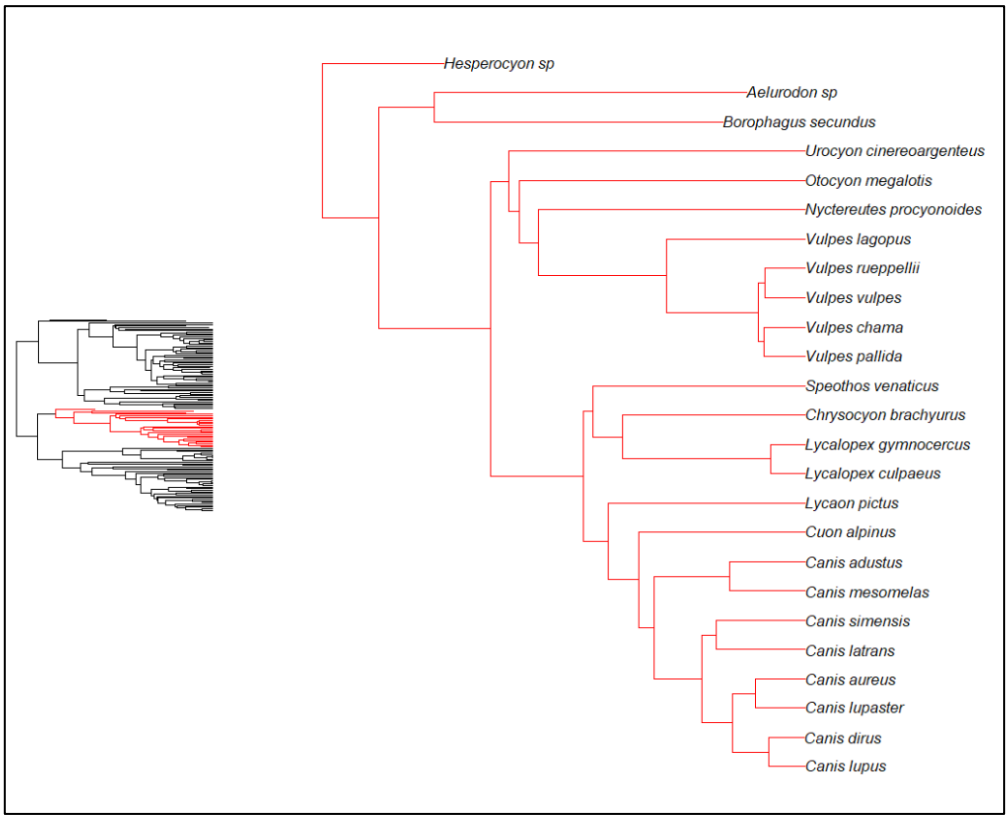

Fig. 4B. Albero filogenetico della famiglia Canidae. Nodo 167.

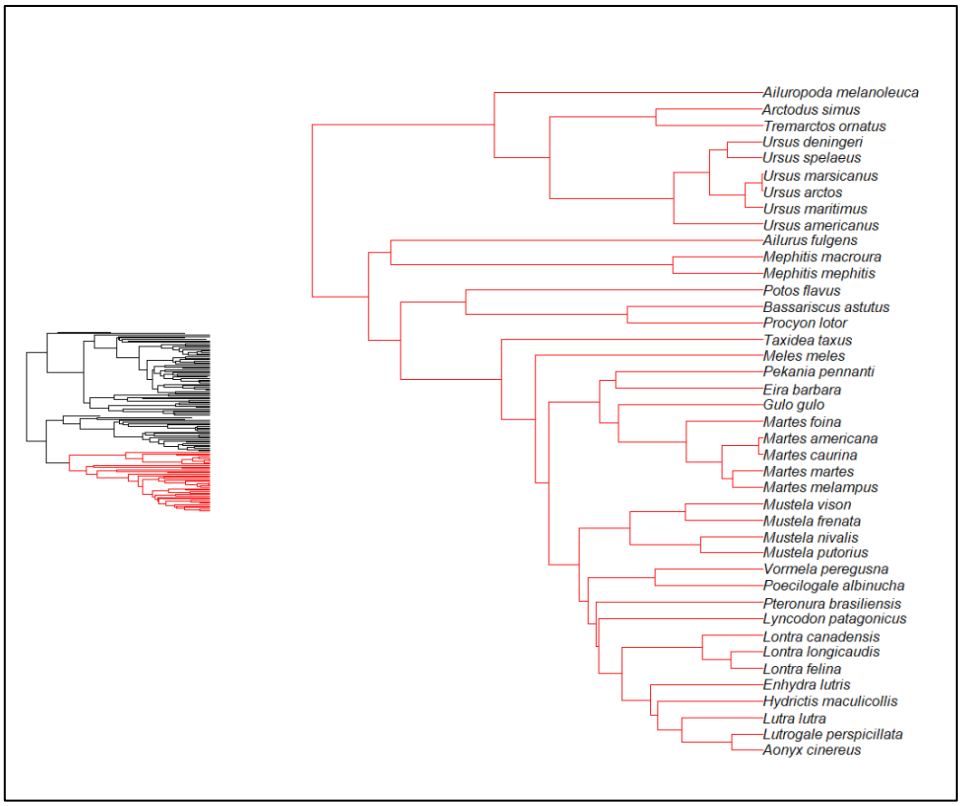

Fig. 4C. Albero filogenetico del clade Arctoidea. Nodo 127.

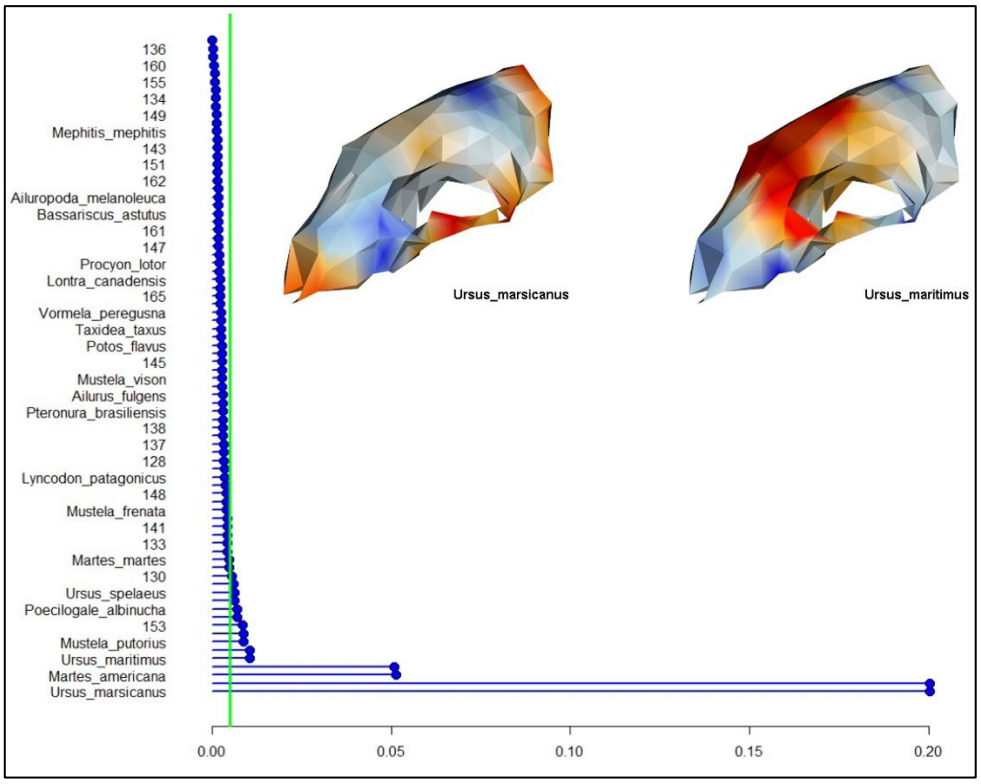

Fig. 5. Diagramma che illustra i tassi evolutivi. Quelli più alti si riscontrano in due specie: *Ursus marsicanus* e *Martes americana.* In alto ci sono invece le superfici di *Ursus marsicanus* ed *Ursus maritimus.* Le aree in rosso indicano contrazione della struttura ossea, mentre quelle in blu indicano invece espansione.

Abbiamo effettuato due analisi PGLS. Una prima (Tab.4A) tenendo conto della taglia come covariata e considerando le varie categorie di dieta: carnivori-onnivori (carn-omn), erbivori (herbivore), ipercarnivori (hyper), insettivori (insectivore), omn-carn (onnivori-carnivori), denti a sciabola (sabretooth) ed animali marini (sea food), comparati con i *bonecracker,* cioè gli spaccaossa.

	Estimate	**p-value**
Intercept	-0.3703536	8.17E-09
xcan-omn	0.0409366	0.0600525
xherbivore	0.0713696	0.0017355
xhyper	0.0207642	0.3735027
xinsectivore	0.0708869	0.0006265
xomn-carn	0.0428951	0.0517661
xsabretooth	0.0238515	0.3816631
xsea food	0.0479418	0.0793579
z	0.0532855	6.25E-10

Tab.4A. Tabella con valori di *estimate* e *p-value*.

Anche nella seconda analisi sono state usate le stesse categorie e sono state comparate con i *bonecracker.* Non è stata però considerata la taglia come covariata (Tab. 4B).

	Estimate	**p-value**
Intercept	-0.00741106	8.06E-01
xcan-omn	0.01171334	0.6382
xherbivore	0.03081687	0.224
xhyper	-0.00043101	0.9873
xinsectivore	0.0365659	0.1138
xomn-carn	0.01402103	0.5787
xsabretooth	0.03103513	0.3331
xsea food	-0.04319463	0.1778

Tab.4B. Tabella con valori di *estimate* e *p-value*.

Dalla funzione *search.conv* abbiamo inoltre ottenuto valori di convergenza nelle specie che hanno una dieta simile, in particolar modo ci soffermiamo su due categorie:

- Sea food (Tab.5, Fig. 6-7);
- Sabretooth (Tab.6;Fig.8-9).

Nella prima categoria i valori del p-value sono significativi, come dimostra anche la Tabella 5.

	Angle.state	p.angle.state.time
sea food	11.20882	0.001

Tab.5. Il valore *p.angle.state.time* risulta essere significativo, mentre *p.angle.state.time* indica la distanza fenotipica. Il suo valore indica che c'è significatività sulla distanza fenotipica rispetto a quella filogenetica.

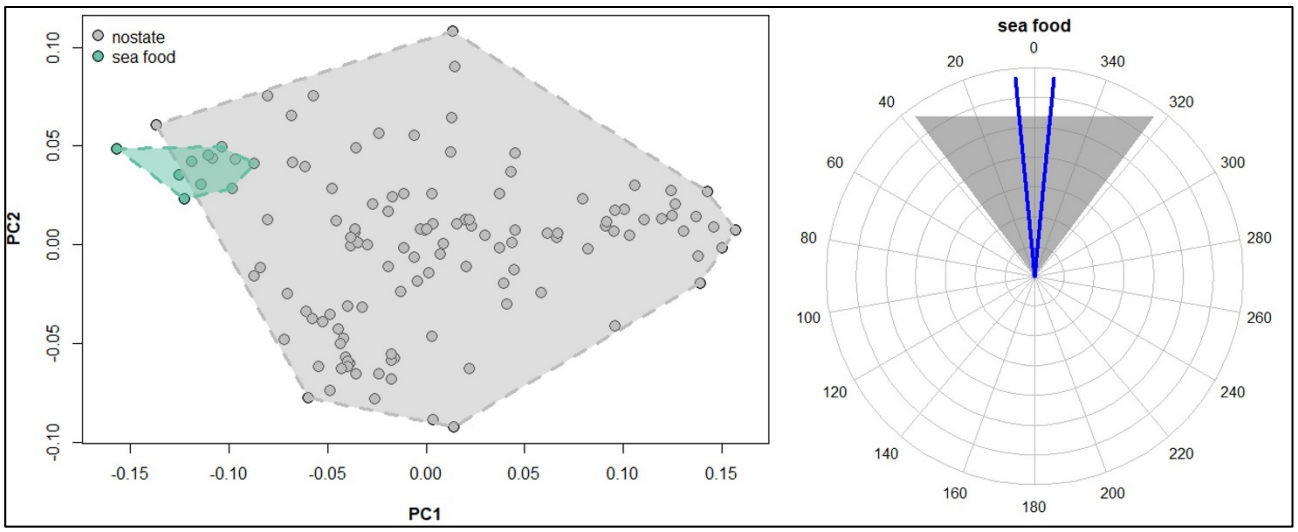

Fig.6. Output grafico della funzione *search.conv.* A sinistra il PC1-PC2 plot in cui, col poligono verde è rappresentato il gruppo che condivide la stessa dieta. A destra invece c'è il *polar plot* in cui la distanza tra i vettori fenotipici (di colore blu) è minore della distanza angolare calcolata, in modo casuale (indicato dal triangolo in grigio). Questo è indice di convergenza.

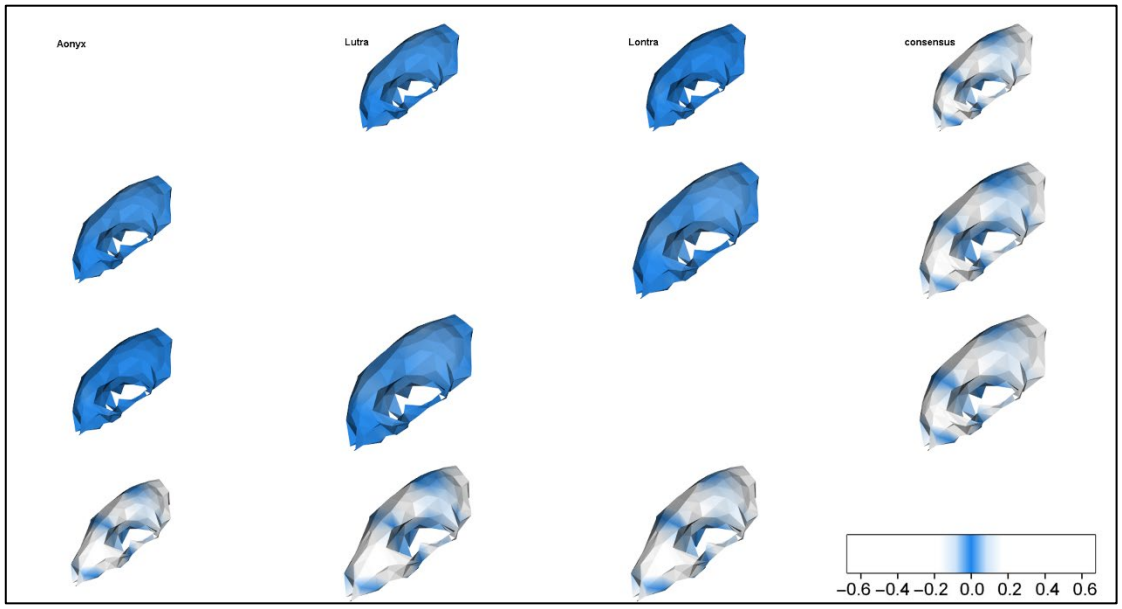

Fig. 7. In questa figura possiamo osservare quali sono le aree convergenti (in blu) rispetto a quelle che non lo sono (in bianco). Sono stati comparati tre generi di mustelidi: *Aonyx sp., Lutra sp.,*

Lontra sp., e chiaramente il consensus (ovvero la forma media). Si nota molto chiaramente quanto i crani siano simili a livello morfologico.

	angle.state	**p.angle.state.time**
sabretooth	31.17659	**0.001**

Tab.6. Il valore *p.angle.state.time* risulta essere significativo, mentre *p.angle.state.time* indica la distanza fenotipica. Il suo valore indica che c'è significatività sulla distanza fenotipica rispetto a quella filogenetica.

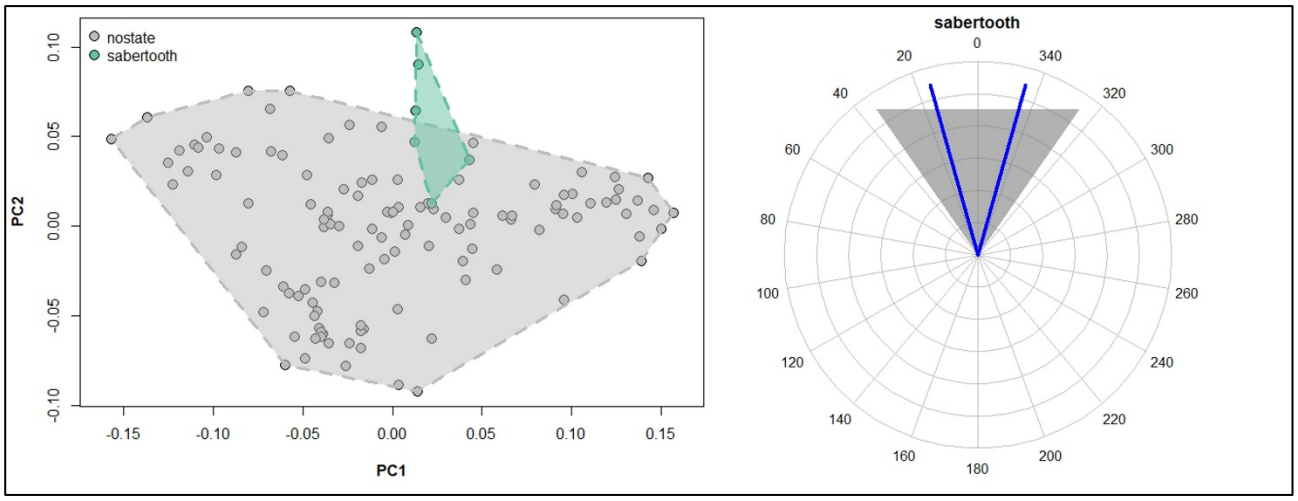

Fig. 8. Output grafico della funzione *search.conv.* A sinistra il PC1-PC2 plot in cui, col poligono verde è rappresentato il gruppo che condivide la stessa dieta. A destra invece c'è il *polar plot* in cui la distanza tra i vettori fenotipici (di colore blu) è minore della distanza angolare calcolata, in modo casuale (indicato dal triangolo in grigio). Questo è indice di convergenza. In questo caso si considera il gruppo *sabretooth.*

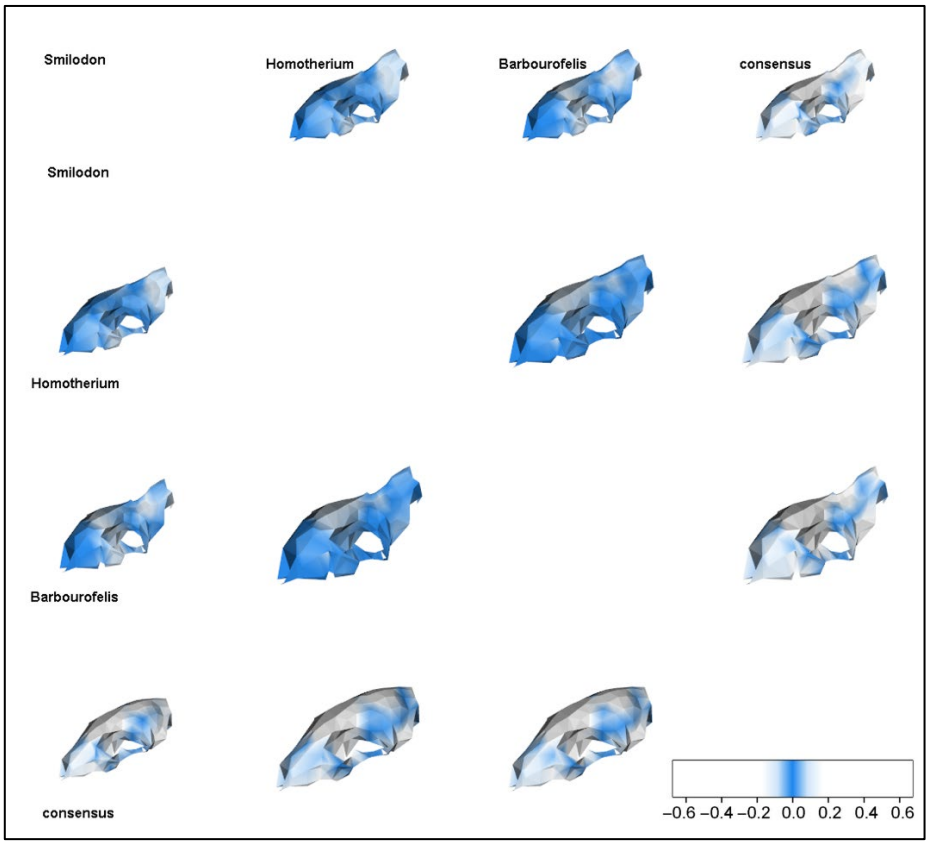

Fig.9. In questa figura possiamo osservare quali sono le aree convergenti (in blu) rispetto a quelle che non lo sono (in bianco). Sono stati comparati tre generi di *sabretooth*: *Smilodon sp., Homotherium sp., Barbourofelis sp.,* e chiaramente il consensus (ovvero la forma media). Si nota molto chiaramente quanto i crani siano simili a livello morfologico, soprattutto nella zona del cranio corrispondente alla cavità nasale ed alla regione alveolare intorno ai canini.

Altri risultati sono stati ottenuti dalla PGLS effettuata sull'ambiente, anziché sulla dieta, considerando (Tab.7A) o meno (Tab.7B) la taglia come covariata.

	Estimate	**p-value**
Intercept	0.204933	6.73E-04
xclosed	0.011908	0.56224
xfossorial	0.011125	0.593214
xopen	0.01797	0.357646
xscansorial	-0.0053	0.806507
z	-0.03217	1.90E-05

Tab. 7A. Tabella con valori di *estimate* e *p-value*

	Estimate	**p-value**
Intercept	-0.01693	6.14E-01
xclosed	0.02758	0.2068

xfossorial	0.028027	0.2047
xopen	0.029988	0.1509
xscansorial	0.011083	6.29E-01

Tab. 7B. Tabella con valori di *estimate* e *p-value.*

2. *Risultati delle analisi sugli endocast*

Per quanto concerne gli *endocast*, dalla funzione *search.shift* abbiamo ottenuto i seguenti risultati:

	rate.difference	**p.value**
92	-0,001123464	0,0005
110	-0,000842871	0,0087
64	0,001277856	1

Tab.8. Dati relativi al nodo dell'albero filogenetico, tasso di evoluzione e *p-value*.

Nella Tab.8 ci sono i risultati relativi all'applicazione della funzione *search.shift* del pacchetto **RRphylo.** Degni di nota sono i risultati della seconda colonna, in cui si possono osservare tassi positivi e negativi. I primi implicano un tasso evolutivo più rapido mentre i secondi viceversa. La prima colonna indica invece a quali codi dell'albero filogenetico corrispondono questi valori: nodo 92, 110 e 64. Rispettivamente: Canidae, il clade Feliformia ed il clade Arctoidea (Fig. 10,11,12).

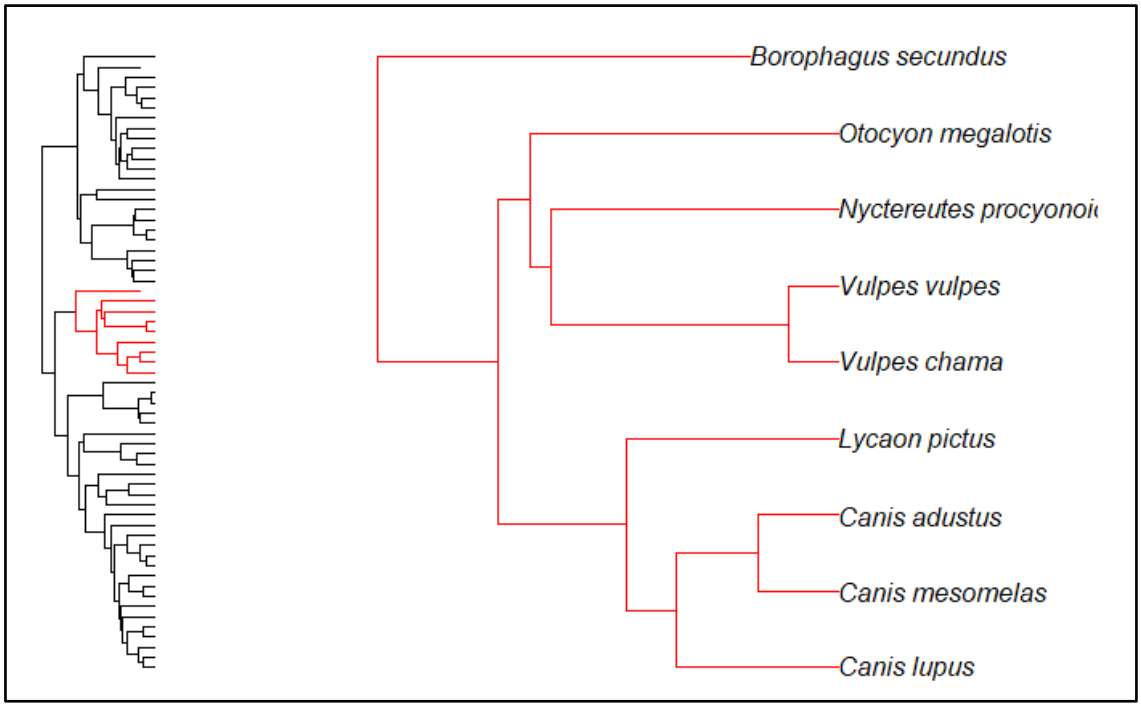

Fig. 10. Albero filogenetico della famiglia Canidae. Nodo 92.

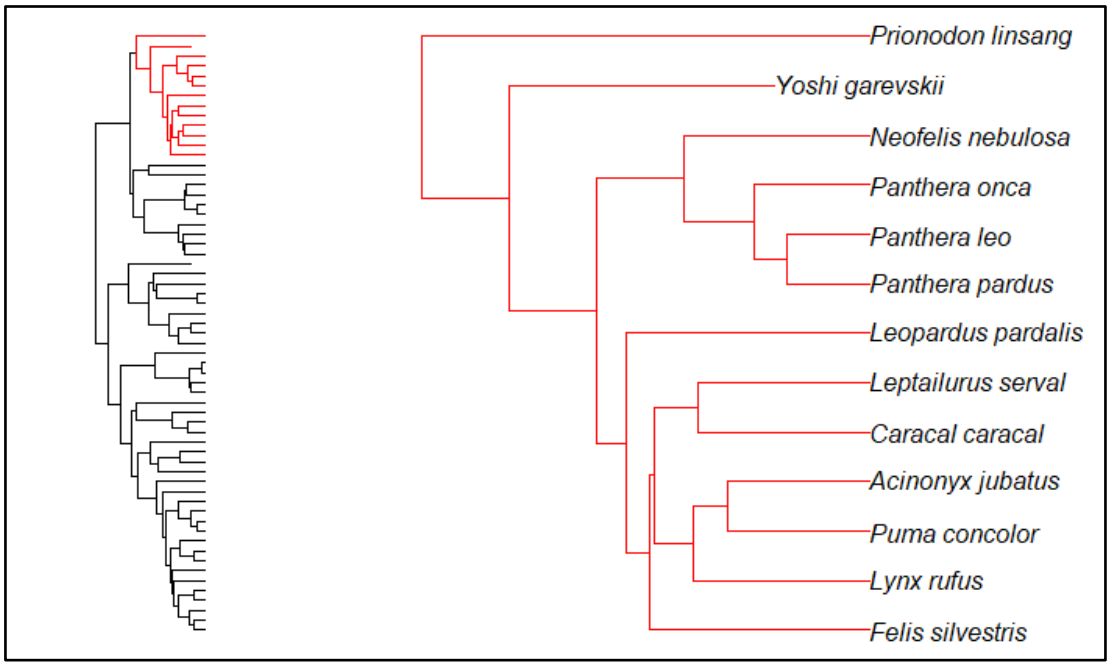

Fig. 11. Albero filogenetico del clade Feliformia. Nodo 110.

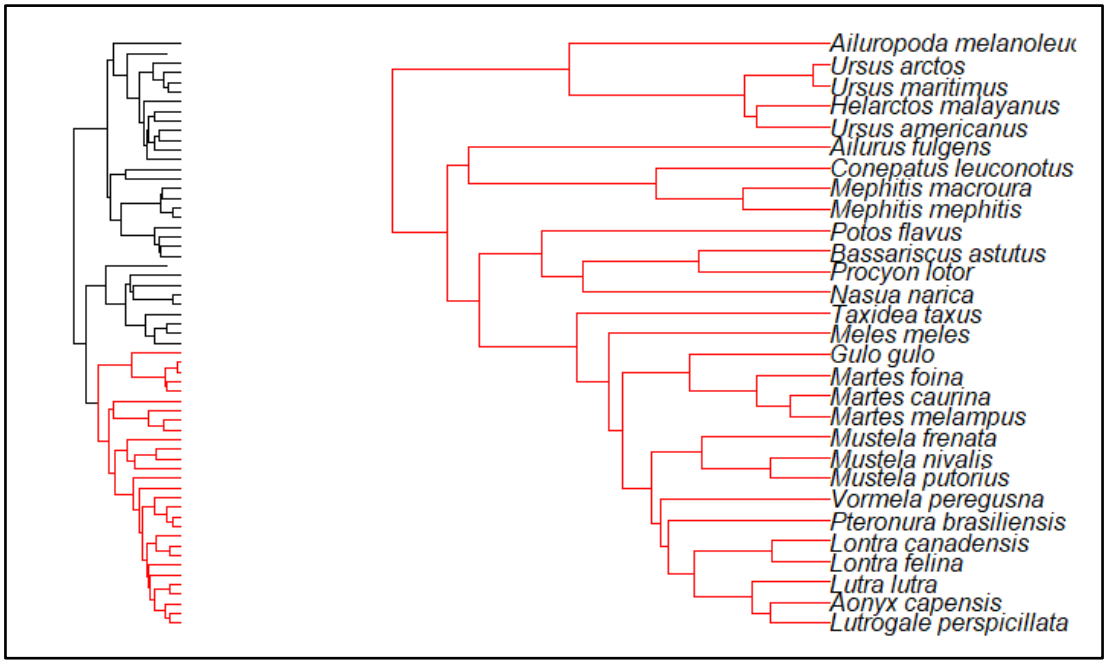

Fig. 12. Albero filogenetico del clade Arctoidea. Nodo 64.

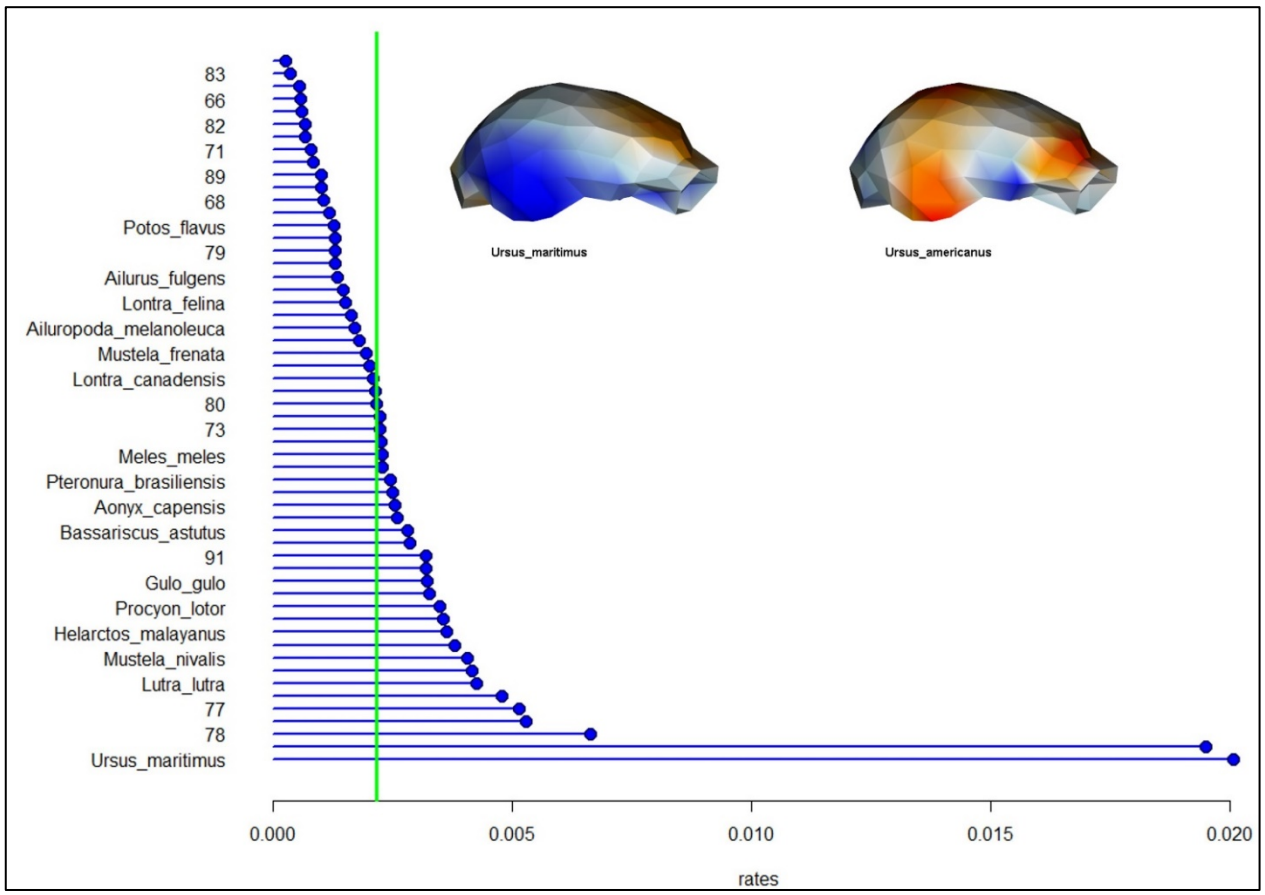

Fig. 13. Diagramma che illustra i tassi evolutivi per gli *endocast*. Quelli più alti si riscontrano in due specie: *Ursus maritimus.* In alto ci sono invece le superfici di *Ursus maritimus* ed *Ursus marsicanus.* Le aree in rosso indicano contrazione della struttura ossea, mentre quelle in blu indicano invece espansione. Nel caso di *Ursus maritimus* c'è una significativa espansione nell'area del lobo temporale, mentre in *Ursus americanus* c'è una significativa contrazione.

Di seguito, le quattro tabelle con i risultati dell'analisi PGLS anche per gli *endocast*. La prima e la seconda (Tab.9A- 9B) tengono e no, rispettivamente, conto della taglia come covariata e considerano le varie categorie di dieta: carnivori-onnivori (carn-omn), erbivori (herbivore), ipercarnivori (hyper), insettivori (insectivore), omn-carn (onnivori-carnivori), denti a sciabola (sabretooth) ed animali marini (sea food).

	Estimate	**p-value**
Intercept	-0,1854605	0,018873
xcarn-omn	-0,0485034	0,014535
xherbivore	-0,0166578	0,559269
xhyper	-0,0340532	0,125662
xinsectivore	0,0005197	0,975937
xomn-carn	-0,3011456	0,550089
xsea food	-0,0354687	0,148713
z	0,0376441	0,003493

Tab.9A. Tabella con valori di *estimate* e *p-value*.

	Estimate	**p-value**
Intercept	0,039349	0,092029
xcarn-omn	-0,064104	0,002148
xherbivore	-0,021213	0,488557
xhyper	-0,034476	0,148382
xinsectivore	-0,018884	0,274869
xomn-carn	-0,027711	0,164266
xsea food	-0,025039	0,335164

Tab.9B. Tabella con valori di *estimate* e *p-value*.

Le tabelle 10A e 10B invece, sono state fatte sull'ambiente. Anche qui, nella prima tabella si considera la taglia come covariata, mentre nella seconda no.

	Estimate	**p-value**
Intercept	-0,2932062	0,0005239
xclosed	0,026086	0,1382338
xfossorial	-0,0016554	0,9151286
xopen	-0,0071103	0,6556805
xscansorial	0,0078003	0,6676945

z	0,0516488	9,16E-05

Tab.10A. Tabella con valori di *estimate* e *p-value*.

	Estimate	**p-value**
Intercept	0,03074	0,20547
xclosed	-0,008683	0,61978
xfossorial	-0,27731	0,09176
xopen	-0,034352	0,04218
xscansorial	-0,025887	0,16702

Tab.10B. Tabella con valori di *estimate* e *p-value*.

Infine, questi sono i risultati relativi alla funzione *search.conv.*

	angle.state	**p.angle.state.time**
scansorial	93,11143	0,947

Tab.11. Il valore *p.angle.state.time* risulta essere significativo, mentre *p.angle.state.time* indica la distanza fenotipica. Il suo valore indica che c'è significatività sulla distanza fenotipica rispetto a quella filogenetica.

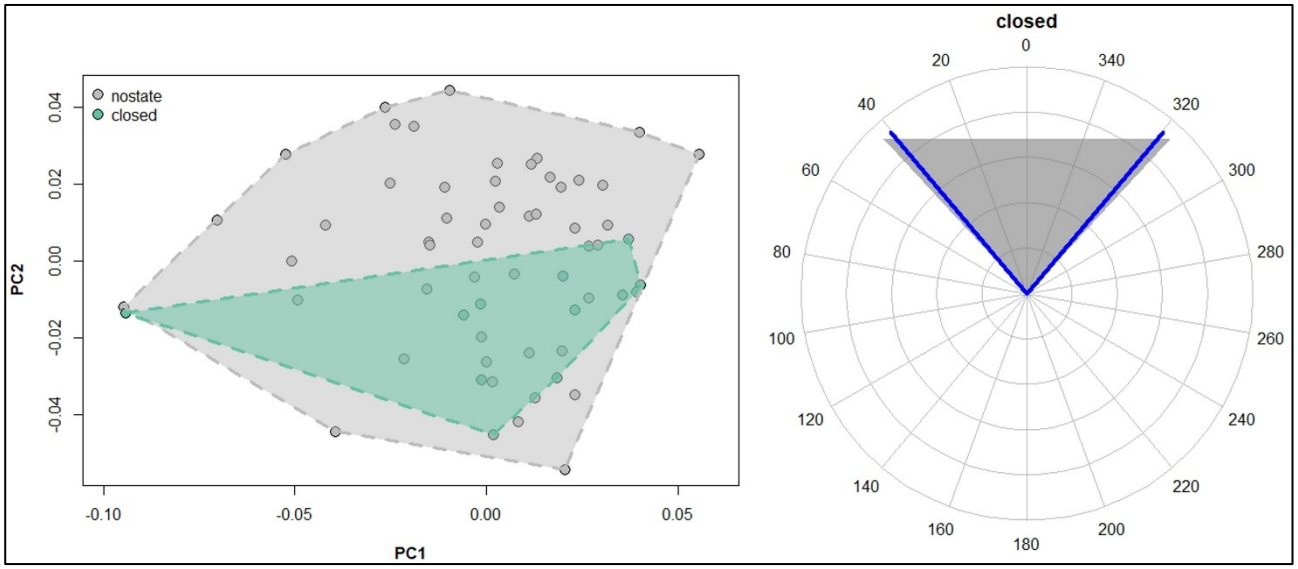

Fig.14. Output grafico della funzione *search.conv.* A sinistra il PC1-PC2 plot in cui, col poligono verde, è rappresentato il gruppo che condivide la stessa dieta. A destra invece, c'è il *polar plot* in cui la distanza tra i vettori fenotipici (di colore blu) è minore della distanza angolare calcolata, in modo casuale (indicato dal triangolo in grigio). Questo è indice di convergenza. In questo caso si considera come tipo di ambiente quello chiuso.

One among many: the enigmatic case of the Miocene mammal, *Kolponomos newportensis*

MARIA MODAFFERI[1], , MARINA MELCHIONNA[1*], SILVIA CASTIGLIONE[1], DAVIDE TAMAGNINI[2], LUIGI MAIORANO[2], GABRIELE SANSALONE[3], ANTONIO PROFICO[4,5], GIORGIA GIRARDI[1] and PASQUALE RAIA[1]

1*Dipartimento di Scienze della Terra, dell'Ambiente e delle Risorse, Università di Napoli Federico II, 80126 Napoli, Italy*
2*Department of Biology & Biotechnologies 'Charles Darwin', University of Rome 'La Sapienza', viale dell'Università 32, 00185 Rome, Italy*
3*Function, Evolution & Anatomy Research Laboratory, Zoology Division, School of Environmental and Rural Science, University of New England, Armidale, NSW, 2351, Australia*
4*Catalan Institute of Human Paleoecology and Social Evolution (IPHES), Zona Educacional 4, 43007 Tarragona 43002, Spain*
5*Àrea de Prehistòria, Facultat de Lletres, Universitat Rovira i Virgili, Tarragona 43002, Spain*

Biological Journal of the Linnean Society, Volume 136, Issue 3, July 2022, Pages 477–487

https://doi.org/10.1093/biolinnean/blac052

Abstract

Kolponomos newportensis era un enigmatico mammifero vissuto nel Miocene. È stato descritto per la prima volta nel 1960 da Stirton, grazie a resti frammentari ritrovati nei depositi marini di Clallam Bay sul margine nord-occidentale del Pacifico. Questa specie fu perciò chiamata *Kolponomos clallamensis.*

Anni dopo, nella Nye Mudstone Formation (Oregon) furono scoperti resti cranici e post- cranici, tanto da fondare una nuova specie: *Kolponomos newportensis.*

La posizione tassonomica di questo animale è sempre stata ambigua ed oggetto di studi. Precedentemente si pensava che fosse filogeneticamente vicina agli Amficionidi (Tedford et al., 1994), ma attualmente viene inserito come *stem-group* dei Pinnipedimorpha.

Questo studio riguarda la presenza di convergenza evolutiva tra questo particolare mammifero e diverse specie di *sabretooth*: *Barbourofelis fricki, Homotherium serum, Hoplophoneus primaevus, Smilodon fatalis* e *Smilodon californicus.* L'obbiettivo è stato quello di verificare l'ipotesi secondo cui le tecniche di caccia di queste specie così filogeneticamente lontane presentassero in realtà palesi elementi di convergenza.

Main text

Convergence concerns the independent appearance of similar phenotypes in distantly relates lineages (Harmon et al., 2005; Losos, 2011). Among mammal, there are a lot of examples such as elongates upper canines in different predatory species (Wroe et al, 2008; Melchionna et al., 2021), locomotion in sloths (Serio et al., 2020) and Euarchontoglires (Geng et al., 2020), high-crowned molars in grazers (Palmqvist et al., 2008; Gomes Rodrigues et al., 2017) and fused metatarsals in artiodactyls (Yohe & Solounias, 2020).

Sometimes happens that different phenotypes produce similar functional outputs, known as many-to-one mapping of form to function (Alfaro et al., 2005; Wainwright, 2007; Losos, 2011; Renaud et al., 2018). It means that functional convergence might occur even if there isn't morphological convergence (Sansalone et al., 2020).

In extinct species, the correct recognition of functional convergence is complicated by the limited availability and bad fossil record condition. So, palaeontology infer functional performance by means of different approaches, like indirect measurements and simulations.

Tseng et al. (2016) recently described the feeding style of the extinct pinniped *Kolponomos,* reporting an unusual case of mosaic convergence between it and the sabretooth *Smilodon.*

The attribution of *Kolponomos* to any specific family of Carnivora remained elusive. After the discovery of a partially complete cranium, a mandible and a few post-cranial bones, new species *Kolponomos newportensis* was erected. At that time, *Kolponomos* was phylogenetically linked to Amphicyonidae (Tedford et al., 1994).

Later, this species was revisited again and was allied to stem Pinnipedimorpha (Paterson et al., 2020). With a probably amphibious lifestyle, *Kolponomos* fed on hard-shelled marine invertebrates that lived on rocky substrates. About *Kolponomos* feeding strategy, Tseng et al., 2016 suggested that this animal used the anterior portion of its jaw as a fulcrum to capture and dislodge shells from the substrates, while the cheek teeth served to crush the prey exoskeletons.

Applying FEA (Finite Element Analysis) and GMM (Geometric MorphoMetrics) to mandibles of seven different mammal species, Tseng et al., found that there is a functional convergence between *Kolponomos* and *Smilodon* about the prey-capture strategy. This surprising convergence between these two genera was explained in term of the way they used their mandibles.

Both possessed a prominent mastoid process, suggesting massive atlanto-mastoid muscles to facilitate the head-flexing movement originating the torque (Antón et al., 2004; Tseng et al., 2016).

This suggested that convergence can be identified in cranium structure as well.

In this paper, we address the role of cranial shape in morphological convergence between *Kolponomos* and these sabretooth species: *Barbourofelis frickii, Homotherium serum, Hoplophoneus primaevus, Smilodon fatalis* and *Smilodon californicus.*

Our hypothesis is that morphological similarity between sabretooth and *Kolponomos* should be limited at the presence of long and flattened upper canines and the complex feeding habits of *Kolponomos.*

By mapping convergence on 3D cranium models, now possible thanks to a recent method *conv.map* (Melchionna et al., 2021), we expect to find convergence in the posterior area of the skull, which provides to the attachment for powerful masticatory and neck muscles that both *Kolponomos* and sabretooth had, and its front, where applied contact with the prey.

Methods

Data collection and preparation

We collected 159 3D skull models belonging to different taxonomic groups: Barbourofelidae, Canidae, Felidae, Herpestidae, Hyaenidae, *Kolponomos newportensis,* Mephitidae, Mustelidae, Nimravidae, Odobenidae, Otariidae, Phocidae, Prionodontidae, Ursidae, Viverridae. Out dataset included 98 species, both extinct and living. Three-dimensional CT-scan and/or surface belong to different online databases: Digimorph, KUPRI, Morphosource, Phenome10K and Sketchfab, or were acquired from museum by one of us (DT).

Y. garevskii and *D. barlowi* were kindly provided by N. Spassov and D. Gerrads (Spassov & Geraads, 2015) and Justin Adams and colleagues (Adams et al., 2015), respectively.

To extract surface from CT-Scan, we used Amira (v.5.4.5, Visualization Sciences Group, 2013) and Geomagic Studio (v.2014.3.0.1781, Geomagic, 2014).

We placed a set of 37 landmarks by using Amira on each specimen, to record variation in cranial shape (**Fig.1, Table 1**).

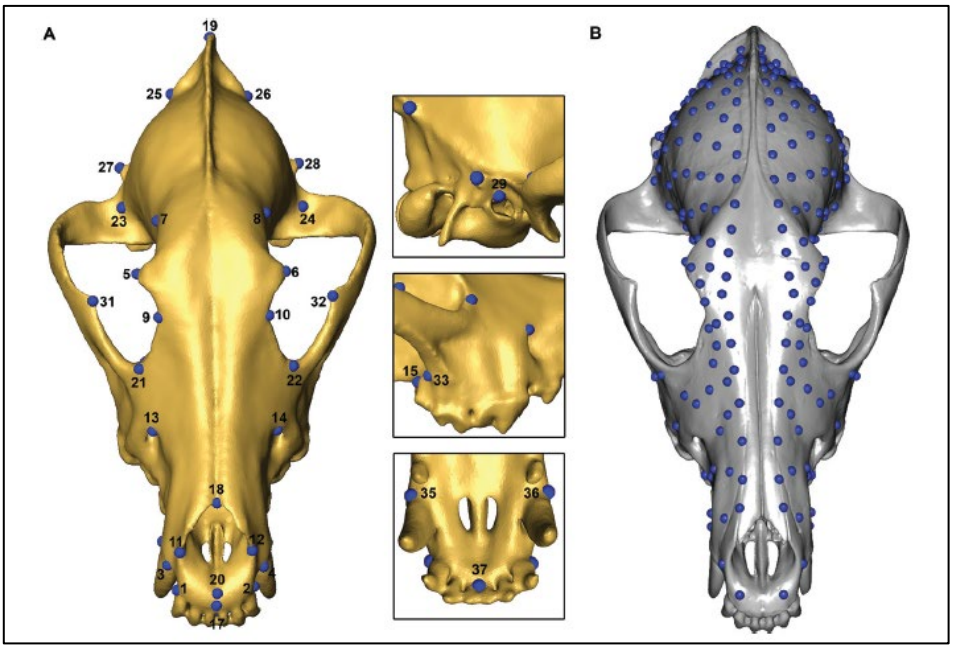

Fig.1. Landmark and semilandmark configuration. A- manually sampled landmark. B- semilandmark patches placed through the *sliding* procedure (see **Table 1** for a full landmark description).

Number	Landmark Definition
1 and 2	Alveolar margin at the posterior aspect of the last incisor (right and left side)
3 and 4	Alveolar margin at the anterior aspect of the canine (right and left side)
5 and 6	Frontal zygomatic process (right and left side)
7 and 8	Postorbital constriction (right and left side)
9 and 10	End of supraorbital margin (right and left side)
11 and 12	Margin of the nasal aperture (right and left side)
13 and 14	Infraorbital foramen (right and left side)
15 and 16	Alveolar margin at the posterior aspect of the last molar (right and left side)
17	Anterior edge of the premaxilla
18	Anterior point of midline between nasals
19	Topmost point of the nuchal crest
20	Interpremaxillary suture at the inferior margin of the nasal aperture
21 and 22	Anterior edge of the premaxilla-jugal suture
23 and 24	Root of the zygomatic arch (right and left side)
25 and 26	Lambdoid crest (right and left side)
27 and 28	Dorsalmost point of the mastoid process (right and left side)
29 and 30	"Dorsalmost point of the acoustic meatus (right and left side)" (“One among many: the enigmatic case of the Miocene mammal,”) (“One among many: the enigmatic case of the Miocene mammal,”)
31 and 32	Dorsalmost point of the frontal process of the zygomatic bone (right and left side)
33 and 34	Ventral intersection between the zygomatic arch and the maxilla
35 and 36	Alveolar margin at the posterior aspect of the canine (right and left side)
37	Juncture between incisor (internal side)

Table 1. Landmark description.

Kolponomos newportensis skull holotype (USNM215070) was taken from Tseng et al. (2016). Some fossil specimens presented missing parts and distortion in cranial shape due to taphonomic processes. To account these problems, we retrodeformed some digital models and *Kolponomos* model using *retroDeformMesh* function, an algorithm embedded in the R package **Morpho** (Schlager et al., 2018). Aim of this function is to symmetrize 3D surface using landmark. To perform retrodeformation, we placed bilateral landmark on the best- preserved and most recognizable parts of skull morphology.

Retrodeformed models was processed in Geomagic Studio. Eventually, 3D model was smoothed and symmetrized by taking the best-preserved side (right) of the specimen as reference (**Fig.2**).

These fossil species: *Dinofelis barlowi* (DNMNH-BF55-22), *Hoplophoneus primaevus* (USNM-99), *Smilodon californicus* (BCGD-27000), *Yoshii garevskii* (MMNH-Sk-69) presented taphonomic distortion and was partially incomplete. So, we estimated the position of missing landmarks using *fixLMtps* and *fixLMmirror* both from R package **Morpho** (Schlager, 2017).

The former estimates missing landmarks combining nearest-neighbour interpolation and TPS (*thin plate spline*) deformation, while the latter estimates missing landmark from their bilateral counterparts (Schlager, 2017).

fixLMtps was applied in cases of damaged surfaces, *fixLMmirror* to missing portions of the skull for which the counterpart was present and undeformed.

For mapping convergence pattern on digital model (Melchionna et al., 2021), we placed 100 semilandmarks, evenly spaced, on the left side of a reference samples and we mirrored semilandmarks on the right side. Then, we performed sliding procedure on each specimen following the protocol included in **Morpho** package (Schlager, 2017).

These specimens: *Aonyx capensis* CMNH-VZ-17620*, Zalophus californianianus* LEPBLBZ-BM-361-080300 and LEPBLBZ-CSL-484-230404*,* were excluded because they present missing part which prevent semilandmarks placing.

Using the complete set of landmarks and semilandmarks, we performed GPA (*general Procrustes analysis*) to align, rotate and scale landmark configuration. Then, we performed PCA (principal component analysis) on the aligned configuration using R package **Morpho.**

To perform convergence analysis, we assembled a phylogenetic tree (Fig.3) following the hypotheses proposed by Paterson et al., (2020) with *Kolponomos newportensis* as stem-pinnipeds.

Phylogenetic tree was assembled by using a new tool, *tree.merger* (Castiglione et al., 2022)*,* included in R package **RRphylo** (Castiglione et al., 2018).

Morphological convergence test

To test morphological convergence between sabretooth and *Kolponomos newportensis*, we used a function included in **RRphylo** package (Castiglione et al., 2019) named *search.conv*.

This function computes the angle θ between PC scores vectors for each pair of species as a measure of similarity. Angle θ is further divided by the patristic distance between the pair to provide a second measure of similarity accounting for the evolutionary time separating species.

Both metrics are compared to a family of 100 random values for the same metrics generated under the Brownian motion mode of evolution to assess significance (Castiglione et al., 2019).

Search.conv tool can test two different kinds of convergence: (i) convergence among distinct monophyletic clades on the tree, (ii) convergence among species that sharing a "state" (locomotory type, feeding habit).

In this work, we focused on the second one, erecting a "convergent" state and collating *S. fatalis, S. californicus, Hoplophoneus primaevus, Homotherium serum* and *Kolponomos newportensis* under such a heading. As some sabretooth are close phylogenetically (*Smilodon, Homotherium*), trait similarity among them might be influenced by proximity rather than true convergence. To deal this, *search.conv* test for phylogenetic clustering. Then removes tip species until clustering disappears. Declustering procedure is random, so the result may change depending on which species is omitted. For this reason, we repeated *search.conv* ten times to test the reliability of result.

Tseng et al. (2016) indicates that *Kolponomos* is functionally rather than morphologically convergent on *Smilodon.* PCA plots indicate *Kolponomos* stands well within the morphological variability of pinnipeds. Also, we applied *search.conv* to a restricted number of pinniped species, selecting all of them which were morphologically close to sabretooth than *Kolponomos* as estimated by the θ between vectors of PC scores between each pinniped and the vector of mean PC scores calculated over all sabretooth species. This procedure allows us to test if morphological similarity between *Kolponomos* and *Smilodon* is remarkable compared to other pinnipeds.

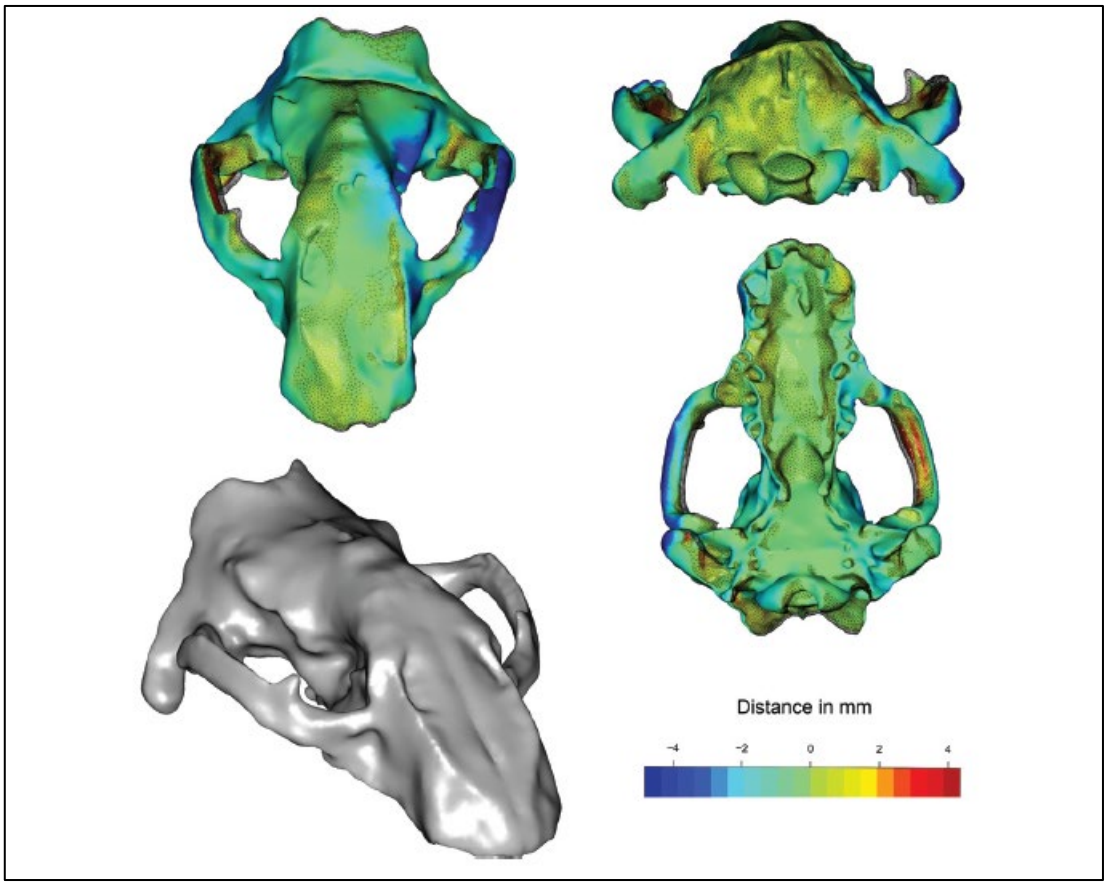

Fig.2. *Kolponomos newportensis* holotype (USNM-215070) and its restoration. The coloured surfaces represent retrodeformation result, while the reticulates surfaces represent the superimposed original shape of the 3D model. The most deformed areas were highlighted following the colour scale shown. Surface on the bottom left is the 3D mesh after restoration with Geomagic Studio.

Relative warp analysis and conv.map

We use *conv.map* to explore the patterns of morphological convergence. *Conv.map* is a novel method which chart the PC axes responsible for the greatest similarity mong species directly on the 3D models (Melchionna et al., 2021). To apply this method, we use RWA (relative warp analysis) to single-out the non-affine component of shape variations by means of partial warp scores (Rohlf & Bookstein, 2003). We performed relative warp analysis on both landmarks and semilandmarks configurations by using *relWarp* functions of the R package **Morpho** (Schlager, 2017).

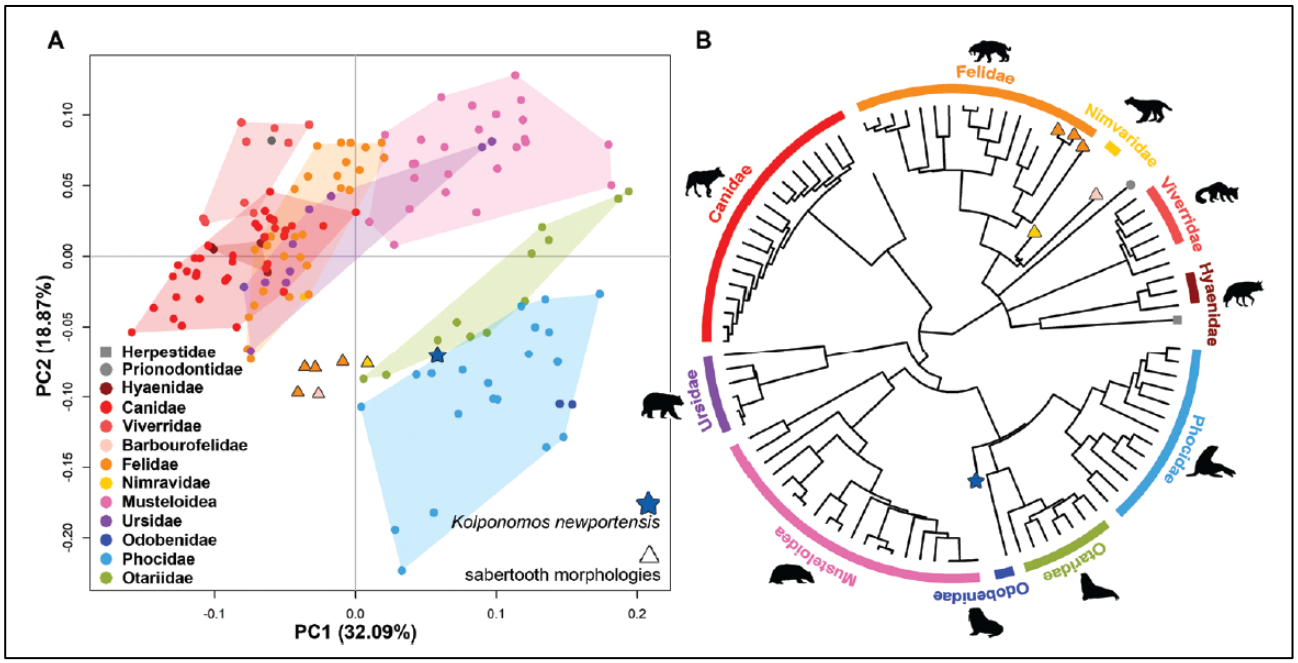

Fig.3. Morphospace defined by the two first PC axes and the phylogenetic tree. A- PC1 and PC2 axes; B- phylogenetic tree. The star represents the phylogenetic position of *Kolponomos newportensis*. Triangles represent the species with a sabretooth morphology: *Hoplophoneus primaevus* (Nimravidae), *Barbourofelis frickii* (Barbourofelidae, pink triangle), *Smilodon californicus, Smilodon fatalis and Homotherum serum* (Felidae). Grey square represents *Suricata suricatta* and grey circle represents *Prionodon linsang*.

Results

Using the full landmark and semilandmarks configuration, the first PCS vectors account for 32,9% and 18,87% of the total shape variation, respectively (Fig. 3A). Along PC1 there is a separation between Canidae, Felidae (at negative values) and Musteoloidea (positive values).

The family Hyaenidae overlap with Canidae on PC1/PC2 plot. Ursidae are close to Mustelidae and Felidae, while species *Helarctos malayanus* is separates from other bears due to its unusual cranial shape.

Over PC2 families Otariidae, Phocidae and Odobenidae are well distinguished from any other species. *Barbourofelis frickii* and *Hoplophoneus primaevus* are close to each other and separated from other pinnipeds and feliforms along PC2. PCA plot of the landmark configuration replicated the same general positioning of major groups in PC1/PC2 biplot.

Kolponomos is close to true sabretooth, but it shared same position with other pinniped species.

The θ angle between the vector of sabretooth average PC scores and the PC scores vector of eleven different pinnipeds to be lower than the corresponding angle between *Kolponomos newportensis* and the sabretooth (Tables 2, S2).

We tested convergence between all of the 12 selected pinniped and true sabretooth, applying *search.conv* ten times separately to each of them. Our result shows the highest frequency of positive evidence for morphological convergence relative to *Kolponomos newportensis* and *Cystophora cristata* (the hooded seal) which were found to convergence on sabretooth half of the time.

Neophoca cinerea (Australian sea lion)*, Eumetopias jubatus* (Steller sea lion) and *Pusa hispida* (ringed seal) were found to converge on sabretooth four out of ten times (Table 3).

The corresponding figures by using landmarks are: *Eumetopias* (six times) and *Neophoca* (four times). *Cystophora* and *Pusa* were not selected for the landmark-only convergence test as they are not morphologically closer to sabretooth than *Kolponomos* by using the landmark configuration.

We selected hoodes seal, sea lion, ringed seal and *Kolponomos* (Fig. 4) to visually inspect which parts of the skull show the highest convergence with *Smilodon.*

Convergence between *Kolponomos* and *Smilodon* involves both face and neurocranium of the skull, and in particular the dorsal surface of the posterior area of the cranium, and the alveolar region around the canines. More, they share a narrow postorbital constriction.

By selecting PC axes responsible for convergence, the *conv.map* function indicates that *Kolponomos* shows a higher degree of convergence with *Smilodon* than to the other pinnipeds, and no one of the latter shows any particularly intense pattern of convergence with sabretooth. In fact, some convergence for these pinnipeds, *Neophoca* and *Cystophora,* is concentrated in nasal region which is absent in *Kolponomos* (Fig.4).

	S. fatalis	*S. californicus*	*B. fricki*	*Homotherium serum*	*Hoplophoneus primaevus*	*Mean*
Halichoerus grypus	73.36	71.13	33.24	76.18	75.88	65.96
Mirounga angustirostris	77.23	78.9	98.35	62.03	59.55	75.21
Phoca vitulina	93.91	96.77	88.43	88.44	34.64	80.44

Neophoca cinerea	79.48	81.08	106.02	27.43	121.74	83.15
Pusa hispida	101.15	104.02	102.06	77.54	39.53	84.86
Monachus tropicalis	96.8	97.35	50.85	70.98	111.81	85.56
Phocarctos hookeri	90.67	89.76	40.17	103.12	106.26	86
Hydrurga leptonyx	89.03	91.95	83.88	63.7	106.12	86.94
Cystophora cristata	79.66	81.76	113.33	84.61	75.42	86.95
Eumetopias jubatus	102.5	104.42	41.2	106.02	89.5	88.73
Monachus monachus	95.5	96.59	84.61	60.02	109.94	89.33
Kolponomos newportensis	79.45	76.49	66.8	120.75	111.64	91.03

Table 2. θ angles among the pinnipeds closest to sabretooth.

	Angle state	**Percentage of issues of convergence found**
Halichoerus grypus	56.45	20
Neophoca cinerea	57.24	40
Mirounga angustirostris	58.42	30
Kolponomos newportensis	58.7	50
Cystophora cristata	60.71	50
Phocarctos hookeri	63.09	30
Hydrurga leptonyx	64.35	30
Monachus monachus	65.76	30
Phoca vitulina	68.32	0
Eumetopias jubatus	69.49	40
Monachus tropicalis	69.75	10
Pusa hispida	70.77	40

Table 3. In this table we can see output from *search.conv* analysis. Angle state is the mean θ angle between species assigned to state convergent. Convergence is reported as the percentage of significant instances of convergence found.

Discussion

Tseng et al. (2016) analysis indicates that the mosaic convergence between *Smilodon* and *Kolponomos* is functional and relates to the way they had to withstand strong torquing loads when biting prey with their canines pr whilst dislodging marine shelled organism fastened to the sea bottom, respectively.

Although this study (Tseng et al., 2016) focused on the mandible, the attachment areas of neck and masticatory muscles and the loadings they originate pertain to the cranium (Salesa et al., 2005). Therefore, we scanned this structure searching for any pattern of convergence between *Kolponomos* and sabretooth species. We found that *Kolponomos* skull shape falls well within the morphological variability of otariids, in line with its phylogeny (Paterson et al., 2020).

Even if *Kolponomos* is not closer in skull shape to *Smilodon* and the other sabretooths than the other pinnipeds it remains the most "sabretooth-like" among the pinniped. Also, it remains the closest to *Smilodon* and the other sabretooth in absolute terms in PC plots (Fig. 3).

It is possible to speculate the morphological proximity between otariids and sabretooth (Fig. 3) may have facilitated convergence between *Koloponos* and *Smilodon,* providing the former with the basic morphological equipment to deal with the especially demanding loadings originated at biting.

We used a recently implemented software tool which allows the users to chart phenotypic resemblance directly on the digital models (Melchionna et al., 2021) to investigate which part of the cranium of *Kolponomos* resembles sabretooths the most.

Smilodon and *Kolponomos* shapes are similar in the alveolar area around the canines, the postorbital constriction, and in the vast area of attachment of the *temporalis* and *profundus* muscle in the temporalis fossa (Wroe et al., 2013).

In *Smilodon* ad well ad in the other sabretooth, the low coronoid reduced the mechanical advantage of the temporalis (McHenry et al., 2007), compensated for the by the increased strength in the neck musculature, allowing strong lateral head movements during biting (Antón et al., 2004). Similar bite mechanics in *Kolponomos* is confirmed in *Kolponomos* by Tseng et al., (2016).

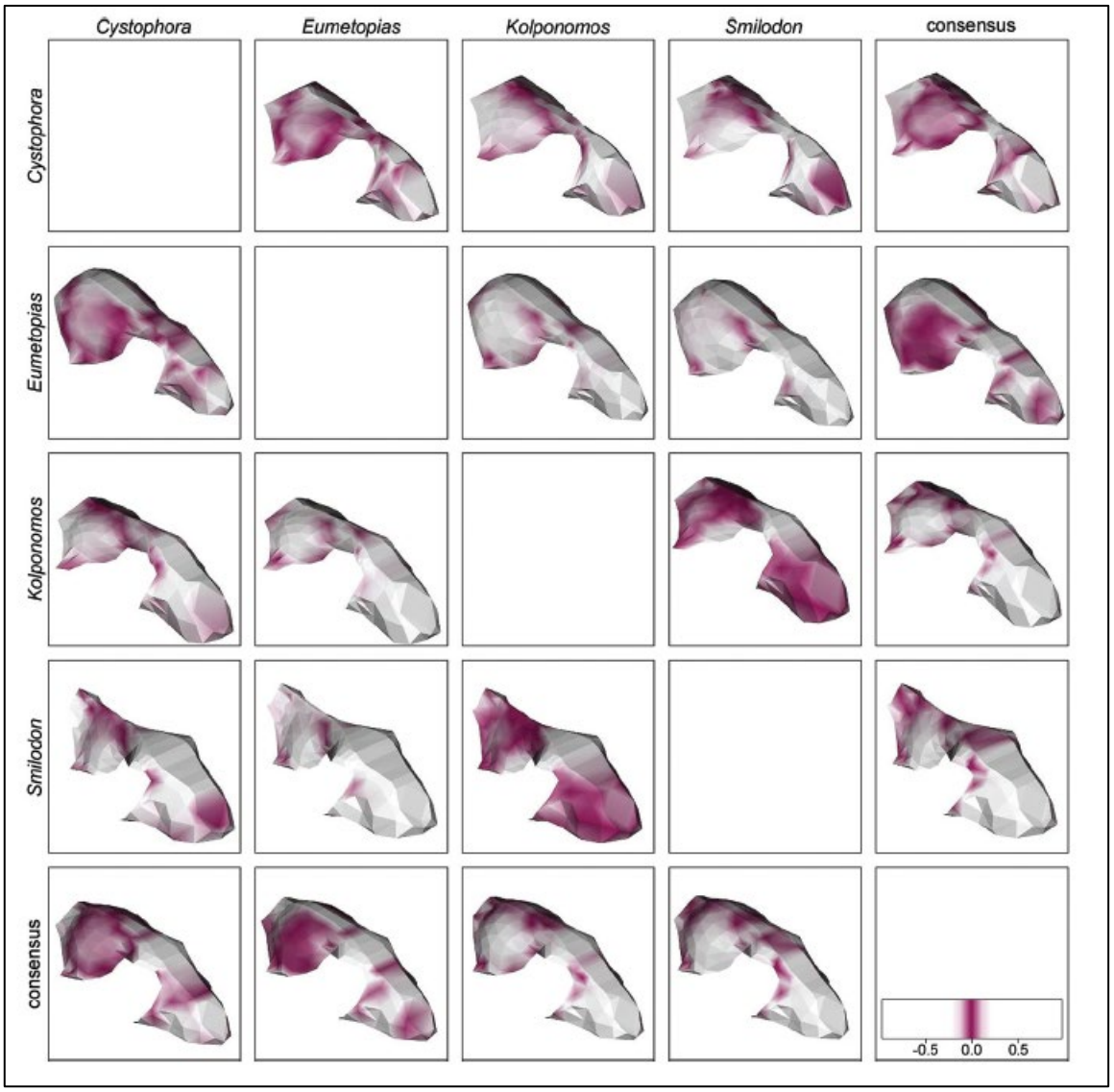

Fig. 4. Pairwise comparison between *Cystophora, Eumetopias, Kolponomos, Smilodon* and *consensus.* The colour gradient indicates local differences between the two surfaces. The scale bar was rescaled to the range 0-1. Differences between the two taxa are displayed on a reconstruction of the taxon named on the left.

Further, *Kolponomos* shares with sabretooth the derived shape of the mastoid process to provide attachment for an (inferred) massive atlanto-mastoid muscle, while it maintains a prominent coronoid process in agreement with its phylogenetic position. This provides convergence between *Kolponomos* and *Smilodon* in a localized area of the mandible, as driven by functional adaption to withstand strong torque loadings at biting. The cranium seems to conform to this pattern of mosaic convergence.

The areas of this structure which converge, clearly relate to the jaw-closing muscle and the canine area which are massive in both *Kolponomos* and *Smilodon* and represent the portion of the cranium

most solicited at biting. These findings indicate mosaic convergence between these two species extend to both component of the skull.

Also, convergence is a complex evolutionary pattern, whereby morphological resemblance does not confer adaptation to shared functional ends (Sansalone et al., 2020).

Even divergent morphologies may provide functional convergence (Alfaro et al., 2005; Wainwright, 2007; Losos, 2011; Renaud et al., 2018).

We emphasize the importance of visualizing pattern of morphological resemblance directly on phenotypes. The particular case of enigmatic *Kolponomos* further reminds us that convergence in response to a similar adaptive solicitation may be limited to restricted areas of an anatomical structure, which highlights the importance of mapping the potential patterns of convergence in phenotype of interest.

Human face-off: a new method for mapping evolutionary rates on three-dimensional digital models

SILVIA CASTIGLIONE[1] , MARINA MELCHIONNA[1] , ANTONIO PROFICO[2] , GABRIELE SANSALONE[3] , MARIA MODAFFERI[1], ALESSANDRO MONDANARO[4] , STEPHEN WROE[3] , PAOLO PIRAS[5] and PASQUALE RAIA[1]

[1]Dipartimento di Scienze della Terra, dell'Ambiente e delle Risorse, Università di Napoli Federico II, 80126, Napoli, Italy; silvia.castiglione@unina.it, marina.melchionna@unina.it
[2]PalaeoHub, Department of Archaeology & Hull York Medical School, University of York, Heslington, UK
[3]Function, Evolution & Anatomy Research Lab, Zoology Division, School of Environmental & Rural Science, University of New England, NSW 2351, Armidale, Australia
[4]Dipartimento di Scienze della Terra, Universit_a degli studi di Firenze, 50121, Firenze, Italy
[5]Via Romero Rodriguez Pereira, 00136, Rome, Italy

Palaeontology, Vol. 65, No. 1, p. e12582

https://doi.org/10.1111/pala.12582

Abstract

Per stimare i tassi evolutivi del cambiamento filogenetico ed in che modo cambiano tra i singoli cladi, ci avvaliamo dei PCMs (*phylogenetic comparative methods*).

Una loro limitazione però, sta nel dare come risultato una grandezza scalare. In questo lavoro, proponiamo quindi un nuovo metodo che permette di mappare la variazione del tasso evolutivo direttamente sui fenotipi. Abbiamo usato superfici tridimensionali, che informano automaticamente la direzione e l'entità del cambiamento del tratto considerato.

La funzione qui proposta è un'implementazione del pacchetto RRphylo, prende il nome di *rate.map* e pone le sue basi sulla *phylogenetic ridge regression*.

Presentiamo l'applicazione di questa tecnica direttamente sugli Hominoidea, clade che comprende il genere *Homo* e le grandi scimmie antropomorfe (sia viventi che estinti). Lo scopo del lavoro è stato quello di mappare l'evoluzione delle ossa facciali.

È stato scoperto che la forma del viso umana è frutto di rapidi cambiamenti fenotipici che coinvolgono tre zone: le ossa nasali, la cresta sopraccigliare e la regione mascellare.

Main text

Estimation of *tempo* and *mode* of evolution is the main purpose of PCMs (*phylogenetic comparative methods)* and now there are a lot of these tools available to estimate the rates of phenotypic traits to testing different evolutionary scenarios (Butler & King 2004; O'Meara 2012).

Most of phylogenetic comparative methods calculate the evolutionary rate as a measure of trait variance accumulation over the time, but they represent the global rate of phenotypic change for the whole structure or rate.

For this reason, we can't decompose any specific part of the phenotype under investigation. This interferes with our understanding of whether different portions of a complex phenotype evolve and in which direction.

With univariate data the results are scalar, and they do not offer the opportunity to determine how or whether various parts of the phenotype evolve along different paces and different lines.

Here we proposed a new method, *RRphylo.* It applies the phylogenetic ridge regression to estimate the evolutionary rate of phenotypic change for each branch of the tree. It also calculates ancestral states in the process (Castiglione et al., 2020).

RRphylo represents rates estimated at tree branches by phylogenetic ridge regression. Since slope have a magnitude and sign, the user can assess whether the phenotypic value increases or decreases, and at what speed, along the branches by looking at RRphylo rates alone (Prince-Waldman et al., 2020).

Performing RRphylo on PC scores derived from GMM (*geometric morphometrics)* analysis, which decomposes shape variation into orthogonal axes, RRphylo rates can inform about increasing or decreasing of PC scores, and how rapid these changes are. This is possible because PC saxes represent deformations of the reference mean shape.

So, computing *RRphylo* rates on PC scores offers the opportunity to visualize the direction and rate of change at specific location of the phenotype.

We proposed a new function in *RRphylo* v2.5.7 (Castiglione et al., 2018), an R package, named *rate.map,* This function allows the user to graphically visualize *tempo* and *mode* (rate and mode) of phenotypic change on anatomical structures of interest.

Rate.map identifies the PC axes linked to the highest and lowest evolutionary rate values and reconstructs the morphology weighted on selected PC axes. Thanks to this method, users can observe where and how the phenotype changed the most between any pair of taxa in the phylogenetic tree.

Rate.map can be also used to compare either a species to a parental node, or a pairs of species tracing back to their most recent common ancestor. We applied *rate.map* function on the facial skeleton in apes and hominins to study evolutionary rates.

Material

Data preparation

We assemble a 3D database with 42 surface skull mesh belonging to 12 species, extant and extinct, of Hominoidea (Castiglione et al., 2021). The living species are *Gorilla gorilla, Homo sapiens, Hylobates lar, Pan troglodytes, Pongo abelii, Symphalangus syndactylus.* Fossil species included: *Australopithecus africanus* (Sts5)*, Homo habilis* (KNM-ER 1813)*, Homo erectus* (Sangiran-17)*, Homo heidelbergensis* (Kabwe I, Petralona)*, Homo neanderthalensis* (Amud 1, Gibraltar 1)*, Homo sapiens* (Skhul-V)*, Paranthropus boisei* (KNM-ER 406).

3D mesh of the extant species other than *H. sapiens* were taken from: Smithsonian Institute digital collection and KUPRI (Digital Morphology Museum), while specimens of modern *Homo sapiens*

were downloaded from online database NESPOS. The 3D model of Sts-5 was acquired from the virtual anthropology of the University of Vienna. Amud I skull surface was kindly provided by I. Hershovitz and J. Abramov while Gibraltar 1, Sangiran-17, KNM-ER 1813, KNM-ER 406, Kabwe I and Petralona were kindly provided by G. Manzi.

Some fossil specimens presented missing parts and distortion in cranial shape due to taphonomic processes. For example, Gibraltar 1 skull lacks the left margin on the brow ridge and the zygomatic arch. KNM-ER 406 have incomplete and covered by matrix bones, such as the left zygomatic and maxilla. KNM-ER 1813 have the left orbit markedly deformed and lacks zygomatic bones and the left maxilla. For restoring missing parts, first we use the function *retroDeformMesh* from **Morpho** R package v2.8 (Schlager 2017, Schlager et al. 2018, 2020). Then, we created a mirrored version of the symmetrized surface and aligned them.

After that, using the software Geomagic Studio (2014), we selected the areas that need to be restored. We manually sample 29 anatomical landmarks on each cranium (Fig. 1, Table 1) using Amira software (v.5.4.5; Visualization Sciences Group, ©2013). We defined 500 semilandmarks per side, which are slide by using *slider3D* function of **Morpho** R package (Schlager 2017). Also, we symmetrize the bilateral semilandmark sets by using the function *symmetrize* in **Morpho.**

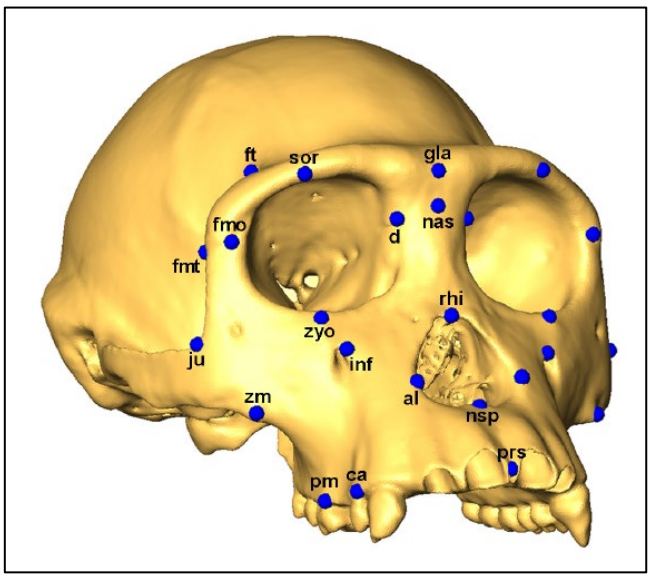

Fig.1. Landmark configuration used in this study.

N°	Landmark	Definition
1	Prosthion (prs)	Midline point at the most anterior point on the alveolar process of the maxillae
2	Nasospinale (nsp)	Lowest point of the inferior margin of the nasal aperture as projected on the mid-sagittal plane
3	Nasion (nas)	Midline point where the two nasal bones and the frontal intersect
4	Glabella (gla)	Midline bony prominence between the superciliary arches of the frontal bone, representing the most anterior part of the forehead looking straight ahead
5,6	Alare (al)	Most lateral point on the margin of the anterior nasal aperture
7,8	Zygoorbitale (zyo)	Point at which the orbital rim intersects the zygomaticomaxillary suture
9,10	Frontomalare orbitale (fmo)	Point at which the frontozygomatic suture crosses the inner orbital rim
11,12	Frontomalare temporale (fmt)	Point at which the frontozygomatic suture crosses the temporal line
13,14	Dacryon (d)	Point at which the maxillolacrimal suture meets the frontal bone
15,16	Zygomaxillare (zm)	Most inferior point on the zygomaticomaxillary suture
17	Rhinion (rhi)	Midline point at the inferior free end of the internasal suture
18,19	Jugale (ju)	Notch between the temporal and frontal processes of the zygomatic
20,21	Infraorbital foramen (inf)	Upper margin of the infraorbital foramen
22,23	Canine (ca)	External alveolar margin of the canine
24,25	Premolar (pm)	External alveolar margin of the second premolar
26,27	Superior orbital (sor)	Highest point on the orbital margin
28,29	Frontotemporal constriction (ft)	Point of narrowing of the cranium just behind the eye sockets

Table 1. Landmark descriptions and abbreviations. Landmark definition is from White et al. 2011.

Procrustes superimposition and RRphylo

Our goal was to chart evolutionary rates in the facial skeleton evolution of hominoids (human species included).

We performed GPA (*general Procrustes analysis* Gower 1975) to filter out non-shape differences, due to rotation, position, and size. Then, we performed PCA (*principal component analysis*) on the aligned landmark's coordinates. To do this, we used the function *procSym* from the Morpho package (Schlager, 2017). The function returns both scores from the PCA and aligned coordinates.

We computed evolutionary rates using the *RRphylo* function from the package **RRphylo** (Castiglione et al., 2018), using PC scores as shape information and a phylogeny with all species.

In hominins phylogeny *Homo sapiens* and *Homo neanderthalensis* are places as sister species. Moving from this pair, from the last to the most inclusive clade, the tree includes *Homo heidelbergensis, Homo erectus, Homo habilis*, australopiths and greater and lesser apes (Villmoare 2018; Diniz-Filho et al. 2019; Parins-Fukuchi et al. 2019; Puschel et al. 2021). For extinction dates, we use the last appearance for each species: *Australopithecus africanus,* 2,03 Ma (Pickering at al., 2019); *Homo habilis,* 1,6 Ma (de la Torre et al., 2021); *Homo erectus,* 0,1 Ma (Rizal et al., 2020); *Paranthropus boisei,* 1,34 Ma (Dominiguez-Rodrigo et al., 2013); *Homo heidelbergensis,* 224 ka (Lu et al., 2011; Arnold et al., 2015); *Homo neanderthalensis,* 40 Ka (Higham et al., 2014).

Mapping rates of shape evolution

From Procrustes superimposition and PCA we have PC scores, which we used to summarize the phenotype. For any two species in the tree, or for a species and its parental nodes, the function retrieves multivariate rates of phenotypic transformation from an **RRphylo** object (Fig. 2A-B, Table 2). The phenotypic difference between ancestor- descendant pair within the tree is defined by the sum of the subsequent changes along the path to the species.

Shape change is described by the algebraic sum of the evolutionary rate values computed along all branches between the ancestor and the descendent on phylogenetic tree, separately for each PC scores. This operation gives a vector $\boldsymbol{r}$ of rate sums; it has length n (the number of PCs).

For any pair of species, the resulting multivariate rate vectors, $\boldsymbol{r_1}$ and $\boldsymbol{r_2}$, describe the shape of change from each species.

The inflexion point is identified using R package **inflection** (Christopoulos 2019) with the function *ede*. This function is a distance estimator (Christopoulos 2012, 2016) to locate inflection points along a curve. We used identified PC axes along each vector to estimate the landmark configurations for the analysed species/nodes pair by using *showPC* function from **Morpho.**

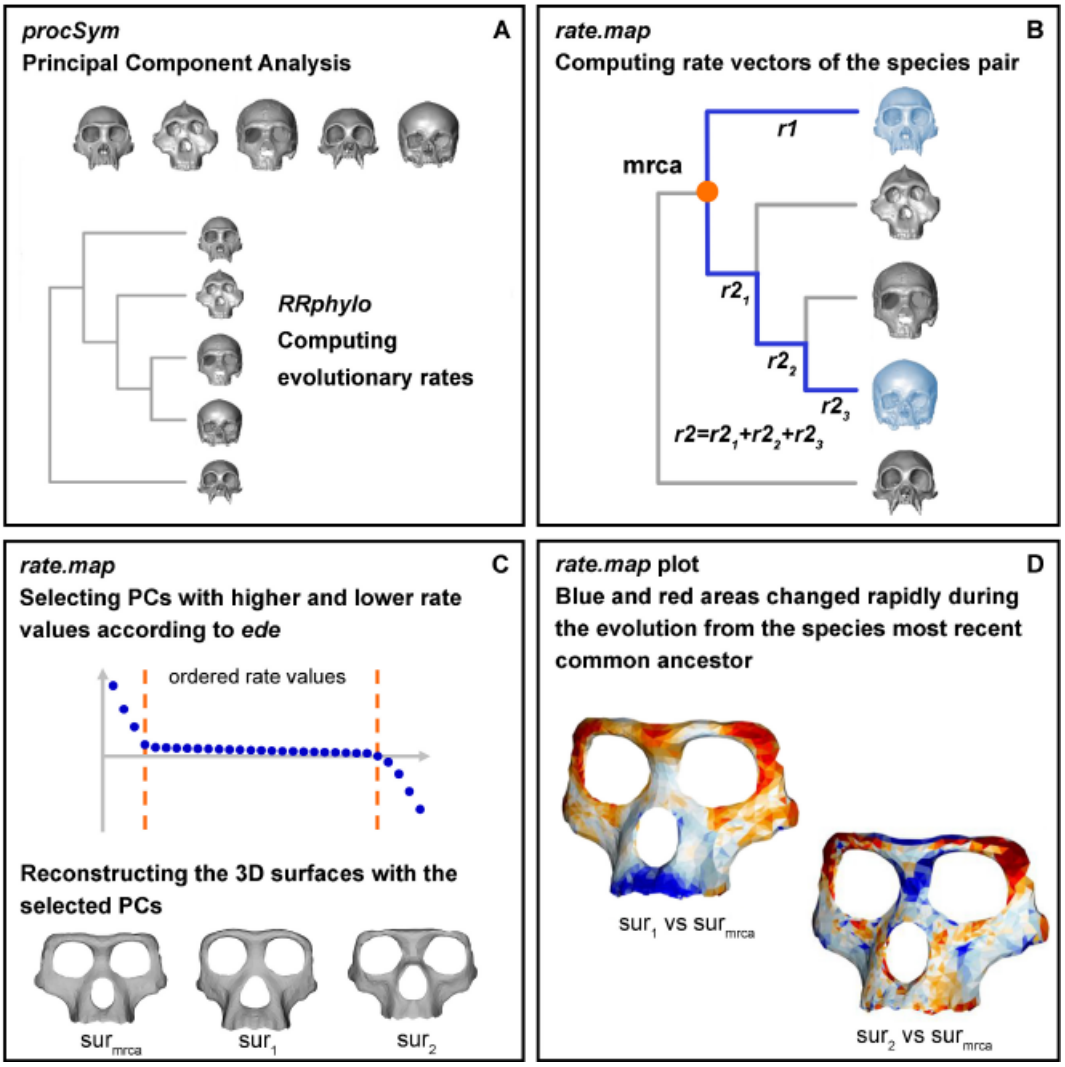

Fig.2. *rate.map* function workflow. **A**- morphological information and the evolutionary rates are the initial data. **B**- *rate.map* computes the rate vectors for each specie/node. **C**- highest and lowest vectors are selected in relation of the inflection points; associated PCs are used to reconstruct the surface of the two species/node and for the most recent ancestor (sur_1, sur_2 and sur_{mrca}). **D**- *rate.map* show the local area comparison in terms of expansion (blue) or contraction (red) between each surface and the most recent common ancestor of the species pair (mrca).

The function automatically reconstructs the new 3D surface (sur1, sur2) using the ball-pivoting algorithm (Bernardini et al., 1999). To do this procedure, we use the function *vcgBallPivoting* from the R package **Rvcg** (Schlager 2017). To reconstruct the landmark configuration and the 3D surface

of the ***MRCA*** (*most recent common ancestor*)- ***sur$_{rca}$***- we use the same procedure, but without selecting any PCs (Fig.2C).

sur$_{rca}$ was compared with ***sur$_1$*** and ***sur$_2$*** using the function *localmeshdiff* embed for the **Arothron** package (Profico et al., 2021). This function compares the area differences between corresponding triangles of each 3D mesh. Its final product, named *rate.map,* produces automatically a 3D plot that show comparison between ***sur$_1$*** and ***sur$_{rca}$*** and between ***sur$_2$*** and ***sur$_{rca}$***.

This result illustrates the magnitude and direction of phenotypic change for any pair of species.

We have also a colour gradient from blue to res, where blue represents expansion area of the mesh, while the red area represents contractions area of the mesh (Fig. 2D).

Argument name	Explanation
x	The species/nodes to be compared; it can be a single species, or a vector containing two species, or a species and a node to be compared
RR	An object generated by using the RRphylo function
Pcscores	PC scores
pcs	PC vectors of all the samples
mshape	The consensus configuration
out.rem	Logical: if TRUE triangles with outlying area difference are removed
shape.diff	Logical: if TRUE, the mesh area differences are displayed in a second 3D plot
show.names	Logical: if TRUE, the names of the species are displayed in the 3D plot

Table 2. *rate.map* arguments

Value	Explanation
Selected	List of PC axes selected for higher evolutionary rates for each species
Surfaces	List of reconstructed coloured surfaces of the given species and of the most recent common ancestor

Table 3. *rate.map* returned values.

The function *rate.map* allow us to inquire the morphological comparison of shapes by excluding the evolutionary rate component.

If we setting the argument *show.diff* = TRUE, the function will reconstruct ***sur1*** and ***sur2*** without selecting any PC axes. In this case, a second 3D plot will be displayed highlighting area differences in two colours: green for expansion and yellow for contraction.

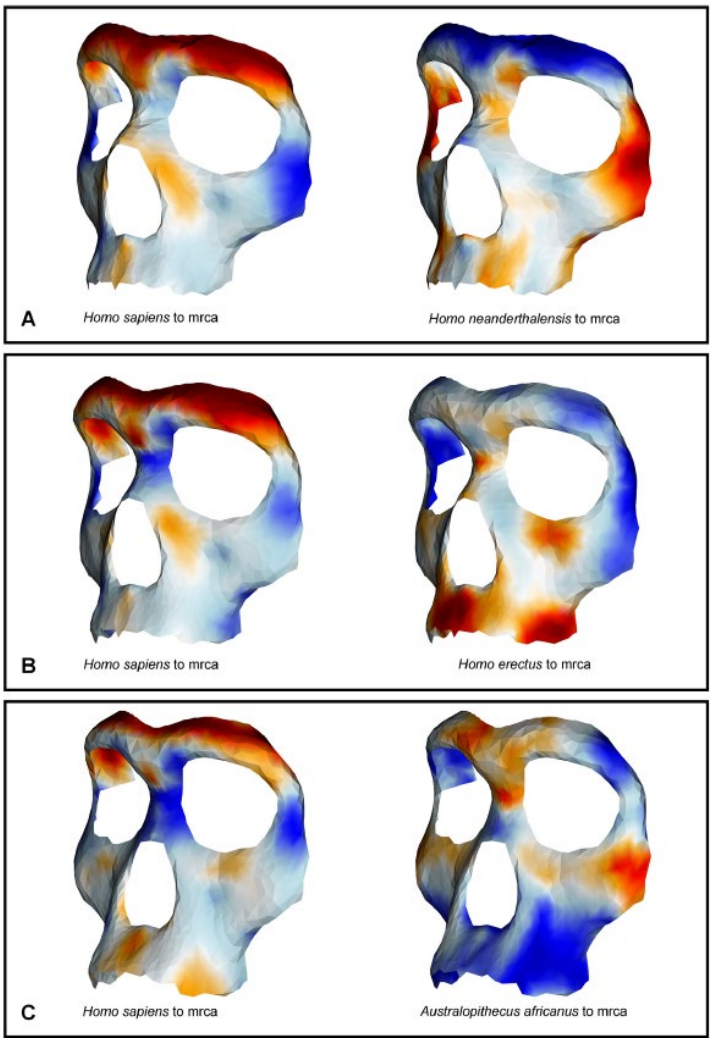

Fig. 3. We can see the pairwise comparison between *Homo sapiens* and A- *Homo neanderthalensis* B- *Homo erectus;* C- *Australopithecus africanus*. In each case, on the left we have the reconstructed surface of the MRCA of *Homo sapiens* and the comparator taxon using PC axes related to the highest evolutionary rates for *Homo sapiens.* On the right we use for comparator taxon the highest evolutionary rates. Colour gradient goes from blue (expansion) to red (contraction).

Results

Rate.map results shows three different comparisons: *Homo sapiens- Homo neanderthalensis; Homo sapiens- Homo erectus* and *Homo sapiens – Australopithecus africanus* (Fig. 3A, 3B,3C).

The first comparison is between *Sister species,* the two others between different lineages and, progressively, deeper common ancestor.

In the first case (Fig. 3A) we can see that the nasal region and the brow ridges changed very rapidly from those of their common ancestor. *H. sapiens* (on the left side) shows a restriction in the nasal area and a strong contraction of the brow ridge and a narrow piriform aperture.

H. neanderthalensis (on the right side) shows a large nasal cavity, while the midface is more prognathic, a feature which is often reported in literature (Stelzer et al., 2018).

The second one (Fig. 3B) shows the comparison between *H. sapiens* and *H. erectus.* Relative to their most common ancestor, in *H. sapiens* there is a great reduction in the brow ridge and a narrow skeleton in the upper face. Brow ridge in the lineage from the most recent common ancestor to *H. erectus* does not show high evolutionary rates.

The third one (Fig.3C) shows the comparison between *H. sapiens* and *A. africanus.* In the former, we see a rapid forward expansion of the nasal bones and of the brow ridge while the dental arch appears reduced and laterally compressed.

Discussion

In Hominoidea, facial morphology has a crucial role in communication, recognition, and expression of emotions (Du et al., 2014; Lacruz et al., 2019). While craniofacial bones are highly integrated with the brain case (Bastir & Rosas 2005; Marcucio et al., 2011), they have a lesser degree with the cranial base (Profico et al., 2017; Neaux et al. 2019). Changes among the neurocranial shape is likely to be the consequence of long-term trends toward increased brain size, bipedalism (Masao et al. 2016), but also the diet as well.

Early representative of the human lineage, like *Australopithecus* and *Paranthropus* may show a range of craniodental and osteological feature conferring adaptation to hard food consumption (Teaford & Ungar 2000; Strait et al., 2009).

Generally, living greater apes have a marked prognathism, long snouts and vertically deep faces.

Fossil instead, has a shorter midface, a vertical profile and follow a trend toward gracilization, but show a slightly prognathic premaxillary region. This feature is in common with the vasal hominin species (Stelzer et al. 2018; Lacruz et al. 2019).

If we consider the comparison between *H. sapiens* and *A. africanus,* we can see how evident this pattern is, such reduced prognathism, thinning and outward expansion of nasal bones.

Rates of the shape range are also evident in the *H. sapiens – H. neanderthalensis* pair, if we compare them to the shape of their most common recent ancestor.

Modern humans have thinner brow ridge and nasal bones relative to Neanderthals, while in Neanderthals there are an inflated canine fossa. These changes were attributed to ontogenetic bone modelling in Schuh et al. (2019), while for Maddux & Franciscus (2009) and Freidline et al. (2012) this pattern is a by-product of the formation of surrounding structures.

The reconstruction performed by *rate.map* indicates that the area of canine fossa has been affected by a lower rate of change, than the other surrounding regions.

These observations are consistent with the "spandrel-like" hypothesis (*sensu* Gould & Lewotib 1979).

Conclusion

RRphylo estimate the phenotypic evolutionary rates using the phylogenetic ridge regression. Using the shape data, each rate represents the magnitude and the direction of shape change attached to specific PC axes.

This offers the opportunity to show the rates on the phenotype, illustrating how and the degree the phenotype changes in course of evolution.

We developed the *rate.map* function to map the shape changes patterns. By applying this methodology on the facial shape of the Hominoidea lineage, we see that the modern human face is the product of rapid evolution while the region of canine fossa evolved slowly.

A method for mapping morphological convergence on three-dimensional digital models: the case of the mammalian sabretooth

MARINA MELCHIONNA[1] , ANTONIO PROFICO[2] , SILVIA CASTIGLIONE[1] , CARMELA SERIO[3] , ALESSANDRO MONDANARO[4] , MARIA MODAFFERI[1], DAVIDE TAMAGNINI[5] , LUIGI MAIORANO[5] , PASQUALE RAIA[1],* , LAWRENCE M. WITMER[6] , STEPHEN WROE[7] and GABRIELE SANSALONE[7]

[1]*Dipartimento di Scienze della Terra, dell'Ambiente e delle Risorse, Università di Napoli Federico II, 80126 Napoli, Italy; pasquale.raia@unina.it*
[2]*PalaeoHub, Department of Archaeology & Hull York Medical School, University of York, Heslington, UK*
[3]*Research Centre in Evolutionary Anthropology & Palaeoecology, School of Biological & Environmental Sciences, Liverpool John Moores University, Liverpool, UK*
[4]*Dipartimento di Scienze della Terra, Università degli studi di Firenze, 50121 Firenze, Italy*
[5]*Department of Biology & Biotechnologies 'Charles Darwin', University of Rome 'La Sapienza', viale dell'Università 32, 00185 Rome, Italy*
[6]*Department of Biomedical Science, Heritage College of Osteopathic Medicine, Ohio University, Athens, OH 45701, USA*
[7]*Function, Evolution & Anatomy Research Lab, Zoology Division, School of Environmental & Rural Science, University of New England, Armidale, NSW 235, Australia*
**Corresponding author*

Palaeontology, Vol. 64, No. 4, pp. 573-584

https://doi.org/10.1111/pala.12542

Abstract

Una delle limitazioni dei metodi statistici finora proposti è quello di non fornire la visualizzazione della convergenza, soprattutto se si stratta di aree piuttosto estese e strutturalmente complesse.

In questo lavoro proponiamo un nuovo metodo che invece permette proprio di tracciare questi modelli di convergenza su modelli tridimensionali. Per farlo, ci siamo avvalsi di una nuova funzione, presente nel pacchetto **RRphylo**, chiamata *conv.map.*

Abbiamo deciso di applicare questa nuova tecnica ad un gruppo molto noto; quello delle tigri dai denti a sciabola (*sabretooth* in inglese) un morfotipo evolutosi indipendentemente nei cladi di mammiferi sia placentali che metateri.

Il nostro obbiettivo era altresì identificare eventuali caratteri morfologici condivisi presenti in questi animali che potessero costituire la base per strategie di caccia simili. Abbiamo trovato che la convergenza morfologica nella parte rostrale e posteriore del cranio; il che suggerisce una somiglianza tra specie filogeneticamente distanti.

Main text

Convergence is the evolution of analogous body parts in phylogenetically distant species (Losos 2011; Wake et al. 2011). We have a lot of examples, such as neck elongation in both sauropod dinosaur and giraffes (Sander et al., 2010), elongated upper canines along several carnivore mammals (Wroe et al., 2008) and the trenchant- heeled condition of the lower molars of hypercarnivorous canids (Van Valkenburgh, 2007).

Most of statistical methods to study convergence pattern (Harmon et al. 2005; Stayton 2006; Adams & Collyer 2009; Muschick et al. 2012; Ingram & Mahler 2013; Stayton 2015; Castiglione et al. 2019) are limited to a positive or negative inference.

Generally, studies about morphological convergence are exclusive of body parts (e.g., wings, neck, or sabres) rather than structures or bodies of which they are part, with a few exceptions (Lingham-Soliar 2016).

Currently available methods can't identify specific regions within the structure or quantify the degree of convergence (McGhee 2011). This can have limitation about if convergence is restricted to superficial morphological resemblance or if it is product of shared selective pressure (Wainwright 2007; Moen 2019). Also, there is a difference between simple morphological convergence, which relates to phenotypic similarity, and functional convergence, which is present even without phenotypic resemblance.

Recently, we developed a new function *search.conv* (Castiglione et al., 2019), embed in the package **RRphylo** (Castiglione et al., 2018). This function permits pattern identification between different clades among phylogenies.

Search.conv computes the angle between PC scores (vectors of principal component) retrieved from geometric morphometric (GMM) analyses to evaluate whether two shape vectors are morphologically closer, so there is a small angle between them.

Since sequencing GM data by principal component analysis (PCA) represents both affine and non-affine shape change components, identifying PC axes responsible for the convergence pattern allow us to identify it in the focal biological shape, mapping, and quantifying which individual areas contribute to the overall convergence of the structure under study.

These concepts are central to the new methodology presented here: *conv.map.*

In this work, we applied *conv.map* to a classical example of convergence: the independent evolution of sabretooth morphology in predatory mammalian lineages. All sabretooth are defined by elongated teeth that are laterally flat. These are the upper canines (Emerson & Radinsky, 1980; Christiansen 2008); which are widely believed to have been used to kill large prey (Ackerstein, 1985; McHenry et al., 2007).

Variation in the postcranial morphology, such as canine length and forelimb strength, led researchers to speculate about differences in hunting behaviour among different sabretooth species (Duckler, 1997; Christiansen, 2008; Slater & Van Valkenburgh, 2008; Christiansen, 2011; Figuerido et al., 2018). However, most researchers, including those mentioned above, believe that, despite these differences, all sabretooth mammals specialized in killing large prey by stabbing them in the neck, as opposed to suffocating them with pinch-and-hold bite which is typical strategy used by cone-toothed cats (Wroe et al., 2013; Figuerido et al., 2018). Mechanical models demonstrate that sabretooth perform poorly than conical toothed carnivores in lateral shaking of the skull and jaw. However, they are better adapted to resist stabbing, driven by neck muscles.

Basing to FEA (finite element analysis) that included both sabre and conical- tooth cats' species, has been proposed that the increasing of canines in sabretooth species are characterized by a capacity to resist stabbing forces, but a diminishing ability to resist laterally directed forces (McHenry et al., 2007; Wroe et al., 2013; Figuerido et al., 2018).

Several authors have proposed quite diverse ways of killing and feeding, such as biting on the abdomen rather than the neck, and diets inclusive of internal organs and blood, rather than meat.

This position has proposed for both *Smilodon fatalis* (placental) and *Thylacosmilus atrox* (metatherian) taxa (Merriam &Stock 1932; Akersten 1985; Janis et al., 2020).

The most diverse hypothesis in recent time suggests that the taxon with the most hypertrophied canines, *Thylacosmilus atrox,* was not a predator at all, but a specialized scavenger (Janis et al., 2020).

Killing and feeding behaviour differ between sabretooths. So, we might aspect to find similarities in cranial shape and not shared across the functionally relevant regions of the cranium.

So our goal is here to determine how many and to what degree different anatomical regions of the cranium were shared across very distantly related clades. Also, where these differences are significant.

We applied our new function *conv.map* to a large sample of placental and metatherian taxa, and also to a wide range of other carnivorous species.

Material and method

Data preparation

We sampled 92 specimens. On each, we put manually 32 landmark, which configuration defines the shape of the dorsal regions of the cranium. We exclude from this configuration the zygomatic arch, that in fossil specimens is rarely represented.

After, we placed and slide 1000 semilandmark, 550 for each side, with the **Morpho** R package (Schlager et al., 2020).

Specimens include a barbourofelid, a scimitar-tooth and a dirk-tooth felid; also, we sampled genus *Neofelis* which displays the most morphological features common to extinct sabretooths (Christiansen 2008). We also include *Thylacosmilus atrox* and *Thylacoleo carnifex* to provide species phylogenetically near to *Thylacosmilus.* Our dataset comprised 49 species, both extant and extinct.

We symmetrize two mesh: *Barbourofelis frickii* and *Homotherum serum* because of taphonomic distortion. To do this, we use the function *retroDeformMesh* (Schlager et al.2018).

GPA (general Procrustes analysis) was applied by using the function *procSym* from the R package **Morpho**. GPA rotates, translates, and scales landmark configuration to the unit centroid size. Centroid size is the square root od squared differences between landmark coordinates and Centroid coordinates. Then, we applied ordination the align coordinates by means of PCA. Resulting PC scores represent the shape variables.

Searching for convergence

To perform convergence analysis, we implemented the felid phylogenetic tree, and we included the metatherian in it. After, we used *search.conv* function (Castiglione et al. 2019). This function test whether phenotypes in distant clades are more similar to each other than expected from their phylogenetic position. PC scores represents phenotype, and they are derived from geometric morphometric analysis. The phenotypic vectors are calculating in relation the origin of PC axes (the *consensus* shape in geometric morphometrics) and the angle they form represents a correlation coefficient. An angle close to 0° means convergence in shape, an angle close to 90° means dissimilarity and an angle close to 180° indicates phenotypes evolving in an opposite direction to the consensus.

Also, we applied *search.conv* to the sabretooth group to verify the convergence in the skull shape within the category.

Relative warp analysis

This new function embeds for the RRphylo package enable us to identify species which show convergent phenotypes. PCA can decompose the variability of the sample into orthogonal exes to describing shape variation around the sample mean shape.

Convergence, however, implies large scale, non-affine shape variation which is best inspected by means of PCA of a partial warp score weighted by a factor $\alpha > 0$ (α spans from $-\infty$ to $+\infty$; at $\alpha = 0$ RWA corresponds to PCA so that the affine and the non-affine components of shape variation are not separated, Rohlf 1993; Rohlf & Bookstein, 2003).

We performed relative warp analysis using the Morpho function *relWarp* (Schlager et al., 2020). Also, we set the parameter α to 1 and we extracted the RW scores and the RW vectors.

Mapping convergence

Conv.map function visualize the intensity of convergence on a 3D mesh. In RWA, we note that the user can use RW scores and PC scores.

Given two phenotypic vectors ρ_1 e ρ_2 of length n, the angle α between them is geometrically equivalent to the correlation coefficient between the vectors (Zelditch et al, 2012; Castiglione et al. 2019). Removing a pair of *i* of corresponding RW scores from both vectors, produced the angle α_i between the remaining scores $\rho_{1[-i]}$ and $\rho_{2[-i]}$ of length n-1.

If the removed pair of scores is important to phenotypic similarity $\alpha_i < \alpha$, and vice versa.

In the function *conv.map,* pairs of relative warp (RW) scores are removed on pair at time. The angle between the vectors of remaining RWs computed each time. After this procedure, the resulting angles $\alpha_{[1\ldots n]}$ are collated into a vector, from the largest to the smallest.

If all RWs are responsible for the phenotypic distance between the two original shape vectors, this vector will be flat.

Relative warp analysis decomposes the shape variance into orthogonal axes of maximal variation. So, the vector $\alpha_{[1\ldots n]}$ presents two inflection points. The former sets apart RW axes which contributes

most to the convergence patter, while the latter, if present, identifies the RW axes which are the most responsible of shape difference between the two phenotypic vectors.

We use the function *ede* from the R package **Inflection** (Christopoulos, 2019) to identify the first inflection point and then to select the PC axes responsible for convergence.

The function *ede* is an extreme distance estimator (Christopoulos, 2012; Christopoulos, 2016) and it efficiently locate the inflection points along a curve.

To do this, it finds the first inflection point the $RW_{conv1,2}$ matrix of *k* (which correspond to RW axes for each species) is extracted from vectors ρ_1 and ρ_2.

This procedure is analogous to the criterion used for the selection of relevant axes in principal component analysis (PCA), but it differs from the scree plot. In fact, it selects PC axes that explain most of the variance and it selects the $RW_{conv1,2}$ sets of scores in ρ_1 and ρ_2 in order to maximizes their similarity.

Conv.map computes the angle α_{conv} between the two vectors in $RW_{conv1,2,}$ to evaluate the statistical significance of the RW axes. Then, it computes 10 000 angles randomly, by selecting in ρ_1 and ρ_2 pairs. If α_{conv} is smaller than 5% of the random angles, it represents the subset of RW axes that best account for convergence.

We used *showPC* function from the R package **Morpho** to have a new landmark configuration from $RW_{conv1,2}$ scores. This new convergence is weighted on the variance responsible for convergence.

Using the ball-pivoting algorithm (Bernardini et al. 1999), the function automatically reconstructs a 3D mesh. The algorithm is embedded in the R package **Rvcg** (Schlager & Girinon, 2017) function *vcgBallPivoting.*

From this new surface, *conv.map* estimates the area differences between corresponding triangles of each 3D mesh and the consensus shape mesh of the original RWA.

If the species are convergent, they should present the same variation pattern and in the same region of 3D mesh. Convergent areas will show small variation where there are not convergent regions of the 3D surface (plotted in colour shades).

Same procedure could be generalized to >2 shape vectors at once. In this case, the user must supplement *conv.map* with a ρ shape vector for each species. Also, the user must indicate which species were found to convergence. Given *j* species, the function will calculate all the $RW_{conv1...j}$ matrices, one for each pairwise comparison, and selects the RW axes that appear more than once in the $RW_{conv1,2}$ matrices.

If $j > 2$ shape vectors are provided and comparison of convergence mapping are plotted against the consensus shape.

To resume, *conv.map* works as it follows:

- From ρ_1 and ρ_2 vectors, we can select the RW scores responsible for morphological convergence.
- Using both RW scores and RWs (the $RW_{conv1,2}$ matrix) we can reconstruct the landmark configuration.
- We have a triangle 3D mesh of both landmark configurations referring to ρ_1 and ρ_2 vectors, while we obtain consensus shape using the ball-pivoting algorithm.
- Each surface referring to ρ_1 and ρ_2 is compared to the consensus shape. Also, 3D mesh triangles areas differences are computed.
- Calculate the triangle mesh by referring to $RW_{conv1,2}$ and plot it on the 3D surface.

This function also gives the opportunity to exclude some RW axes from the analysis. This is because, for example, in most cases RW_1 captures high- older morphological differences guided to size variation and phylogeny in the sample.

Conv.map needs as input data: a data frame with RW or PC scores of each group of species; the matrix of RW or PC vectors and the number of RW or PC that will be excluded from the analysis (Table 1).

Function returns the index of the RW axes selected in $RW_{conv1,2}$, the angle alpha between ρ_1 and ρ_2, the angle α_{conv} between vectors $RW_{conv1,2}$, angle differences between $\alpha - \alpha_{conv,}$ the p value for α_{conv}.

Also, it plots 3D surface coloured according to the convergence pattern represented by $RW_{conv1,2}$.

Application of conv.map to sabretooth

First of all, we computed mean relative warp scores for all species in the phylogenetic tree, in order to chart convergence on sabretooth.

Also, we considered *Barbourofelis, Homotherium, Smilodon and Thylacosmilus* as sabretooth. After that, we use *search.conv* function using all PCs as the multivariate dataset, to represent shape.

Other sabretooth classification can't find convergence for *Neofelis* and *Yoshi,* even if they are frequently cited as showing common traits with sabretooth (*Neofelis*) and with the machairodontinae family (*Yoshi*). We used *conv.map* from a relative warp analysis with α=1 to do a comparison between sabretooth and consensus.

Also, we compared *Barbourofelis frickii* against machairodont and against *Thylacosmilus atrox.*

Argument name	**Explanation**
dataset	Data frame (or matrix) with the RW (or PC) scores of the group or species to be compared
pcs	RW (or PC) vectors of all the samples
mshape	The consensus configuration
conv	A named character vector indicating convergent species as ('conv' in 'dataset') and not convergent species ('noconv')
exclude	Integer: the index number of the RW (or PC) to be excluded from the comparison
out.rem	Logical: if TRUE triangles with outlying area difference are removed
show.consensus	Logical: if TRUE, the consensus configuration is included in the comparison
plot	Logical: if TRUE, the pairwise comparisons are plotted; for more than 5 pairwise comparisons, the plot is not shown
col	Character: the colour for the plot

names	Logical: if TRUE, the names of the groups or species are displayed in the 3D plot

Table 1. Argument name and explanation of *conv.map* function.

Value	Explanation
angle.compare	Data frame including the real angles a between the given shape vectors, the angles aconv computed between vectors of the selected RWs (or PCs), the angles between vectors of the non-selected RWs (or PCs), the difference a-aconv, and its p-values
selected.pcs	RWs (or PCs) axes selected for convergence
average.dist	Symmetrical matrix of pairwise distances between 3D surfaces
surface1	List of coloured surfaces; if two meshes are given, it represents convergence between mesh A and B charted on mesh A
surface2	List of coloured surfaces; if two meshes are given, it represents convergence between mesh A and B charted on mesh B
scale	The value used to set the colour gradient, computed as the maximum of all differences between each surface and the mean shape

Table 2. *Search.conv* returned values and explanation.

Results

The results of *search.conv* analysis showed significant convergence among carnivores, with only species belonging to the sabretooth group that show a significant convergence (mean angle=43.88°, p=0.017).

Paired angle comparison between *Barbourofelis, Homotherium, Smilodon* and *Thylacosmilus* are presented in Table 3A. The angle differences (calculated angles between selected and unselected RW score vectors) of all the convergent groups are significant. Comparison with the consensus shape is not significant or marginally significant for each sabretooth (Table 3A).

Barbourofelis frickii and *Homotherium serum* have the least distance among all pairwise comparison, as we can also see in the convergence plots (Fig. 1). All carnivore sabretooths are distant equally from the consensus shape (Table 3B).

Comparison between 3D surface shows a significant similarity in the carnassial and premaxillary areas, and in the occipital region on and around the nuchal crest.

The nature of differences against the consensus is similar for all sabretooth taxa (Fig.1).

Comparing *Barbourofelis, Thylacosmilus* and the consensus to each other, the angle differences between the convergent species are the only statistically significant example found (Table 4A).

The smallest area difference is between *Barbourofelis frickii* and machairodont cats.

With a similarity in the muzzle area, *Thylacosmilus atrox* is closer to *Barbourofelis frickii* than to machairodonts. All groups are far from the consensus (Table 4B, Fig.2).

Discussion

We know that in convergence species belonging to different lineages develop similar structures that have same function (Wainwright 2007; Wroe & Milne 2007; Losos, 11; McGhee, 2011).

But evolution of convergence traits can trace different morphological trajectories (Alfaro et al., 2005; Serb et al., 2017; Renaud et al., 2018) and often convergence fail to apply then the structures' functional performance is ignored (Sansalone et al., 2020).

The aim of this study is to reveal such particularities and how and who contribute to the pattern of convergence.

A	**Real angle**	**Selected**	**Others**	**Angle Differences**	***p*- value**
Smilodon–Thylacosmilus	53.351	14.929	143.828	-128.899	<0.001
Barbourofelis–Homotherium	28.62	15.326	64.012	-48.66	<0.001
Homotherium–Smilodon	23.46	20.467	33.301	-12.834	0.061
Barbourofelis–Thylacosmilus	48.382	24.667	117.86	-93.192	<0.001
Barbourofelis–Smilodon	36.887	26.532	76.896	-50.364	0.01
Homotherium–Thylacosmilus	59.022	27.838	138.987	-11.149	<0.001
Barbourofelis–consensus	81.17	45.77	84.033	-38.263	0.067
Thylacosmilus–consensus	87.711	54.637	65.968	-41.331	0.09
Homotherium–consensus	83.943	61.016	86.508	-25.492	0.354

Smilodon–consensus	85.859	66.651	89.063	-22.412	0.366

B	***Barbourofelis***	***Homotherium***	***Smilodon***	***Thylacosmilus***	***Consensus***
Barbourofelis	-	0.053	0.069	0.08	0.213
Homotherium	0.053	-	0.066	0.112	0.172
Smilodon	0.069	0.066	-	0.075	0.205
Thylacosmilus	0.08	0.112	0.075	-	0.248
Consensus	0.213	0.172	0.205	0.248	-

Table 3. pairwise between these genera: *Barbourofelis, Homotherium, Smilodon, Thylacosmilus* and the consensus shape. A- pairwise angle comparison.
B- pairwise average area differences, rescaled from 0 to 1.

Conv.map helps to identify morphological regions which are responsible of functional convergence. Thanks to their complexity, vertebrate's skull is an ideal case study to identify and quantify convergence. In this study, we consider as an example, the sabretooth ectomorph.

We choose four taxa that share more anatomical traits than any other carnivore group, suggesting a strong selective pressure that drive the evolution of these features.

The function shows shared anatomical structures, such are: premaxillary area, carnassial region, occipital region, the nuchal crest. The last one, the nuchal crest, is common to all sabretooth carnivore, both mammalian and both metatherian, like *Thylacosmilus.*

These features allow these animals to have their killing behaviour. Sabretooth also have strong neck musculature, low condyles in the posterior part of the cranium and large gape to use the sabre.

In our view these elements support the consensus view that sabretooth morphotype confers a comparable capacity to hunt and kill rapidly large prey, by applying a stabbing bite thanks to powerful neck muscles (Emerson & Radinsky, 1980; Wroe et al., 2013).

However, this hyper specialization led the sabretooth to extinction, mostly when large prey become less abundant (Piras et al., 2018). The presence of similarities to dental and rostral areas represent functional adaptation related to relatively high loadings to the muzzle when the animal bites.

We found that convergence in sabretooth involves in particular carnassial and premaxillary area. Also, we found that there are similarities in the occipital area, which participated in extensive neck muscle of the skull (Ducker, 1997; Christiansen, 2008). *Thylacosmilus* is apart than the other

sabretooth because there is not influence of convergence from neurocranial, nasals and maxillary areas (Table 4, Fig. 2). *Barbourofelis* is closer to *Homotherium* than *Smilodon.* It is probably because of similarity in their incisor arcades (Biknevicius et al. 1996).

There is a great similarity between *Thylacosmilus* and *Barbourofelis.* This suggests that the metatherian sabretooth converged more on the high specialized barbourofelid. Other works suggests that these genera converged because of the presence of long canines, mandibular flange, and other postcranial features (Prevosti et al., 2012).

Fig. 1. There is comparison between *Barbourofelis, Homotherium, Smilodon* and consensus. The colour gradient indicates area differences between two surfaces. Blue colour indicates no differences. Bar scale ranges between 0-1.

The results support the hypothesis that the *conv.map* pattern of convergence of sabretooth skulls show primary functional significance, but secondary functional diversity may exist between sabretooth (Lautenshlager et al., 2020). The absence of convergence in the nasal area and in the neurocranium

is consistent with previously identify features and does not indicate prey selection or killing (e.g., the small brain of *Thylacosmilus*).

A	Real angle	Selected	Others	Angle difference	*p*- value
Barbourofelis - *Thylacosmilus*	48.382	3.941	93.912	-89.971	0.009
Barbourofelis - Machairodont cats	12.455	7.3	18.475	-11.175	0.073
Machairodont cats - *Thylacosmilus*	51.846	11.241	103.093	-91.852	0.012
Thylacosmilus - consensus	87.711	51.603	94.427	-42.824	0.285
Barbourofelis - consensus	81.17	55.544	81.629	-26.085	0.413
Machairodont cats - consensus	82.141	62.844	81.833	-18.989	0.474

B	*Barbourofelis*	Machairodont cats	*Thylacosmilus*	Consensus
Barbourofelis	-	0.039	0.054	0.347
Machairodont cats	0.039	-	0.085	0.308
Thylacosmilus	0.054	0.085	-	0.371
Consensus	0.347	0.308	0.371	-

Table 4. Comparison between *Barbourofelis, Homotherium* and *Smilodon* (machairodont cats), *Thylacosmilus* and consensus shape. A- pairwise angle comparison. B- pairwise area differences (rescaled from 0 to 1).

Thylacosmilus may have been a scavenger and that distinguish them from the other conical-tooth predators. We do not contest that *Thylacosmilus* was better adapted to exert pulling behaviour, because of the only FEA-based study (Wroe et al., 2013).

In this study, Wroe et al., (2013) found that *Thylacosmilus* was better than *Smilodon* to deliver a stabbing bite, but both were better in this than *Panthera pardus* (modern leopard). We suggest that *Thylacosmilus* was admirably adapted to deliver both neck-driven head pulling and depressing functions. There is no mechanic evidence to indicate if *Thylacosmilus* has a capacity to deliver a head pull and if it is a defining feature of sabretooth or not.

Janis et al., (2020) did a FEA-based analysis, which results are that *Thylacosmilus* did not habitually eat meat or bones. Probably, *Thylacosmilus'*s diet is largely based on soft internal organs (e.g., heart, lungs, and liver). These habits would make *Thylacosmilus* an incredibly unique animal among scavengers. Also, large extant mammalian carnivores consume preys' internal organs rather than meat and bone (Schaller, 1972).

Thylacosmilus probably concentrated its diet on the internal organs of the pray, rather than scavenge carcass of animals, because it was difficult to find internal organs untouched. Sabretooth had a weak jaw closing muscles, but a strong head depressor (Wroe et al., 2005; Christiansen, 2011). *Thylacosmilus* is extreme with both traits (Wroe et al., 2013), and we argue that these traits, together with evidence of a diet consisting most of soft organs, indicates an extreme example of sabretooth killing and feeding behaviour. It is opposite to an entirely divergent ectomorph and diet.

Conclusion

3D model revolutionized fossil study in both palaeontology and palaeoanthropology (Cunningham et al., 2014). Implementation of geometric morphometric techniques drive the development of new software suitable for 3D surface model. These innovative technologies allow researchers to virtually restore and realign element (Gunz et al., 2009; Profico et al., 2019). Also, it can perform the retrodeformation in case of damaged fossil record.

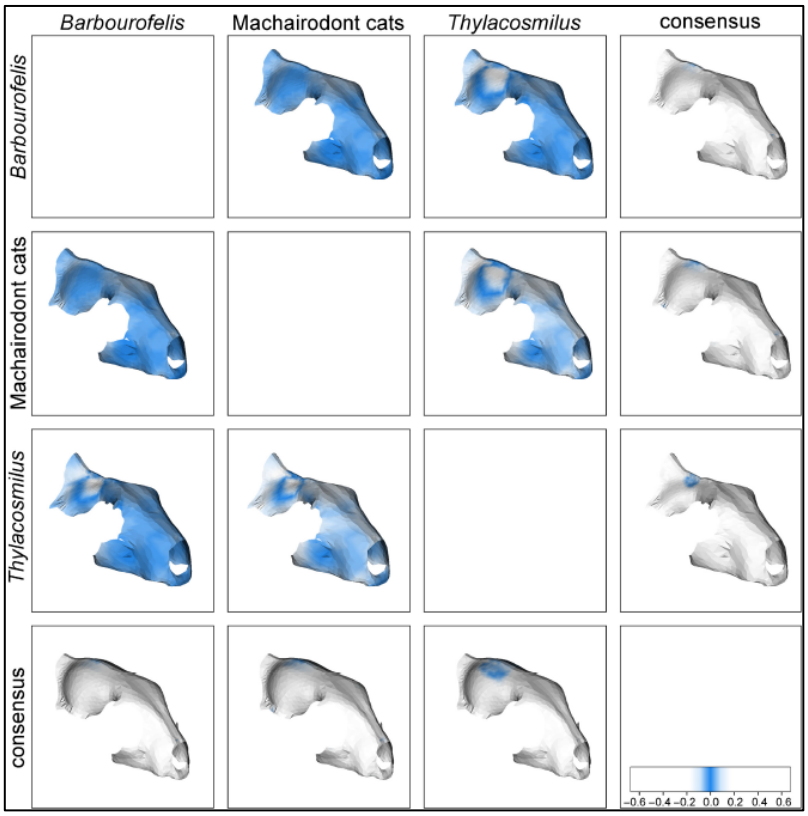

Fig.2. Pairwise comparison between *Barbourofelis,* Machairodont cats*, Thylacosmilus* and consensus. The colour gradient indicates area differences between two surfaces. Blue colour indicates no differences. Bar scale ranges between 0-1.

These methods permit to study functional and evolutive aspects of 3D shape evolution with increased precision. In this study, we present a new function *conv.map,* which allows us to study convergence pattern across 3D surface. Also, *conv.map* allow us to visualize the functional significance of convergence of morphological structures under study.

A Major Change in Rate of Climate Niche Envelope Evolution during Hominid History

ALESSANDRO MONDANARO,[1,2] MARINA MELCHIONNA,[1] MIRKO DI FEBBRARO,[3] SILVIA CASTIGLIONE,[1] PHILIP B. HOLDEN,[4] NEIL R. EDWARDS,[4] FRANCESCO CAROTENUTO,[1] LUIGI MAIORANO,[5] MARIA MODAFFERI,[1] CARMELA SERIO,[6] JOSE` A.F. DINIZ-FILHO,[7] THIAGO RANGEL,[7] LORENZO ROOK,[2] PAUL O'HIGGINS,[8] PENNY SPIKINS,[8] ANTONIO PROFICO,[8] AND PASQUALE RAIA[1,9,*]

[1] *Department of Earth, Environmental and Resources Sciences, University of Naples "Federico II", Naples 80126, Italy.*
[2] *Department of Earth Science. University of Florence, Florence 50121, Italy.*
[3]*Department of Bioscience and Territory. University of Molise, Pesche, Isernia 86090, Italy.*
[4]*School of Environment, Earth and Ecosystem Sciences, The Open University, Milton Keynes MKT 6BJ, UK.*
[5]*Department of Biology and Biotechnologies Charles Darwin, University of Rome La Sapienza, Roma 00185, Italy.*
[6]*Research Centre in Evolutionary Anthropology and Palaeoecology, School of Biological and Environmental Sciences, Liverpool John Moores University, Liverpool L3 3AF, UK*
[7]*Department of Ecology, ICB, Universidade Federal de Goiás, Goiânia 74968-755, Brasil*
[8]*Department of Archaeology and Hull York Medical School, University of York, York YO105DD, UK.*
[9]*Lead contact.*
[*]*Correspondence.*

Iscience, *23*(11), 101693

https://doi.org/10.1016/j.isci.2020.101693

Abstract

Grazie alle sue capacità cognitive, *Homo sapiens* è stata l'unica specie che è riuscita a colonizzare ogni angolo del pianeta, occupando una quantità di nicchie ecologiche di gran lunga superiore rispetto a qualsiasi altro animale.

La comunità scientifica, tuttavia, non ha ancora raggiunto un comune accordo su quando è avvenuto questo cambiamento e soprattutto, molti studiosi non sono d'accordo sul fatto che i nostri antenati condividessero questa stessa abilità.

Lo scopo di questo lavoro è quello di risolvere tale quesito e per farlo ci siamo avvalsi di dati paleoecologici e di metodi filogenetici comparativi.

Dai nostri risultati si evince che è solo a partire dalla comparsa di *Homo heidelbergensis* che la nicchia climatica del genere *Homo* si è espansa ben oltre i propri limiti, nonostante il cambiamento climatico. Ciò implica che sono state le innovazioni tecnologiche a fornire uno sfruttamento efficace anche di habitat molto freddi prima della comparsa di *Homo sapiens.*

Main text

Genus *Homo* has existed for about three million years (Harmand et al., 2015; Villmoare et al., 2015). For a third of this period, human species were native and confined to tropical and sub-tropical Africa (Carotenuto et al., 2016; Lordkipanidze et al., 2007), where warm, savannah-like environments abounded and to which early hominins were best adapted (Lee-Thorp et al., 2010; Wite at al., 2009). With the emergence of *Homo erectus* species about two million years ago, hominins began to roam out of Africa. However, they remained confined to low latitudes, probably due to a combination of physiological limits to cold tolerance (Dunbar et al., 2014) and inevitable constraints associated with biogeographic barriers. Yet, later *Homo* species were able to extend their distribution in Northern Europe and Western Siberia, despite the contemporaneous establishment of full glacial cycles that was making global temperature lower than before in the history of the genus.

Happisburgh and Pakefield (UK) sites represented the earliest *Homo* occurrence at the southern edge of boreal zone, about 0.7- 0.9 million years (Parfitt et al., 2010). The occupation of such boreal zone presents a substantial challenge, because not only cold climate challenged hominins which are adapted to African climate, but also the seasonality meant annually fluctuation of resources that are necessary to survive (Pearce et al., 2014). Adaptation that facilitating survival in cold environment

included: use of fire, shelter or clothing, weapons to hitting large species (Thieme, 1997), and an extended social network, with infants particularly susceptible to mortality (Spikins et al., 2019; Martin et al., 2020).

Unfortunately, clothing manufacture leaves us few "fossils" (Hosfield, 2016). The first evidence of hide scraping (for clothing) at Hoxne (UK) Biache-Saint-Vaast, Pech de l'Azé and Abri Peyrony (France), and Shöningen (Germany) (d'Errico and Henshilwood, 2007; Gilligan, 2010; Henshilwood et al., 2002) is just about 50 ka old at the most (Kittler et al., 2003; Gilligan, 2007).

Only *Homo neanderthalensis* and *Homo sapiens* left evidence that they were able to make complex clothing at the time. In the particular case of *Homo neanderthalensis*, combination of biological adaptations and material culture allow them to withstand the cold. This human species possessed relatively short limbs, large midface, and nasal cavity, to humidify and heat inspired air, although this question remains unresolved and there is no evidence for the contrary (Rae et al., 2011; Benito et al., 2017; Wroe et al., 2018). *Homo sapiens* instead, is considered the only human species that can occupy cold regions through a purely cultural process, driven by our technology, from fire use to clothing craftmanship and construction of shelters (Boivin et al., 2016; Gilligan, 2010; Hiscock, 2013; Laland et al.,2001).

Homo sapiens archaeological record shows us that our species was able to create its own niche, using technology that was transmitted across a wide geographical range and through cultural interaction.

Also, our species was able to climatic change over time and space, rather than being physiologically restricted by it (Banks et al., 2006, 2008, 2011, 2013; Dunbar et al., 2014; Spikins et al., 2019; Nicholson, 2019; Xu et al., 2020).

This view distinguished *H. sapiens* from any other human species in terms of cognitive abilities and implicitly rejects the idea that older *Homo* species could have had enough modern material culture to overcome climate harshness (Roberts and Stewart, 2018).

The question of when humans first became cognitively and culturally capable of extending their climatic tolerance beyond their physiology remains extremely difficult to decipher, given the paucity

of clothes fossil record and the tools used to make them. Also, there is a great uncertainty about local paleoclimate and the time and direction of human dispersal.

Here, we considered the question of when and which human species was involved by the expansion of climatic tolerance. We considered the implication of our findings for the timing of such adaptation, rather than underlying the cultural and social adaptation.

We model the evolution of climatic tolerance limits in the *Homo* genus by linking paleoclimatic values with fossil occurrence in archaeological record.

Our hypothesis is that *Homo sapiens* had a greater climatic tolerance than *Homo heidelbergensis* and *Homo neanderthalensis.*

To test our hypotheses, we evaluate the rate of change of climatic tolerance across the human phylogenetic tree and also search for shifts in these rates.

We applied method to calculate the rate of evolution of climatic niche at each branch of phylogenetic tree.

Study of shift in evolutionary rates of climatic tolerance, including the Happisburgh/Pakerfield hominins, *Homo heidelbergensis, Homo neanderthalensis, Homo sapiens* (MHS). These hominins are the first to acquire the technical skills and cultural adaptation to survive the cold climate.

Instead, if either no shift occurs or the rates overlap with different clades (e.g., early *Homo sapiens,* EHS) the northern habitats colonization would not be indicative of any rapid increase in the ability to withstand environmental harshness.

Our dataset included 2597 occurrences of both hominid remains and both artifacts associated with 727 archaeological sites. We consider a time range that start from the first occurrence of *Australopithecus,* about 4.2 million years ago in East Africa, to the *Homo sapiens* arrival in Europe dated around 0.040 million years (Raia et al., 2020).

This wide range of taxa provides a phylogenetic context for the analysis.

To get spatiotemporally precise climatic data for the past, dynamic climate modelling is required, but the timeframes for human evolution outstrip the capabilities of direct model simulation by many orders of magnitude.

To overcome this limitation, we combined direct simulation with statistical modelling using a computationally efficient, intermediate complexity Earth system model, the Planet Simulator-Grid-Enabled Integrated Earth system model (PLASIM-GENIE), to create PALEO-PGEM, a paleoclimate emulator capable of performing multi-million-year simulations forced by observationally derived proxy time series for ice sheet state, CO2 concentration, and orbital forcing (Holden et al., 2016, 2019).

We used RRphylo (Castiglione et al., 2018) to model the realized niche evolution.

This method allows us to compute evolutionary rates for each branch of phylogenetic trees and to estimate the ancestral phenotypes (Raia et al., 2018; Melchionna et al., 2020b; Baab, 2018). For our purposes, the phenotype includes climatic tolerance limits.

We used annual maxima and minima temperature, precipitation, net primary productivity data from PALEO-PGEM. Then, we reconstructed and projected the climatic niche limits, that corresponding to the ancestral species distribution, onto geographical space.

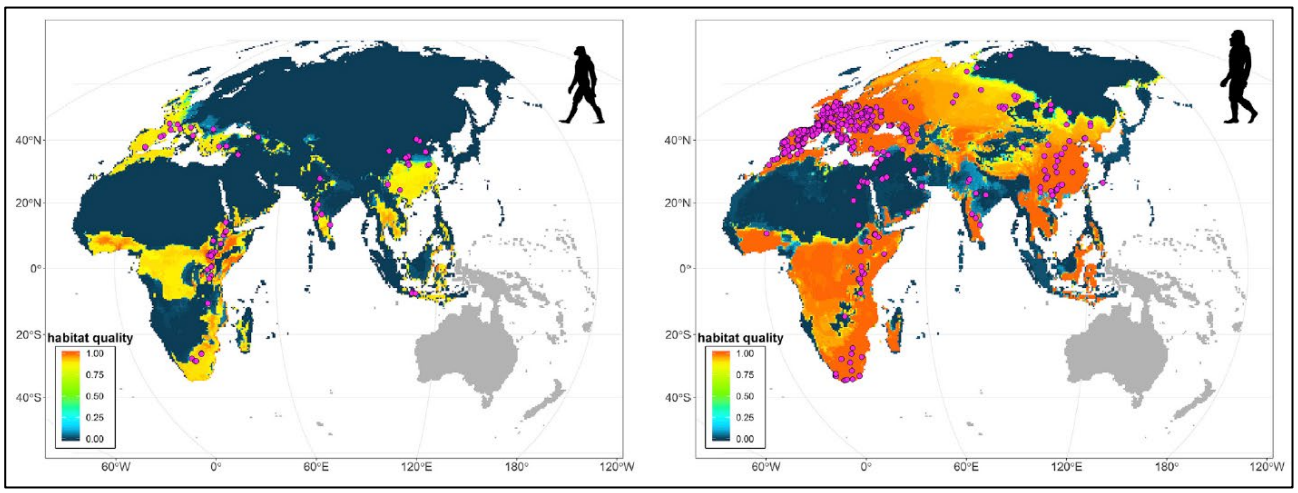

Fig.1. Habitat quality map for EHS (early *Homo sapiens*) and MHS (modern *Homo sapiens*). In blue there are a little suitability and in red there are a highly suitability. The fossil occurrence of EHS (*Homo habilis, Homo ergaster,* and *Homo erectus*) and MHS (*Homo heidelbergensis, Homo neanderthalensis* and *Homo sapiens*) are superimposed on each map.

With **RRphylo**, we can infer climatic niche tolerance (Quintero and Wiens, 2013) for each node in phylogenetic tree and also to see if the climatic niche evolution presents any positive or negative shifts. We compensated for phylogenetic uncertainty by randomly perturbing tree node ages and tree topology one hundred times. We were able to create an overall "habitat quality" (HQ) measure by adding phylogenetic uncertainty in this way, signifying the number of times (out of 100 repeats) a geographic cell was deemed liveable (e.g., it falls within climatic tolerance limits) for a particular ancestor in the tree.

Results

The association between the distribution of fossil species and habitat quality

The area under the curve (AUC) metric was used to assess the relationship between HQ and the location of fossil occurrences. The association would be ideal at AUC = 1. AUC = 0 indicates a perfect inverse relationship, while AUC ~ 0.5 indicates a random association. Despite the enormous geographic variation in both preservation potential and intensity of paleontological sampling (Carotenuto et al., 2010), we discovered a strong relationship between the geographic position of archaeological remains and the inferred suitability of the environmental conditions for both EHS (AUC = 0.80, Figure 1 left, AUC after subsampling the most abundant species = 0.71) and MHS (AUC = 0.81, Figure 1 right, AUC after subsampling the most abundant species = 0.82).

This strong association holds true for all nodes in the hominin tree (Figures S1 and S2, Tables 1 and S2), implying that climatic variation in time and space strongly influenced our ancestors' geographic ranges. Excluding extreme climatic values (i.e., climatic records above the 90th percentile of the individual variable distributions) to mitigate the effect of potential errors in the paleoclimate emulator, the AUC value for EHS decreased to 0.68, while it increased to as high as 0.82 for MHS (Table S3, Figure S3). We repeated this test by randomly distributing species fossil occurrences across their biogeographical domain (Table S4, Figure S4) to simulate a scenario in which there is no association between the archaeological record and HQ.

The AUC values decrease toward 0.5 in this simulation, indicating a non-significant association between the two variables (EHS AUC = 0.56; 95%, confidence interval: 0.52-0.61; MHS AUC = 0.58, confidence interval: 0.56-0.60). This discovery supports the idea that the geographic location of archaeological sites is a non-random process influenced by climatic variability.

Rates of hominin climatic niche limit niche evolution

We discovered a significant evolutionary rate shift toward wider climatic tolerance in the clade identified by *H. heidelbergensis*, *H. neanderthalensis*, and *H. sapiens* and their common ancestor (Figure 2). The rate shift is independent of the specific phylogenetic hypothesis (tree topology) assumed, as well as the species we used.

Species	Shift	Node with Two species	Node with Three species	*H. heidelbergensis*	*H. neanderthalensis*	*H. sapiens*
H. heidelbergensis	86	23	63	/	75	74
H. neanderthalensis	85	22	63	74	/	74
H. sapiens	86	23	63	75	74	/

Table 1. Percentage of Significant Rate Shifts in Niche Width Calculated through Phylogenetic Reshuffling. The table lists the percentage of significant shifts that occurred at nodes with two or three species, as well as the occurrence of each of the three Homo species in each significant shift.

When the tree node ages (to account for dating error) and species locations in the hominin tree (to account for phylogenetic uncertainty) are changed at random 100 times, the shift appears 95 times for this clade (Table 1). Subsampling the most numerous species (randomly picking no more than 100 fossil occurrences per species) to account for sampling disparities across species, the shift appears 91 times out of a hundred. We also performed the phylogenetic reshuffling, deleting randomly one species at a time. Under this latter arrangement, the MHS shift happens 63 times out of 100, and the change involves two, rather than three, MHS species 23 times more.

Individually, *H. sapiens* and *H. heidelbergensis* appear in 86 rate shifts, *H. neanderthalensis* in 85, and no shift exists outside the MHS clade, indicating that the rate shift is exclusive to these species and is not led preferentially by any of the three (Table 1).

Discussion

The calculated values of realized climatic niche limits at the inner nodes in the hominin tree imply that the rate change in the MHS clade's climatic niche limits was not only due to biological processes. At the root of the hominin tree (node 11, Table S1), yearly temperatures are anticipated to vary from 20°C (coldest quarter of the year) to 29.9°C (warmest quarter), and mean rainfall is predicted to range from 12 mm (driest quarter) to 512 mm (wettest quarter).

This fits perfectly with the current African savannah habitat (Hijmans et al., 2005). The equivalent statistics for the node subtending the pair *H. ergaster* + *H. erectus* (the first hominid to spread throughout Southern Eurasia) are 0.7°C-31.9°C for temperature range and from 4.8 mm to 1080 mm for precipitation range.

These estimations are realistic in light of *H. erectus* range extension into temperate regions as well as its colonization of warm and humid habitats (Indonesia) (Carotenuto et al., 2016; Joordens et al., 2015; Rizal et al., 2019). However, the predictions for yearly temperature extremes at the common ancestor to the three MHS range from negative 21.1°C to + 31.4°C, and for annual precipitation from 0.7 mm to 905 mm.

Although the common ancestor of MHS was probably an African species that never experienced these extreme climates (Profico et al., 2016), the values agree qualitatively with the notion that the arrival of this ancestor resulted in a sudden widening of climatic niche limits, whose offspring lived after the onset of fully glacial Pleistocene conditions (Churchill, 1998).

The massive increase in the estimated range of thermal conditions suitable for the MHS clade taxa (marked by a 20°C decrease in the minimum temperature of the coldest season of the year as compared to the hominin tree root, Figures 3 and S5) is independent of the phylogenetic hypothesis

we used and exceeds what is expected by a random process of increased phenotypic variance over time (namely the Brownian motion of evolution).

We identified a significant trend in the temperature of the coldest season achieved by hominins 97 times (Figure 3), however no trend was detected in the maximum temperatures of the hottest season, using 100 alternative tree topologies and branch lengths to account for phylogenetic uncertainty.

We discovered that the average temperature of the coldest quarter of the year in African species and predecessors was no less than 9.4°C, indicating that the winter chill was unlikely to have been an issue for them (Table S5).

In contrast, the coldest quarter of the year for *Homo heidelbergensis* was as cold as minus 12.3°C, implying that specific technological and cultural adaptations were required to avoid hypothermia and live in the highly seasonal, cold northern environments (Ulijaszek and Strickland, 1993; Ellison et al., 2005; Gilligan, 2007; Rivals et al., 2009; El Zaatari et al., 2016). Fitted garments (Amanzougaghene et al., 2019), thrown spears (Lenoir and Villa, 2006), adhesives (Carciumaru et al., 2012), and improved healthcare practices may have been among these modifications (Spikins et al., 2019).

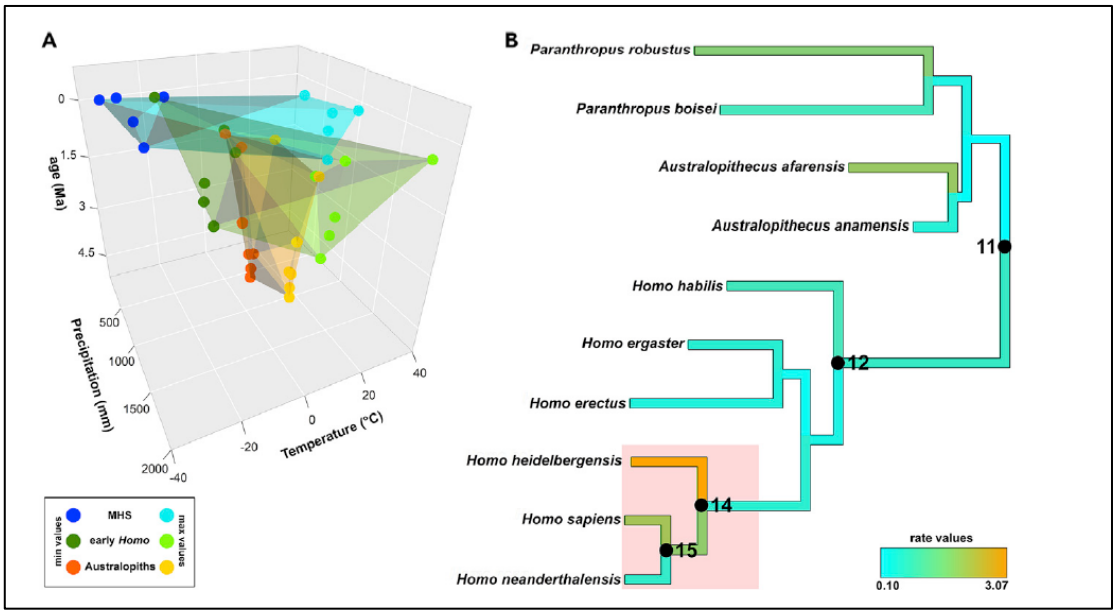

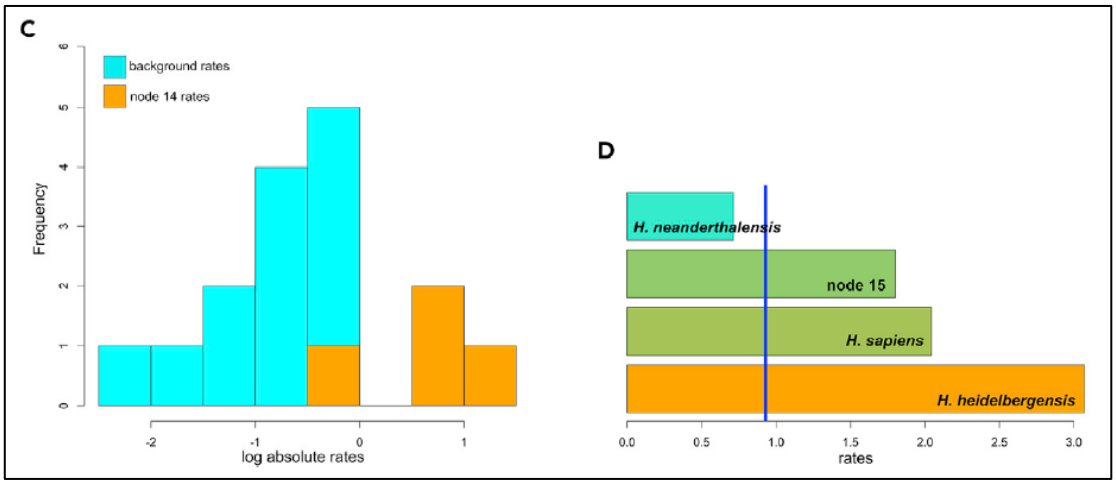

Figure 2. Climatic niche evolution in Hominins. A- 3D plot of the climatic niche space occupied by hominin clades through time.
B- Hominin tree used in this study. Branch colours are proportional to the multivariate rate of climatic niche evolution for each branch in the tree. Common ancestor to all species within *Homo* is indicated by note 12.
C- The distribution of the rates of niche evolution for the MHS clade compared to the rest of the branches in the tree (light blue).
D- Individual rates of niche evolution for the tree branches forming the MHS clade. MHS = modern *Homo* species, EHS = *Homo* species exclusive of MHS, Australopiths = species in the genus *Paranthropus* and *Australopithecus.*

According to some, the process of cultural niche construction (Laland et al., 2001; Laland and O'Brien, 2012), through which human cultural traits have changed the human adaptive niche and thus selective pressures and ecological inheritance (Odling-Smee and Laland, 2011), dates back to the emergence of the genus Homo 2.5 million years ago (Anton and Snodgrass, 2012; Anton et al., 2014). At the time, increasing reliance on stone artifact production and social learning (Hiscock, 2014) and collaboration (Fuentes et al., 2010; Fuentes, 2015) may have been especially influential in allowing hominins to not only escape their biological constraints but also actively change the environmental and ecological niches of other species (Low et al., 2019).

The occasional use of fire has equally deep origins in human history (Gowlett, 2016; Organ et al., 2011; Pruetz and Herzog, 2017). However, the frequent use of fire (Shimelmitz et al., 2014) and the capacity to manipulate hide, wood, and ivory (d'Errico and Henshilwood, 2007; Thieme, 1997) is recorded considerably later, during the Middle Stone Age (d'Errico, 2003), and is solely associated with the MHS. MHS is characterized by brain asymmetry and right handiness, which are often

associated with high cognitive abilities (Crow, 1993; Xiang et al., 2019; Melchionna et al., 2020a) (Frayer et al., 2012; Lozano et al., 2009; Poza-Rey et al., 2017). In contrast to MHS, EHS either did not migrate outside of Africa or travelled longitudinally over Eurasia.

Homo erectus moved over Africa and Eurasia to Java some 1.7 million years ago, but never settled north of the Mediterranean or southeast China (Carotenuto et al., 2016). From the appearance of *H. heidelbergensis* onward, northern, presumably colder habitats were no longer completely uninhabitable.

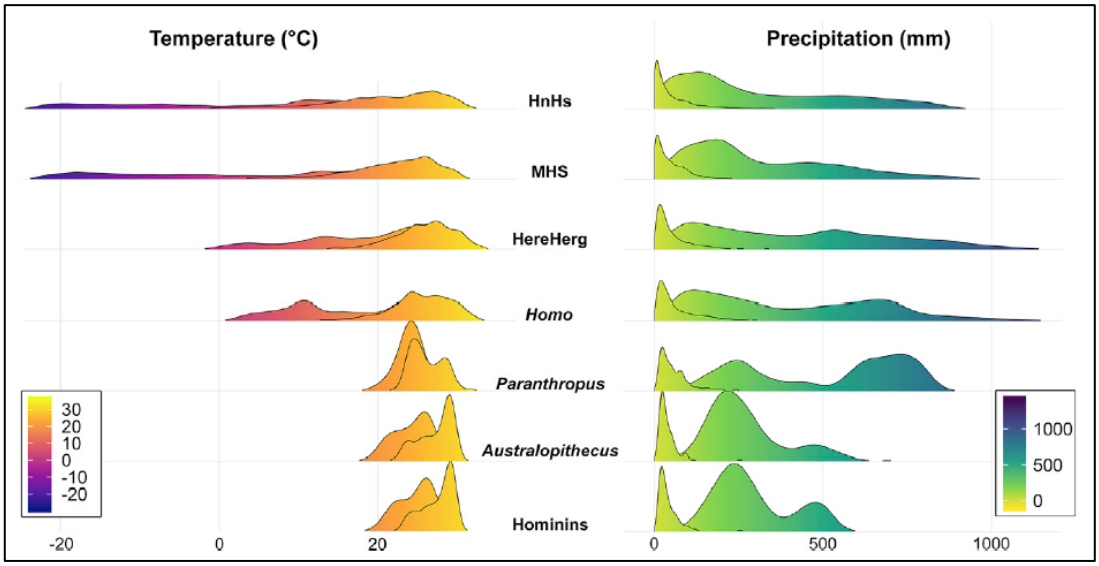

Figure 3. Estimated Temperature and Precipitation Ranges at Several Nodes in the Human Phylogenetic Tree The individual rows represent the density distribution of minimum and maximum temperature and precipitation, respectively, collapsed together. **HnHs** = common ancestor to *H. neanderthalensis* and *H. sapiens*, **MHS** = common ancestor to *H. heidelbergensis*, *H. neanderthalensis*, and *H. sapiens*; **HereHerg** = common ancestor to *H. erectus* and *H. ergaster*, **Homo** = common ancestor to *Homo species*, **Paranthropus** = common ancestor to all *Paranthropus* species, **Australopithecus** = common ancestor to all *Australopithecus* species, **Hominins** = common ancestor to hominins.

The rapid rise in the rates of evolution in climatic niche breadth (caused by a fast increase in cold tolerance, Figure 3) had a massive impact on geographic range. By modelling climatic niche limits as a random walk with constant variance process (e.g., the Brownian motion model of evolution, BM) and assuming as habitable all geographic cells with HQ >0.25, the rate shift accounts for a twofold increase in viable geographic range at MHS's ancestor (node 14 in the tree), for a net gain of $30x10^6$ km^2 (roughly the land surface of the African continent).

The habitable region becomes about three times bigger than predicted under BM at node 15, the progenitor of *Homo sapiens* and *Homo neanderthalensis*, equating to a geographic expansion of around $50x10^6$ km^2. This large increase in habitable territory is mostly due to migration towards northern latitudes, demonstrating the significance of the rate shift in Eurasia's colonization (Figure S5).

Although there is consistent evidence that *Homo* species may have exchanged genes with positive fitness consequences in cold environments through genetic introgression, this evidence is limited to the last 40 Ky and invariably pertains to local *Homo sapiens* populations, implying that it occurs much later than the rate shift and after the actual colonization of northern territories (Huerta-Sánchez et al., 2014; Sánchez-Quinto and Lalueza-Fox, 2015). Although the true consequences of any individual cultural or technological adaptation introduced by MHS will almost certainly be debated for some time, our findings suggest that these hominins were able to overcome the challenges imposed by life in northern habitats through a non-biological process, implying that behavioural modernity, defined as the ability to use technology and culture to overcome the constraints imposed by natural climate variability on the geographic distribution, is not limited to *Homo sapiens*.

Limitations of the study

The concept of niche construction in *Homo* implies cultural advancements (fitted clothing production, intentional use of fire, the production of tools made of perishable materials such as bone, hide, and wood), as well as improved social connections and skills that leave little to no archaeological evidence (Riede, 2019). Rather than focusing on such scant data, we chose to focus on one of the most significant implications of these cultural advances: the colonization of locations and temperatures outside of humans' physiological niche boundaries.

One drawback of our findings is that it is difficult to discern the precise relationship between the expansion of climatic niche boundaries and advances in material culture. Still, it is based on paleoclimate modelling, which has inherent uncertainty in the estimations.

Nonetheless, our analysis firmly indicates the significance of cultural niche construction in Homo evolution and how the abrupt acquisition of such niche construction abilities affected the geography of our own lineage in the distant past.

References

Symonds, M.R.E., Blomberg, S.P. (2014). A Primer on Phylogenetic Generalised Least Squares. In: Garamszegi, L. (eds) Modern Phylogenetic Comparative Methods and Their Application in Evolutionary Biology. Springer, Berlin, Heidelberg. https://doi.org/10.1007/978-3-662-43550-2_5

Adams, Dean C., F. James Rohlf, and Dennis E. Slice. "Geometric morphometrics: ten years of progress following the 'revolution.'" Italian Journal of Zoology 71.1 (2004): 5-16.

Dunbar, Robin IM. "The social brain hypothesis." Evolutionary Anthropology: Issues, News, and Reviews: Issues, News, and Reviews 6.5 (1998): 178-190.

Pandolfi, Luca, et al. "Evolving virtual and computational paleontology." Frontiers in Earth Science 8 (2020): 591813.

Rohlf, F. James. "Relative warp analysis and an example of its application to mosquito wings." Contributions to morphometrics 8 (1993): 131-159.

Mujal, Eudald, et al. "Upper Paleozoic to lower Mesozoic tetrapod ichnology revisited: photogrammetry and relative depth pattern inferences on functional prevalence of autopodia." Frontiers in Earth Science 8 (2020): 248.

Tate, Judith R., and Christopher E. Cann. "High-resolution computed tomography for the comparative study of fossil and extant bone." American Journal of Physical Anthropology 58.1 (1982): 67-73.

Weber, Gerhard W. "Virtual anthropology (VA): a call for glasnost in paleoanthropology." The Anatomical Record: An Official Publication of the American Association of Anatomists 265.4 (2001): 193-201.

Conroy, Glenn C., and Michael W. Vannier. "Noninvasive three-dimensional computer imaging of matrix-filled fossil skulls by high-resolution computed tomography." Science 226.4673 (1984): 456-458.

Wind, Jan. "Computerized X-ray tomography of fossil hominid skulls." American Journal of Physical Anthropology 63.3 (1984): 265-282.

Zonneveld FW, Wind J. 1985. High-resolution computed tomography of fossil hominid skulls: a new method and some results. In: Tobias PV Hominid evolution, past, present, and future. New York: Alan Liss. p 427–436.

Lui, J. H., Hansen, D. V., & Kriegstein, A. R. (2011). Development and evolution of the human neocortex. Cell, 146(1), 18-36.

Weber, Gerhard W., and Fred L. Bookstein. Virtual anthropology: a guide to a new interdisciplinary field. Vienna: Springer, 2011.

Aiello, L., Wood, B., Key, C., & Wood, C. (1998). Laser scanning and paleoanthropology. In Primate Locomotion (pp. 223-236). Springer, Boston, MA.

Kappelman, John. "Advances in three-dimensional data acquisition and analysis." *Primate locomotion*. Springer, Boston, MA, 1998. 205-222.

Zelditch, Miriam Leah, Donald L. Swiderski, and H. David Sheets. Geometric morphometrics for biologists: a primer. academic press, 2012.

Cardini, A. (2013). Geometric morphometrics. Biological Science Fundamental and Systematics. UK: Oxford.

Bookstein, F. L. (1989). Principal warps: Thin-plate splines and the decomposition of deformations. IEEE Transactions on pattern analysis and machine intelligence, 11(6), 567-585.

Harvey, Paul H., and Mark D. Pagel. *The comparative method in evolutionary biology*. Vol. 239. Oxford: Oxford university press, 1991.

Adams, D. C., Rohlf, F. J., & Slice, D. E. (2004). Geometric morphometrics: ten years of progress following the 'revolution.' Italian Journal of Zoology, 71(1), 5-16.

Johnston, M. R., Tabachnick, R. E., & Bookstein, F. L. (1991). Landmark-based morphometrics of spiral accretionary growth. Paleobiology, 17(1), 19-36.

Wärmländer, S. K., Garvin, H., Guyomarc'h, P., Petaros, A., & Sholts, S. B. (2019). Landmark typology in applied morphometrics studies: What's the point? The Anatomical Record, 302(7), 1144-1153.

Gunz, P., & Mitteroecker, P. (2013). Semilandmarks: a method for quantifying curves and surfaces. Hystrix, the Italian journal of mammalogy, 24(1), 103-109.

Iurino, D. A., Profico, A., Cherin, M., Veneziano, A., Costeur, L., & Sardella, R. (2015). A lynx natural brain endocast from Ingarano (southern Italy; late Pleistocene): Taphonomic, morphometric and phylogenetic approaches. Hystrix, 26(2), 110.

Ivanoff, D. V., Wolsan, M., & Marciszak, A. (2014). Brainy stuff of long-gone dogs: a reappraisal of the supposed Canis endocranial cast from the Pliocene of Poland. Naturwissenschaften, 101(8), 645-651.

Holloway, R. L. (2018). On the making of endocasts: the new and the old in paleoneurology. In Digital endocasts (pp. 1-8). Springer, Tokyo.

Friscia, A. R., Van Valkenburgh, B., & Goswami, A. (2010). Ecomorphology of North American Eocene carnivores: evidence for competition between carnivorans and creodonts. Carnivoran evolution: new views on phylogeny, form, and function, 311-341.

Wesley-Hunt, G. D., & Flynn, J. J. (2005). Phylogeny of the Carnivora: basal relationships among the carnivoramorphans, and assessment of the position of 'Miacoidea'relative to Carnivora. Journal of Systematic Palaeontology, 3(1), 1-28.

Rose, K.D. (2006) The Beginning of the Age of Mammals. Johns Hopkins University Press, Baltimore.

Spaulding, M., & Flynn, J. J. (2012). Phylogeny of the Carnivoramorpha: the impact of postcranial characters. Journal of Systematic Palaeontology, 10(4), 653-677.

Wang, X., Tedford, R. H., & Tedford, R. H. (2008). Dogs: their fossil relatives and evolutionary history. Columbia University Press.

Friscia, A. R., Van Valkenburgh, B., & Biknevicius, A. R. (2007). An ecomorphological analysis of extant small carnivorans. Journal of Zoology, 272(1), 82-100.

Agnarsson, I., Kuntner, M. and May-Collado, L.J. (2010) Dogs, cats, and kin: a molecular species-level phylogeny of Carnivora. Molecular Phylogenetics and Evolution, 54, 726–45.

Morlo, M., Gunnell, G. & Polly, P. D. (2009). What, if not nothing, is a creodont? Phylogeny and classification of Hyaenodontida and other former creodonts. Journal of Vertebrate Paleontology 29, 152A–152A.

Zack, S. P. (2011). New Species of the rare early Eocene creodont *Galecyon* and the radiation of early Hyaenodontidae. *Journal of Paleontology* **85**, 315–336.

Van Valkenburgh, B. (1999). Major patterns in the history of carnivorous mammals. Annual Review of Earth and Planetary Sciences, 27(1), 463-493.

Allin, E.F. (1975) Evolution of the mammalian middle ear. *Journal of Morphology*, **147**, 403–38.

Luo, Z.X. (2011) Developmental patterns in Mesozoic evolution of mammal ears. *Annual Review of Ecology, Evolution and Systematics*, **42**, 355–80.

Kemp, T.S. (2005) *The Origin and Evolution of Mammals*. Oxford University Press, Oxford.

Takechi, M., & Kuratani, S. (2010). History of studies on mammalian middle ear evolution: a comparative morphological and developmental biology perspective. Journal of Experimental Zoology Part B: Molecular and Developmental Evolution, 314(6), 417-433.

Richards, A. K. (1999). Phantoms in the Brain: VS Ramachandran and Sandra Blakeslee. New York: William Morrow, 320 pp, Journal of the American Psychoanalytic Association, 47(3), 960-960.

Chapman, S. C. (2011). Can you hear me now? Understanding vertebrate middle ear development. Frontiers in bioscience: a journal and virtual library, 16, 1675.

Wesley-Hunt, G. D. (2005). The morphological diversification of carnivores in North America. Paleobiology 31, 35–55.

McKenna, M. C. and Bell, S. K. (1997). Classification of Mammals Above the Species Level. New York, NY: Columbia University Press.

Morales, J., M. J. Salesa, M. Pickford, and D. Soria. 2001. A new tribe, new genus and two new species of Barbourofelinae (Felidae, Carnivora, Mammalia) from the Early Miocene of East Africa and Spain. Transactions of the Royal Society of Edinburgh: Earth Sciences, 92: 97–102.

Morlo, M., S. Peigné, and D. Nagel. 2004. A new species of Prosansanosmilus: implications for the systematic relationships of the family Barbourofelidae new rank (Carnivora, Mammalia). Zoological Journal of the Linnean Society, 140: 43–61.

Bryant, H. N. 1996b. Nimravidae. In D. R. Prothero and R. J. Emry (eds.), *The Terrestrial Eocene-Oligocene Transition in North America,* 453– 475. Cambridge University Press, Cambridge.

Peigné, S. 2003. Systematic review of European Nimravinae (Mammalia, **236** Bibliography Carnivora, Nimravidae) and the phylogenetic relationships of Palaeogene Nimravidae. *Zoologica Scripta,* 32: 199–229.

Adams, D. A. (1997). The Big Cats and Their Fossil Relatives: An Illustrated Guide to Their Evolution and Natural History. Science, 276(5314), 909-911.

Schlager, S., Jefferis, G., Ian, D., & Schlager, M. S. (2019). Package 'Morpho.'

Adams, D. C., Rohlf, F. J., & Slice, D. E. (2004). Geometric morphometrics: ten years of progress following the 'revolution.' Italian Journal of Zoology, 71(1), 5-16.

Bookstein, F. L. (1991, July). Thin-plate splines and the atlas problem for biomedical images. In Biennial international conference on information processing in medical imaging (pp. 326-342). Springer, Berlin, Heidelberg.

Adams JW, Olah A, McCurry MR, Potze S, Wilson BA. 2015. Surface model and tomographic archive of fossil primate and other mammal holotype and paratype specimens of the Ditsong National Museum of Natural History, Pretoria, South Africa. *PLoS One* 10: e0139800.

Alfaro ME, Bolnick DI, Wainwright PC. 2005. Evolutionary consequences of many-to-one mapping of jaw morphology to mechanics in labrid fishes. *The American Naturalist* 165: E140–E154.

Antón M, Salesa MJ, Pastor JF, Sánchez IM, Fraile S, Morales J. 2004. Implications of the mastoid anatomy of larger extant felids for the evolution and predatory behaviour of sabretoothed cats (Mammalia, Carnivora, Felidae). *Zoological Journal of the Linnean Society* 140: 207–221.

Barrett PZ. 2016. Taxonomic and systematic revisions to the North American Nimravidae (Mammalia, Carnivora). *PeerJ* 2016: e1658.

Castiglione S, Serio C, Mondanaro A, Melchionna M, Raia P. 2022. Fast production of large, time-calibrated informal supertrees with tree. merger. *Palaeontology* 65: e12588.

Castiglione S, Serio C, Tamagnini D, Melchionna M, Mondanaro A, Di Febbraro M, Profico A, Piras P, Barattolo F, Raia P. 2019. A new, fast method to search for morphological convergence with shape data. *PLoS One* 14: e0226949.

Castiglione S, Tesone G, Piccolo M, Melchionna M, Mondanaro A, Serio C, Di Febbraro M, Raia P. 2018. A new method for testing evolutionary rate variation and shifts in phenotypic evolution. *Methods in Ecology and Evolution* 9: 974–983.

Dickson BV, Pierce SE. 2019. Functional performance of turtle humerus shape across an ecological adaptive landscape. *Evolution* 73: 1265–1277.

Geng W-H, Wang X-P, Che L-F, Wang X, Liu R, Zhou T, Roos C, Irwin DM, Yu L. 2020. Convergent evolution of locomotory modes in Euarchontoglires. *Frontiers in Ecology and Evolution* 8: 476.

Gomes Rodrigues H, Lefebvre R, Fernández-Monescillo M, Mamani Quispe B, Billet G. 2017. Ontogenetic variations and structural adjustments in mammals evolving prolonged to continuous dental growth. *Royal Society Open Science* 4: 170494.

Harmon LJ, Kolbe JJ, Cheverud JM, Losos JB. 2005. Convergence and the multidimensional niche. *Evolution* 59: 409–421.

Losos JB. 2011. Convergence, adaptation, and constraint. *Evolution* 65: 1827–1840.

McHenry CR, Wroe S, Clausen PD, Moreno K, Cunningham E. 2007. Supermodeled sabercat, predatory behavior in *Smilodon fatalis* revealed by high-resolution 3D computer simulation. *Proceedings of the National Academy of Sciences of the United States of America* 104: 16010–16015.

Melchionna M, Profico A, Castiglione S, Serio C, Mondanaro A, Modafferi M, Tamagnini D, Maiorano L, Raia P, Witmer LM, Wroe S, Sansalone G. 2021. A method for mapping morphological convergence on three-dimensional digital models: the case of the mammalian sabretooth. *Palaeontology* 64: 573–584.

Organ C, Nunn CL, Machanda Z, Wrangham RW. 2011. Phylogenetic rate shifts in feeding time during the evolution of *Homo*. *Proceedings of the National Academy of Sciences of the United States of America* 108: 14555–14559.

Palmqvist P, Pérez-Claros JA, Janis CM, Gröcke DR. 2008. Tracing the ecophysiology of ungulates and predator-prey relationships in an Early Pleistocene large mammal community. *Palaeogeography, Palaeoclimatology, Palaeoecology* 266: 95–111.

Paterson RS, Rybczynski N, Kohno N, Maddin HC. 2020. A total evidence phylogenetic analysis of pinniped phylogeny and the possibility of parallel evolution within a monophyletic framework. *Frontiers in Ecology and Evolution* 7: 457.

Piras P, Maiorino L, Teresi L, Meloro C, Lucci F, Kotsakis T, Raia P. 2013. Bite of the cats: relationships between functional integration and mechanical performance as revealed by mandible geometry. *Systematic Biology* 62: 878–900.

Piras P, Silvestro D, Carotenuto F, Castiglione S, Kotsakis A, Maiorino L, Melchionna M, Mondanaro A, Sansalone G, Serio C, Vero VA, Raia P. 2018. Evolution of the sabertooth mandible: a deadly ecomorphological specialization. *Palaeogeography, Palaeoclimatology, Palaeoecology* 496: 166–174.

Raia P, Carotenuto F, Passaro F, Piras P, Fulgione D, Werdelin L, Saarinen J, Fortelius M. 2013. Rapid action in the Palaeogene, the relationship between phenotypic and taxonomic diversification in Cenozoic mammals. *Proceedings of the Royal Society B: Biological Sciences* 280: 20122244.

Renaud S, Ledevin R, Pisanu B, Chapuis JL, Quillfeldt P, Hardouin EA. 2018. Divergent in shape and convergent in function: adaptive evolution of the mandible in Sub-Antarctic mice. *Evolution* 72: 878–892.

Rohlf FJ, Bookstein FL. 2003. Computing the uniform component of shape variation. *Systematic Biology* 52: 66–69.

Salesa MJ, Antón M, Turner A, Morales J. 2005. Aspects of the functional morphology in the cranial and cervical skeleton of the sabretoothed cat *Paramachairodus ogygia* (Kaup, 1832) (Felidae, Machairodontinae) from the Late Miocene of Spain: implications for the origins of the machairodont killing bit. *Zoological Journal of the Linnean Society* 144: 363–377.

Sansalone G, Castiglione S, Raia P, Archer M, Dickson B, Hand S, Piras P, Profico A, Wroe S. 2020. Decoupling functional and morphological convergence, the study case of fossorial Mammalia. *Frontiers in Earth Science* 8: 1–10.

Schlager S. 2017. Morpho and Rvcg - shape analysis in R: R-Packages for geometric morphometrics, shape analysis and surface manipulations. In: Zheng G, Li S, and Székely G, eds. *Statistical shape and deformation analysis: methods, implementation, and applications.* Academic Press, 217–256.

Schlager S, Profico A, Vincenzo FD, Manzi G. 2018. Retrodeformation of fossil specimens based on 3D bilateral semi-landmarks: implementation in the R package 'Morpho'. *PLoS One* 13: e0194073.

Serio C, Raia P, Meloro C. 2020. Locomotory adaptations in 3D humerus geometry of Xenarthra: testing for convergence. *Frontiers in Ecology and Evolution* 8: 1–12.

Spassov N, Geraads D. 2015. A new felid from the Late Miocene of the Balkans and the contents of the genus *Metailurus* Zdansky, 1924 (Carnivora, Felidae). *Journal of Mammalian Evolution* 22: 45–56.

Stirton RA. 1960. A marine carnivore from the Clallam Miocene Formation, Washington: its correlation with nonmarine Faunas. *University of California Publications in Geological Sciences* 36: 345–368.

Strait DS, Constantino P, Lucas PW, Richmond BG, Spencer MA, Dechow PC, Ross CF, Grosse IR, Wright BW, Wood BA, Weber GW, Wang Q, Byron C, Slice DE, Chalk J, Smith AL, Smith LC, Wood S, Berthaume M, Benazzi S, Dzialo C, Tamvada K, Ledogar JA. 2013. Viewpoints: diet and dietary adaptations in early hominins: the hard food perspective. *American Journal of Physical Anthropology* 151: 339–355.

Tamagnini D, Meloro C, Raia P, Maiorano L. 2021. Testing the occurrence of convergence in the craniomandibular shape evolution of living carnivorans. *Evolution* 75: 1738–1752.

Tedford RH, Barnes LG, Ray CE. 1994. The Early Miocene littoral ursoid carnivoran *Kolponomos*: systematics and mode of life. *Proceedings - San Diego Society of Natural History* 29: 11–32.

Tseng ZJ, Grohé C, Flynn JJ. 2016. A unique feeding strategy of the extinct marine mammal *Kolponomos*: convergence on sabretooths and sea otters. *Proceedings of the Royal Society B: Biological Sciences* 283: 20160044.

Wainwright PC. 2007. Functional versus morphological diversity in macroevolution. *Annual Review of Ecology, Evolution, and Systematics* 38: 381–401.

Wang X, White SC, Guan J. 2020. A new genus and species of sabretooth, *Oriensmilus liupanensis* (Barbourofelinae, Nimravidae, Carnivora), from the Middle Miocene of China suggests barbourofelines are nimravids, not felids. *Journal of Systematic Palaeontology* 18: 783–803.

Wroe S, Chamoli U, Parr WCH, Clausen P, Ridgely R, Witmer L. 2013. Comparative biomechanical modeling of metatherian and placental saber-tooths: a different kind of bite for an extreme pouched predator. *PLoS One* 8: e668888.

Wroe S, Lowry MB, Anton M. 2008. How to build a mammalian super-predator. *Zoology* 111: 196–203.

Yohe LR, Solounias N. 2020. The five digits of the giraffe metatarsal. *Biological Journal of the Linnean Society* 131: 699–705.

Arnold, Lee J., et al. "Evaluating the suitability of extended-range luminescence dating techniques over early and Middle Pleistocene timescales: Published datasets and case studies from Atapuerca, Spain." Quaternary International 389 (2015): 167-190.

Bastir, Markus, and Antonio Rosas. "Hierarchical nature of morphological integration and modularity in the human posterior face." American Journal of Physical Anthropology 128.1 (2005): 26-34.

Bernardini, F., Mittleman, J., Rushmeier, H., Silva, C., & Taubin, G. (1999). The ball-pivoting algorithm for surface reconstruction. *IEEE transactions on visualization and computer graphics*, *5*(4), 349-359.

Butler, M. A., & King, A. A. (2004). Phylogenetic comparative analysis: a modeling approach for adaptive evolution. *The American Naturalist*, *164*(6), 683-695.

Castiglione, S., Tesone, G., Piccolo, M., Melchionna, M., Mondanaro, A., Serio, C., ... & Raia, P. (2018). A new method for testing evolutionary rate variation and shifts in phenotypic evolution. *Methods in Ecology and Evolution*, *9*(4), 974-983.

Castiglione, S., Serio, C., Mondanaro, A., Melchionna, M., Carotenuto, F., Di Febbraro, M., ... & Raia, P. (2020). Ancestral state estimation with phylogenetic ridge regression. *Evolutionary Biology*, *47*(3), 220-232.

Castiglione, S., Melchionna, M., Profico, A., Sansalone, G., Modafferi, M., Mondanaro, A., ... & Raia, P. (2022). *Human face-off: a new method for mapping evolutionary rates on three-dimensional digital models* (Vol. 65, No. 1, p. e12582).

Cerling, T. E., Mbua, E., Kirera, F. M., Manthi, F. K., Grine, F. E., Leakey, M. G., ... & Uno, K. T. (2011). Diet of Paranthropus boisei in the early Pleistocene of East Africa. *Proceedings of the National Academy of Sciences*, *108*(23), 9337-9341.

Christopoulos, D. T. (2012). Developing methods for identifying the inflection point of a convex/concave curve. *arXiv preprint arXiv:1206.5478*.

Christopoulos, D. T. (2016). On the efficient identification of an inflection point. *International Journal of Mathematics and Scientific Computing, (ISSN: 2231-5330)*, *6*(1).

CHRISTOPOULOS, D. T. 2019. inflection: Finds the Inflection Point of a Curve. R package v.1.3.5. https://cran.r-project.org/package=inflection

de la Torre, I., Benito-Calvo, A., Martín-Ramos, C., McHenry, L. J., Mora, R., Njau, J. K., ... & Stollhofen, H. (2021). New excavations in the MNK Skull site, and the last appearance of the Oldowan and Homo habilis at Olduvai Gorge, Tanzania. *Journal of Anthropological Archaeology*, *61*, 101255.

Delezene, L. K., Zolnierz, M. S., Teaford, M. F., Kimbel, W. H., Grine, F. E., & Ungar, P. S. (2013). Premolar microwear and tooth use in Australopithecus afarensis. *Journal of human evolution*, *65*(3), 282-293.

Diniz-Filho, J. A. F., Jardim, L., Mondanaro, A., & Raia, P. (2019). Multiple components of phylogenetic non-stationarity in the evolution of brain size in fossil hominins. *Evolutionary Biology*, *46*(1), 47-59.

Dominguez-Rodrigo, M., Pickering, T. R., Baquedano, E., Mabulla, A., Mark, D. F., Musiba, C., ... & Arriaza, M. C. (2013). First partial skeleton of a 1.34-million-year-old Paranthropus boisei from Bed II, Olduvai Gorge, Tanzania. *PLoS One*, *8*(12), e80347.

Du, S., Tao, Y., & Martinez, A. M. (2014). Compound facial expressions of emotion. *Proceedings of the national academy of sciences*, *111*(15), E1454-E1462.

Elliot, M. G., & Mooers, A. Ø. (2014). Inferring ancestral states without assuming neutrality or gradualism using a stable model of continuous character evolution. *BMC evolutionary biology*, *14*(1), 1-15.

Freidline, S. E., Gunz, P., Harvati, K., & Hublin, J. J. (2012). Middle Pleistocene human facial morphology in an evolutionary and developmental context. *Journal of Human Evolution*, *63*(5), 723-740.

Grine, F. E., Judex, S., Daegling, D. J., Ozcivici, E., Ungar, P. S., Teaford, M. F., ... & Walker, A. (2010). Craniofacial biomechanics and functional and dietary inferences in hominin paleontology. *Journal of Human Evolution*, *58*(4), 293-308.

Gould, S. J. and Lewontin, R. C. (1979). The spandrels of San Marco and the Panglossian paradigm: a critique of the adaptationist programme. Proceedings of the Royal Society B, 205 (1161), 581-598.

Gower, J. C. (1975). Generalized procrustes analysis. *Psychometrika*, *40*(1), 33-51.

Higham, T., Douka, K., Wood, R., Ramsey, C. B., Brock, F., Basell, L., ... & Jacobi, R. (2014). The timing and spatiotemporal patterning of Neanderthal disappearance. *Nature*, *512*(7514), 306-309.

Hublin, J. J., Ben-Ncer, A., Bailey, S. E., Freidline, S. E., Neubauer, S., Skinner, M. M., ... & Gunz, P. (2017). New fossils from Jebel Irhoud, Morocco, and the pan-African origin of Homo sapiens. *Nature*, *546*(7657), 289-292.

Lacruz, R. S., Stringer, C. B., Kimbel, W. H., Wood, B., Harvati, K., O'Higgins, P., ... & Arsuaga, J. L. (2019). The evolutionary history of the human face. *Nature ecology & evolution*, *3*(5), 726-736.

Ledogar, J. A., Smith, A. L., Benazzi, S., Weber, G. W., Spencer, M. A., Carlson, K. B., ... & Strait, D. S. (2016). Mechanical evidence that Australopithecus sediba was limited in its ability to eat hard foods. *Nature Communications*, *7*(1), 1-9.

Lu, Z., Meldrum, D. J., Huang, Y., He, J., & Sarmiento, E. E. (2011). The Jinniushan hominin pedal skeleton from the late Middle Pleistocene of China. *Homo*, *62*(6), 389-401.

Maddux, S. D., & Franciscus, R. G. (2009). Allometric scaling of infraorbital surface topography in Homo. *Journal of Human Evolution*, *56*(2), 161-174.

Marcé-Nogué, J., Püschel, T. A., Daasch, A., & Kaiser, T. M. (2020). Broad-scale morpho-functional traits of the mandible suggest no hard food adaptation in the hominin lineage. *Scientific reports*, *10*(1), 1-11.

Marcucio, R. S., Young, N. M., Hu, D., & Hallgrimsson, B. (2011). Mechanisms that underlie co-variation of the brain and face. *genesis*, *49*(4), 177-189.

Martinez-Maza, C., Rosas, A., & Nieto-Diaz, M. (2010). Brief communication: Identification of bone formation and resorption surfaces by reflected light microscopy. *American journal of physical anthropology*, *143*(2), 313-320.

Masao, F. T., Ichumbaki, E. B., Cherin, M., Barili, A., Boschian, G., Iurino, D. A., ... & Manzi, G. (2016). New footprints from Laetoli (Tanzania) provide evidence for marked body size variation in early hominins. *Elife*, *5*, e19568.

Neaux, D., Wroe, S., Ledogar, J. A., Heins Ledogar, S., & Sansalone, G. (2019). Morphological integration affects the evolution of midline cranial base, lateral basicranium, and face across primates. *American Journal of Physical Anthropology*, *170*(1), 37-47.

O'Meara, B. C. (2012). Evolutionary inferences from phylogenies: a review of methods. *Annual Review of Ecology, Evolution and Systematics*, *43*(267), 2012.

O'Meara, B. C., Ané, C., Sanderson, M. J., & Wainwright, P. C. (2006). Testing for different rates of continuous trait evolution using likelihood. *Evolution*, *60*(5), 922-933.

Parins-Fukuchi, C., Greiner, E., MacLatchy, L. M., & Fisher, D. C. (2019). Phylogeny, ancestors, and anagenesis in the hominin fossil record. *Paleobiology*, *45*(2), 378-393.

Pickering, R., Herries, A. I., Woodhead, J. D., Hellstrom, J. C., Green, H. E., Paul, B., ... & Hancox, P. J. (2019). U–Pb-dated flowstones restrict South African early hominin record to dry climate phases. *Nature*, *565*(7738), 226-229.

Price-Waldman, R. M., Shultz, A. J., & Burns, K. J. (2020). Speciation rates are correlated with changes in plumage color complexity in the largest family of songbirds. *Evolution*, *74*(6), 1155-1169.

Profico, A., Piras, P., Buzi, C., Di Vincenzo, F., Lattarini, F., Melchionna, M., ... & Manzi, G. (2017). The evolution of cranial base and face in Cercopithecoidea and Hominoidea: Modularity and morphological integration. *American Journal of Primatology*, *79*(12), e22721.

Antonio, P., Costantino, B., Silvia, C., Marina, M., Paolo, P., Alessio, V., & Pasquale, R. (2021). Arothron: An R package for geometric morphometric methods and virtual anthropology applications. *American Journal of Physical Anthropology*, *176*(1), 144-151.

Püschel, H. P., Bertrand, O. C., O'reilly, J. E., Bobe, R., & Püschel, T. A. (2021). Divergence-time estimates for hominins provide insight into encephalization and body mass trends in human evolution. *Nature ecology & evolution*, *5*(6), 808-819.

Revell, L. J., & Harmon, L. J. (2008). Testing quantitative genetic hypotheses about the evolutionary rate matrix for continuous characters. *Evolutionary Ecology Research*, *10*(3), 311-331.

Rizal, Y., Westaway, K. E., Zaim, Y., van den Bergh, G. D., Bettis, E. A., Morwood, M. J., ... & Ciochon, R. L. (2020). Last appearance of Homo erectus at Ngandong, Java, 117,000–108,000 years ago. *Nature*, *577*(7790), 381-385.

Schlager, S. (2017). Morpho and Rvcg–shape analysis in R: R-packages for geometric morphometrics, shape analysis and surface manipulations. In *Statistical shape and deformation analysis* (pp. 217-256). Academic Press.

Schlager, S., Profico, A., Di Vincenzo, F., & Manzi, G. (2018). Retrodeformation of fossil specimens based on 3D bilateral semi-landmarks: Implementation in the R package "Morpho". *PloS one*, *13*(3), e0194073.

Schlager, S., Jefferis, G. and Dryden, I. 2020. Morpho: Calculations and Visualisations Related to Geometric Morphometrics. R-package v.2.8. https://cran.r-project.org/web/packages/Morpho/index.html

Schuh, A., Kupczik, K., Gunz, P., Hublin, J. J., & Freidline, S. E. (2019). Ontogeny of the human maxilla: A study of intra-population variability combining surface bone histology and geometric morphometrics. *Journal of Anatomy*, *235*(2), 233-245.

Smaers, J. B., Mongle, C. S., & Kandler, A. (2016). A multiple variance Brownian motion framework for estimating variable rates and inferring ancestral states. *Biological Journal of the Linnean Society*, *118*(1), 78-94.

Stelzer, S., Neubauer, S., Hublin, J. J., Spoor, F., & Gunz, P. (2019). Morphological trends in arcade shape and size in Middle Pleistocene Homo. *American Journal of Physical Anthropology*, *168*(1), 70-91.

Strait, D. S., Weber, G. W., Neubauer, S., Chalk, J., Richmond, B. G., Lucas, P. W., ... & Smith, A. L. (2009). The feeding biomechanics and dietary ecology of Australopithecus africanus. *Proceedings of the National Academy of Sciences*, *106*(7), 2124-2129.

Stringer, C. (2016). The origin and evolution of Homo sapiens. *Philosophical Transactions of the Royal Society B: Biological Sciences*, *371*(1698), 20150237.

Teaford, M. F., & Ungar, P. S. (2000). Diet and the evolution of the earliest human ancestors. *Proceedings of the National Academy of Sciences*, *97*(25), 13506-13511.

Ungar, P. S., Krueger, K. L., Blumenschine, R. J., Njau, J., & Scott, R. S. (2012). Dental microwear texture analysis of hominins recovered by the Olduvai Landscape Paleoanthropology Project, 1995–2007. *Journal of Human Evolution*, *63*(2), 429-437.

Villmoare, B. (2018). Early Homo and the role of the genus in paleoanthropology. *American Journal of Physical Anthropology*, *165*, 72-89.

White, T. D., Black, M. T., & Folkens, P. A. (2011). *Human osteology*. Academic press.

Adams, D. C., & Collyer, M. L. (2009). A general framework for the analysis of phenotypic trajectories in evolutionary studies. *Evolution: International Journal of Organic Evolution*, 63(5), 1143-1154.

AKERSTEN, W. A. 1985. Canine function in *Smilodon* (Mammalia; Felidae; Machairodontinae). *Natural History Museum of Los Angeles County*, Contributions in Science, 356, 1–22.

Alfaro, M. E., Bolnick, D. I., & Wainwright, P. C. (2005). Evolutionary consequences of many-to-one mapping of jaw morphology to mechanics in labrid fishes. *The American Naturalist*, *165*(6), E140-E154.

Arbuckle, K., Bennett, C. M., & Speed, M. P. (2014). A simple measure of the strength of convergent evolution. *Methods in Ecology and Evolution*, *5*(7), 685-693.

Bernardini, F., Mittleman, J., Rushmeier, H., Silva, C., & Taubin, G. (1999). The ball-pivoting algorithm for surface reconstruction. *IEEE transactions on visualization and computer graphics*, *5*(4), 349-359.

Biknevicius, A. R., Van Valkenburgh, B., & Walker, J. (1996). Incisor size and shape: implications for feeding behaviors in saber-toothed "cats." *Journal of Vertebrate Paleontology*, *16*(3), 510-521.

Castiglione, S., Tesone, G., Piccolo, M., Melchionna, M., Mondanaro, A., Serio, C., ... & Raia, P. (2018). A new method for testing evolutionary rate variation and shifts in phenotypic evolution. *Methods in Ecology and Evolution*, *9*(4), 974-983.

Castiglione, S., Serio, C., Tamagnini, D., Melchionna, M., Mondanaro, A., Di Febbraro, M., ... & Raia, P. (2019). A new, fast method to search for morphological convergence with shape data. *PloS one*, *14*(12), e0226949.

Christiansen, P. (2008). Evolutionary convergence of primitive sabertooth craniomandibular morphology: the clouded leopard (Neofelis nebulosa) and Paramachairodus ogygia compared. *Journal of Mammalian Evolution*, *15*(3), 155-179.

Christopoulos, D. T. (2012). Developing methods for identifying the inflection point of a convex/concave curve. *arXiv preprint arXiv:1206.5478*.

Cunningham, J. A., Rahman, I. A., Lautenschlager, S., Rayfield, E. J., & Donoghue, P. C. (2014). A virtual world of paleontology. *Trends in ecology & evolution*, *29*(6), 347-357.

Duckler, G. L. (1997). Parietal depressions in skulls of the extinct saber-toothed felid Smilodon fatalis: evidence of mechanical strain. *Journal of Vertebrate Paleontology*, *17*(3), 600-609.

Emerson, S. B., & Radinsky, L. (1980). Functional analysis of sabertooth cranial morphology. *Paleobiology*, *6*(3), 295-312.

Figueirido, B., Lautenschlager, S., Pérez-Ramos, A., & Van Valkenburgh, B. (2018). Distinct predatory behaviors in scimitar-and dirk-toothed sabertooth cats. *Current Biology*, *28*(20), 3260-3266.

Gunz, P., Mitteroecker, P., Neubauer, S., Weber, G. W., & Bookstein, F. L. (2009). Principles for the virtual reconstruction of hominin crania. *Journal of human evolution*, *57*(1), 48-62.

Harmon, L. J., Kolbe, J. J., Cheverud, J. M., & Losos, J. B. (2005). Convergence and the multidimensional niche. *Evolution*, *59*(2), 409-421.

Ingram, T., & Mahler, D. L. (2013). SURFACE: detecting convergent evolution from comparative data by fitting Ornstein-Uhlenbeck models with stepwise Akaike Information Criterion. *Methods in Ecology and Evolution*, *4*(5), 416-425.

Janis, C. (2008). An evolutionary history of browsing and grazing ungulates. In *The ecology of browsing and grazing* (pp. 21-45). Springer, Berlin, Heidelberg.

Figueirido, B., DeSantis, L., & Lautenschlager, S. (2020). An eye for a tooth: Thylacosmilus was not a marsupial" saber-tooth predator". *Peerj*, *8*, e9346-e9346.